Methods for Ultra-Wideband Radar Imaging of Low Contrast, Low Radar Cross Section Targets

by

Robert S. C. Winter

A thesis submitted in partial fulfillment of the requirements for the degree of

Doctor of Philosophy

in

Electromagnetics & Microwaves

Department of Electrical and Computer Engineering

University of Alberta

© Robert S. C. Winter, 2023

Abstract

Ultra-wideband (UWB) radar systems have been used as sensing and imaging tools for many industrial needs, and many more applications of the technology are currently under investigation. This research attempts to solve some of the issues UWB time domain synthetic aperture radar (SAR) faces in imaging applications regarding low contrast target imaging.

First, this work investigates the near-field UWB antennas for time-domain radiation and pulse shaping in the near-field. It proposes a new technique and calibration methods to quantify the near-field effects, such as superluminal propagation of the signal on imaging. Then it uses this information to improve the image quality in SAR processing. The near-field imaging technique is validated experimentally.

Second, a new miniaturized antenna is proposed for pulse radiation. This antenna is used to investigate the performance of time-domain and frequency-domain imaging techniques. Different metrics, such as phase center control for time-domain antenna design, are presented. The radiated pulse shape and pulse-peak velocity in different directions are characterized.

Third, a method is presented which can augment the data from arbitrary aperture locations to improve the image quality in case of an obscure target location. This method is validated and demonstrates the ability to enhance the quality of images and readability of target features under challenging measuring scenarios.

Fourth, a new processing technique is presented to consider the variable group velocity of the signal, in the case of a multi-layered medium, to the Global Back-Projection (GBP) algorithm. This technique is shown to produce higher-quality images. This technique is validated using experimental data. Succeeding this point, a time domain alternative to har-

monic radar is presented. The technique is shown theoretically and using basic experiments. This technique shows promise to be used to find and track non-linear objects.

Preface

Chapter 2 is published as: R. S. C. Winter, D. Oloumi and K. Rambabu, "UWB Sensor Characterization for Radar Sensing and Imaging in Superluminal Propagation Regions," in IEEE Transactions on Microwave Theory and Techniques, vol. 69, no. 1, pp. 297-307, Jan. 2021.

Chapter 4 is published as: R. S. C. Winter, D. Oloumi, K. Rambabu, "Virtually Developed Synthetic Aperture Radar: Theory, Simulation and Measurements," in IEEE Trans. on Geoscience and Remote Sensing, vol. 57, no. 5, pp. 2855-2863, May 2019.

Chapter 5 is published as: D. Oloumi, R. S. C. Winter, A. Kordzadeh, P. Boulanger and K. Rambabu, "Microwave Imaging of Breast Tumor Using Time-Domain UWB Circular-SAR Technique," in IEEE Transactions on Medical Imaging, vol. 39, no. 4, pp. 934-943, April 2020. It appears in Section IV, V, VI, Appendix A,B

To my parents

To be sensual, I think, is to respect and rejoice in the force of life, of life itself, and to be present in all that one does, from the effort of loving to the making of bread.

– James Baldwin, The Fire Next Time.

Acknowledgements

First and foremost I would like to thank my Supervisor, Dr. Rambabu Karumudi, who has been a model and an inspiration for my career, and without whom I would never have pursued graduate studies. For their guidance to this thesis I would like to thank the members of my committee Drs. Robert Fedosejevs, Xingqi Zhang, Pierre Boulanger, Mrinal Mandal, and Amina Hussein. I would also like to thank the contribution of the external examiner Dr. Prasad Gogineni.

During my degree I worked with two post postdoctoral researchers, Drs. Daniel Oloumi and Rouhollah Feghhi. Their contributions and the direction provided by both of them are much appreciated. I would also like to hightlight the contributions of students I either worked on various projects with or helped me navigate different aspects of being a grad student, namely: Michael Breitkreutz, Kapil Gangwar, Erik Hedlin, Adil Karimov, Simon Koots, Fatemeh Modares, Sam Pollock, and Braden Smyth.

I would like to thank the Natural Sciences and Engineering Research Council of Canada for much of the funding that helped me pursue this degree.

My family, have been an example and inspiration since childhood. I would especially like to thank my parents George and Pam, whose sacrifices and support are the foundation for everything that I am.

Contents

List of Tables

List of Figures

List of Acronyms

UWB	ultra-wideband
RCS	radar cross section
BW	band width
$FWHM$	full width half max
GBP	global back projection
SAR	synthetic aperture radar
AVA	antipodal Vivaldi antenna
$BAVA$	balanced antipodal Vivaldi antenna
FCC	federal communications commission
$CSAR$	circular synthetic aperture radar
$LSAR$	linear synthetic aperture radar
MRI	magnetic resonance imaging
CT	computed tomography

Chapter 1

Introduction

1.1 Motivation

Ultra-wideband (UWB) pulses have a large bandwidth with respect to the central frequency. This wide bandwidth gives UWB radar systems high spatial resolutions. The resolutions are on the order of centimetres down to millimetres. Generally UWB radar achieve this large bandwidth by using short duration pulses. UWB radar is used in many applications requiring high spatial resolution. The pulses are typically on the order of 100 ps and correspond to frequencies in the range of 1-10 GHz. The frequency band and pulse width allows for good resolution, in the range of 1 cm, as well as being able to penetrate into solid objects. Due to this, UWB has some advantages over other modalities in the field of sensing and imaging. Firstly, UWB hardware is relatively cheap to implement compared to MRI or CT. The hardware can be made small and lightweight as well. Compared to the most similar modalities, namely ultrasound and infrared, UWB has lower resolution. However, UWB is easier to implement when sensing into physical objects is required, as ultrasound presents some difficulty in matching the transponder to the target scene and infrared inherently has very limited penetration.

For these reasons, a range of applications are well suited to UWB solutions. These include applications in the region of civil engineering such as ice-road monitoring [1], pavement monitoring [2] and others. UWB has also been applied to the field of biomedical imaging and monitoring such as internal imaging [3], breast imaging and cancer detection [4]–[6],

stroke imaging [7], as well as vital sign monitoring [8], [9].

The applications also extend to military applications [10], oil extraction monitoring [11], air-plane navigation [12], weather monitoring [13] as well as many others.

In this thesis we will attempt to solve some issues with UWB imaging and sensing. We aim to produce techniques that will improve the quality of UWB results and hopefully expand the potential applications for UWB technology.

1.2 Synthetic Aperture Radar

Radar pulses are transmitted and received by antennas. Antennas have a beamwidth, which determines how tightly concentrated the radiation will be. Due to the beamwidth, a signal transmitted and received will have some ambiguity associated with it in the azimuth as well as in the elevation. Received signals will also have ambiguity in the radial direction based on the pulse width of the transmitted pulse.

In order to create higher resolution images, the beamwidth and the signal pulse width can be decreased. This can create higher resolution images; however, this will lead to higher cost and complexity of the radar system. Additionally, there are physical limits relating the antenna size and gain. This implies that increasing antenna gain will require an increasingly large antenna. SAR is a technique which can increase the resolution without increasing the antenna size or decreasing the pulse width. It does this by synthesizing an effectively larger antenna by signal processing instead of actually using a larger antenna. Antennas used in certain SAR applications can be small and have relatively large beamwidths.

The basis for the synthesis can be understood by thinking about a large array of radiating elements. The elements of the array receive the transmitted signal at the same time and transmit the signal simultaneously. In the receive mode, the elements receive at the same time and the signals are combined in the receiver. In SAR an analogous situation occurs, except the elements of the array transmit and receive at different times. The combination of the effects of the different elements occurs in the signal processing, instead of physically. In addition to using of a smaller radiating element, another benefit of the SAR technique is

the added flexibility created by the processing of the data in software.

SAR can be especially useful in UWB techniques as it is difficult to build an antenna which has high gain over a large bandwidth. The most commonly used apertures in an UWB setting are linear synthetic aperture radar (LSAR) and circular synthetic aperture radar (CSAR). However, there is no restriction on the shape of the aperture and the transceiver can be placed at arbitrary locations. That being said, certain apertures will generate higher quality results as a function of number of aperture locations.

1.3 Simulation Method

As a first step to investigate different aspects of microwave imaging such as, the impact of the aperture, the effect of the antenna, the path length loss, or the reflection from a target scene, the first thing to do is to simulate the situation. Simulations are a key aspect of design for microwave systems. Thanks to computational progress, most simulations can be done using a "full wave environment". This means the simulations are based directly on Maxwell's equations with few simplifying assumptions. There are many different styles of simulations such as finite differential time domain (FDTD), finite element method (FEM), method of moments (MOM) and many others. Most of the work in this thesis focuses on UWB imaging in the time domain. Thus the FDTD is most relevant to this work. The FDTD is a time domain simulation and thus directly solves the problem in the time domain and details in the frequency domain can be found by appropriate Fourier transforms of the results. The FDTD involves discretizing the differential form of Maxwell's equations and time stepping forward, first solving for the electric fields based on the magnetic fields and then using those electric fields to solve for the magnetic fields at the next time step. This process is subject to the boundary conditions of the situation and the simulations continues until a criteria is met.

The FDTD is based on a discretizing the space into a 3D lattice. The spacing of the lattice structure depends both on the desired detail of any objects in the target scene as well as the highest frequency present in the simulation. For the approximations present in the

simulation to hold, there should be at least 10 cells per wavelength. The simulation in time is also discretized. The time step should be short enough such that it takes at least two time steps for a wave front to cross two adjacent points in the lattice. Thus the time step is limited by the material of lowest permittivity in the simulation (which indicates the highest group velocity in the simulation) as well as the smallest grid spacing in the simulation. As the simulation time is a function of both the number of time steps and the number of grid points and is of order $O(tN)$, where t is the number of time steps and N is the total number of grid points.

1.4 Experimental Procedures

Although highly accurate in many situations, simulations do not provide some of the complications present in real world and can be inaccurate. To validate processing techniques and to investigate other electromagnetic phenomena a experimental setup is required.

When conducting radar imaging a setup such as that described in Fig. 1.4 is used. The system consists of a pulse generator, a pulse shaping network, a transmitting antenna, receiving antenna, followed by a oscilloscope to collect the return data. An example of this setup is shown in Fig. 1.4. Off the shelf systems can also be used in the transmitter. For experiments conducted in Chapters 4,5 the pulse generator used was a AVTECH AVP -3SA-C, which generates pulses with 50ps rise time, with a variable amplitude up to $10V$ at a $1MHz$ pulse repetition frequency (PRF). The transmitted pulse has an power level of 2W. The outputted pulse has a centre frequency of 6.5GHz and a -10dB bandwidth of 10GHz. The experiments conducted in Chapters 2,6, and 3 were generated by a system developed at the U of A by Rouhollah Feghhi [14]. This system outputted pulses with a PRF of 10 MHz, a pulse amplitude of 5.0 V, a power level of 500 mW, and a tunable pulse width of 56 to 300 ps. This system was developed in a mono-static as well as bi-static configurations.

The signal is digitized by an Agilent DCA 86100B sampling oscilloscope in the case of the off the shelf pulse generator and a Keysight Infiniti Vision DSOX3024A Digital storage Oscilloscope in the case of the built system.

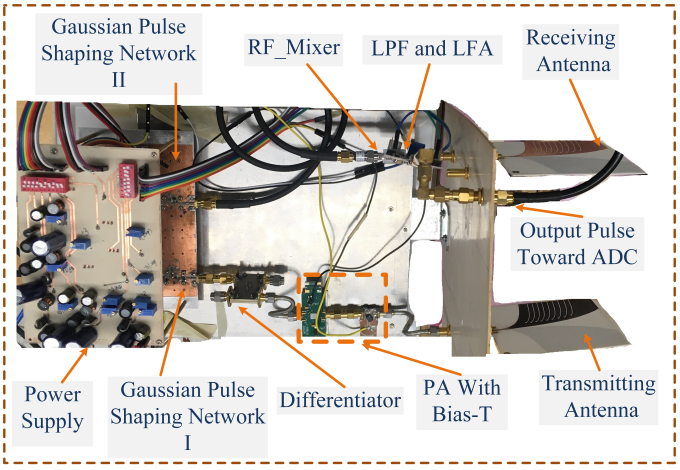

Figure 1.1: (a) UWB radar system overview. Image courtesy of Rouhollah Feghhi [14].

Different antennas are used depending on the different applications. Different antennas have different bandwidths and are thus, optimized for different pulse widths. Throughout the thesis several wideband antennas are used. The large Vivaldi antenna has a size of 18x20cm and a low frequency cut-off of 950 MHz to a upper frequency of 11 GHz [15]. This antenna is merely an expanded version of what is refereed to in the text as the mid sized Vivaldi this has a low frequency cut-off of 2.2 GHz and a upper frequency of over 11 GHz. A miniaturized Vivaldi antenna [16] is also used in several experiments it has a low frequency cut-off of 3.1 GHz and a upper frequency cut-off of over 11 GHz. This antenna was optimized for radiation into an oil medium, which is used as a matching liquid in certain imaging applications. In addition to those antennas a novel miniaturized antenna is developed and presented in Chapter 3, this antenna has a low frequency cut-off of 1.3 GHz and has some interesting characteristics such as high gain and minimized near-field.

1.5 Data Processing

For most of the experiments as well as the simulations conducted, the procedure for processing the data follows a similar procedure. The data of the target scene are collected, either along the aperture or in other situations. The radar system is then arranged so it radiates into free space and the received pulse is called the ambient pulse. The ambient pulse

is the signal when there are no targets present. The ambient pulse, incorporates the details of the mutual coupling, the cables and other details of the radar system itself. In certain situations some of the target scene can be incorporated into the ambient signal and serves to remove those items from the reconstructed image. The ambient signal is removed from the received signals of interest by direct subtraction. Additionally, a signal from a scatterer at a known location, such as a metal plate or rod may be used to obtain a time reference.

Once the data are collected, the first step taken is normally a low pass filter to remove as much unwanted noise as possible. Next interpolation is performed. The interpolation is optional and can increase image quality in certain applications. Once interpolation is performed, the next step consists of aligning the pulses. This is to compensate with the drift of the radar system. The drift is caused by small inaccuracies in triggering the measurement at the same time. The alignment is done by taking a early portion of the pulse, usually before any contribution of the target scene is present, and is normally related to the mutual coupling. After this alignment is completed, the ambient pulse can be subtracted. The resulting datum is called the calibrated pulse. The calibrated pulse can undergo time gating to remove data which originates from outside the target scene or from multi-layer reflections. This final data can be then used in a reconstruction algorithm like the GBP algorithm to create a reconstructed image.

1.6 UWB System Summary

The system design begins with the desired pulse width of the transmitted system. Based on this, an appropriate pulse shaping architecture can be chosen. Different architectures are better suited to different frequencies and power levels. Different architectures are based around different discrete elements. Step recovery diodes (SRD), tunnelling diodes (TD), step recovery diodes (SRDs), high frequency transistors, bipolar junction transistors, non-linear transmission lines (NLTLs), and Avalanche transistors are some of the discrete elements that have been used to create the short duration pulses required. Integrated circuit (IC) designs can also be used instead of discrete elements to generate the short pulse widths desired.

The pulse ringing level, which is the ratio of the ringing after the pulse to the size of the pulse, along with the power level and the pulse width are all factors determining which architecture is best for the application in question.

Depending on the system used, the output of the pulse shaping network will be some form of Gaussian waveform. As this carries significant energy at DC, which cannot be accepted at the transmitting antenna, the waveform is usually altered prior to arriving at the antenna. This usually takes the form of a differentiation caused by a delay line or a 90^o coupler. The bandwidth of the 90^o coupler can be chosen to fit with the bandwidth of the Gaussian pulse. Delay lines offer more flexibility than couplers and have an ability to alter the pulse shape in addition to performing differentiation. This can be used to improve symmetry of the signal outputted to the antenna, or to customize the signal transmitted by the antenna.

The signal outputted by the differentiator block often takes the form of a first derivative Gaussian pulse. This waveform is incident on the transmitting antenna. The quality of the antenna takes into account both frequency and time domain concepts. In the frequency domain, the bandwidth of the antenna should match with the frequency of the input signal. The directivity of the antenna is also an important consideration. Due to the short nature of the pulse, certain frequency domain concepts are not application to the design, thus consideration of the time domain should be incorporated. This consists of ensuring that the output of the waveform has limited ringing and has the desired shape. It is known that the transfer function of an aperture antenna in the receiving mode is equal to the integral of its transfer function in the transmitting mode [17]. However, the aperture antenna differentiates the pulse during radiation [18], [19]. For traveling wave antennas, the receive response is only a function of the effective length of the antenna [20]. Thus in the case of a first derivative Gaussian pulse being incident on the antenna, ideally, the transmitted waveform will take the form a second derivative Gaussian pulse.

The transmitted signal is incident on the target scene and is scattered by the objects in the target scene. The signal is then received by the radar system. This can be done through either a bi-static or mono-static configuration. The two different configurations

have different strengths and weaknesses. For the bi-static configuration a major downside is the mutual coupling between the two antennas. This can mean that the receiving side can become saturated. This means that detecting objects very close to the antennas is difficult. In order to reduce mutual coupling, the two antennas can be moved farther apart from one another. As the antennas are moved apart to reduce mutual coupling, the overlap of the beam patterns of the two antennas decreases. This also leads to added complexity in the processing. By contrast a mono-static or single antenna configuration can be employed. This can be implemented by using a T/R switch or a circulator. This element should cover the bandwidth of the system which is difficult. The mono-static configuration has added system complexity, and can suffer from reflections based on the mismatch of the antenna and can have reduced power levels when compared to bi-static architectures.

1.6.1 Imaging

For radar applications where an image of the target scene is desired there are several methods to reconstruct the final image. The main aspect of the reconstruction problem is related to the low gain antenna used in SAR applications. Instead of using a large physical antenna with high gain for the measurements, a smaller, low gain antenna is used instead. In SAR imaging, the focusing is achieved in the processing stage instead. The SAR process is explained in Fig. 1.2. Fig. 1.2(a) shows the probability of the location in the target scene based on an idealized case with one target. Fig. 1.2(b) shows the same probability function after several transceiver locations are added together. The ambiguity from the low gain nature of the antenna and the pulse width are partially resolved by the SAR data.

One method to convert SAR data into an image is the Global Back-Projection algorithm (GPB). The algorithm directly performs a summation of the data of the aperture positions at each pixel in the reconstructed image. The algorithm can be summarized in the following manner: for each data collected at aperture location having transmitter location (X_t, Y_t, Z_t) and receiver location (X_r, Y_r, Z_r) and for each pixel with location (X_p, Y_p, Z_p), the round trip distance is first found:

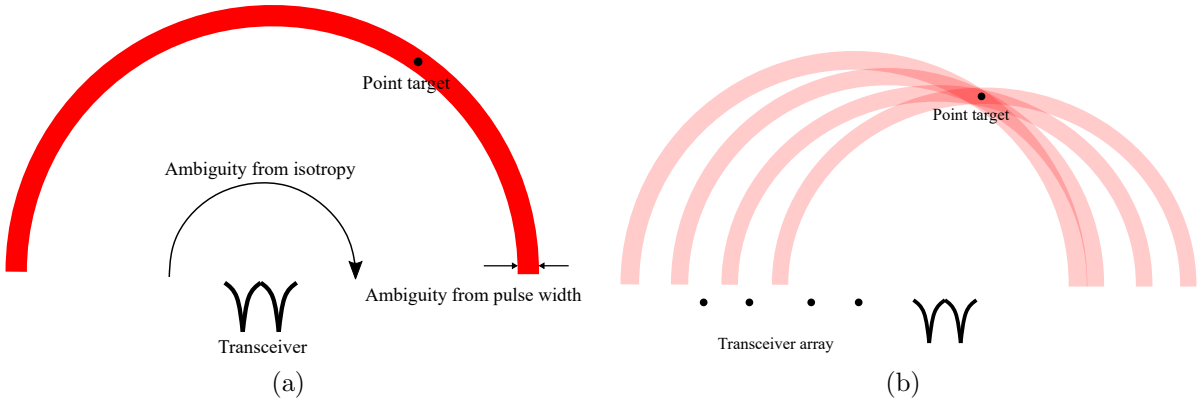

Figure 1.2: (a) Image showing the target localization from the first aperture location. (b) Image showing target localization as more aperture locations are added.

$$R = \sqrt{(X_t - X_p)^2 + (Y_t - Y_p)^2 + (Z_t - Z_p)^2} + \sqrt{(X_r - X_p)^2 + (Y_r - Y_p)^2 + (Z_r - Z_p)^2} \tag{1.1}$$

The round trip time can be found if the speed is known and can be found by the expression:

$$T = R/v \tag{1.2}$$

where v is the speed of the pulse along the round trip. The pixel data is then augmented by adding the received signal from that aperture location at the index corresponding to that round trip time. The index can be found by the following equation:

$$index = round(T/\Delta T) \tag{1.3}$$

where ΔT is the time step of the received data. This process is repeated for each pixel in the image and the entire process is repeated for each aperture location.

Several issues with this simple procedure can occur. Firstly, this process assumes knowledge of the speed of the signal in the target scene. This can be difficult for several reasons. Firstly, target scenes are not always uniform and may have different regions that contain materials with different group velocities. Additionally, the group velocity of the different

materials may not be known a priori. Finally, when imaging in the near-field of the antenna, the near-field of the antenna will have an effect on the apparent group velocities in the region.

Another issue is the choice of aperture. The aperture is restricted by the target scene and the measurement setup. More aperture points require additional time to collect, which is another restriction if time is a concern. Different apertures will lead to different distortions in the final reconstructed image. For example in a linear synthetic aperture radar (LSAR) measurement in the near-field, distortion will occur in the axis travelling away from the aperture, as the fields travel from the near to far field. LSAR measurements will contain distortion at the edges of the aperture. The aperture will need to be extended past the edge of the target scene in order to remove the edge distortion from the reconstructed image.

1.7 The Contributions of this Thesis

1.7.1 Overall Contributions

This thesis is motivated to try and improve the ability of UWB imaging to detect objects that have either low RCS or low contrast. The current techniques, approaches, and applications for microwave imaging are analyzed. Several limitations and points of interest with the current techniques are found. The limitations motivate the development of five new processing techniques in the field of microwave imaging, all of which can serve to improve the detection of low contrast or low RCS targets. In addition to the five techniques, Chapter 3 presents an analysis of time domain antennas and demonstrates the importance of emphasizing the time domain concepts while designing antennas. Of the five techniques, three techniques, those presented in Chapters 2, 4, and 5, introduce new techniques that are generally applicable in microwaving imaging applications and are all demonstrated to improve image quality. The improvement in image quality can improve the detection of low contrast and low RCS targets as improving the SNR and reducing distortion in reconstructed

images will serve to increase the likelihood that the targets will be detected. The remaining two techniques which are presented in Chapters 5, 7, are techniques which directly improve the detection of low contrast and low RCS targets in specific applications.

1.7.2 Contributions of Chapter 2

In this chapter the characteristics of the near-field of UWB antennas is analyzed. The impact of the near-field on microwave imaging had previously been introduced in [16]. Here a further understanding of this principle is presented and a novel method to mitigate this principle is discussed. First this work builds off previous works [21]–[23] and uses a Huygens dipole expansion to model the fields of the antenna as they travel from the antenna to the far field. Then the near-fields of a variety of UWB antennas are shown. Because the apertures of the antenna can no longer to easily described, this motivates a new method to model the near-field of the antennas. This novel technique involves characterizing a transceiver by finding a version of the so called "point spread function". In this case the function consists of a model of the time of flight of a signal from the transceiver, to a point target and back to the transceiver for any point as a function of distance from the transceiver and θ. This transceiver characterization is then incorporated into the image reconstruction algorithm, in this case the Global Back Projection algorithm, in order to improve imaging in the near-field. This technique is then validated using both simple and more complicated examples. It demonstrates improvement in imaging and mitigation of the effect of the near-field.

1.7.3 Contributions of Chapter 3

In this chapter a novel antenna, designed specifically for the time domain is presented. The design process emphasizes the importance of using metrics from the time domain when designing antennas for imaging using time domain techniques. Different techniques for analyzing antennas in the time domain such as phase centre analysis, radiation analysis are

compared with well known frequency domain techniques. Imaging done by collecting data in the time domain is compared to imaging done using the frequency domain. To conclude the chapter the quality of the antenna is presented by demonstrating a particularly difficult imaging situation in which the antenna is successful.

1.7.4 Contributions of Chapter 4

The chapter presents an original algorithm to detect scatterers from sinograms. The algorithm is able to rigorously detect the reflections of the major scatterers in the received data. Using this algorithm and localization principles, the spatial locations of the major scatterers can be then found. With the knowledge of the spatial locations of the major scatterers, this chapter then demonstrates that this information can be used to synthesize new radar data for arbitrary aperture locations, and subsequently, improve the reconstructed images using the additional data. This shows that image distortion has been reduced and this technique can enhance image quality.

1.7.5 Contributions of Chapter 5

In target scenes with regions of differing group velocities, the state-of-the-art imaging technique when using reconstruction techniques like the Global Back Projection technique is to use an weighted average value for the group velocity in the target scene. In this chapter a novel technique is presented. This technique can be applied when there is circular symmetry in the target scene. This technique uses the symmetry to segment the target scene and use different group velocities for the different regions. The different regions are detected using the scatterer algorithm demonstrated in Chapter 4. The technique is validated by both full wave simulations and experiments. This demonstrates that this is an improvement over using the average group velocity.

1.7.6 Contributions of Chapter 6

Harmonic radar is well understood and has been used in some interesting applications [24]–[27]. This chapter proposes the a novel time domain version of the harmonic radar, which seeks to supress linear clutter and find objects such as diodes and transistors which have non-linear scattering properties while scattering electromagnetic pulses. This new technique is demonstrated using simulations and further validated using simple experiments.

1.7.7 Contributions of Chapter 7

This chapter introduces a technique which is common in the ultrasound community but has not been previously applied to microwave sensing and imaging. This technique is customized and modified to fit the field of microwave imaging, specifically stroke detection and classification. Here full-wave simulations demonstrate the possibility of using this technique to suppress stationary clutter and detect movements over time in radar imaging.

Chapter 2

UWB Sensor Characterization for Radar Sensing and Imaging in Superluminal Propagation Regions

2.1 Introduction

Depending on the application, radar might need to be employed in the near field of the target. Imaging in the near field has many benefits, such as high measurement accuracy, limited space requirements, and the potential to increase the SNR [28]. However, imaging in the near field of the antenna adds complexity [28]–[31]. Despite this added complexity, near field imaging has been used in many recent developments such as biomedical imaging [32]–[39], bore-hole imaging [40], and industrial imaging [41], [42]. The present near field imaging techniques account precisely for the wavefront curvature and free space propagation loss, but not for the unique properties of electromagnetic pulses in the near field.

In the time-domain, the near field complexities manifest as a changing pulse shape and superluminal propagation [16]. Strictly speaking, the radiated pulse changes its shape as it propagates in the antenna near field. There has been significant research on antenna characterization and the study of time-domain antennas [20], [43]–[49]. Recently, it has been shown that pulse shaping and superluminal propagation in the near field can affect image reconstruction [16]. The impact of using the incorrect pulse velocities in imaging applications

has also been demonstrated.

In this chapter, we propose a method to account for the near field effects on imaging by characterizing the time-domain behaviour of the sensor in the field of view. This study includes characterizing the radiated pulse from the antenna and the scattered pulse from the target. It is expected that the scattered pulse changes pulse shape in the near field of the target, as well as having superluminal velocities. By tracking the time of flight, and the distance, specific pulse characteristics such as pulse-peak velocity [50], take to arrive at locations in the target scene during the characterization step, the apparent velocity of the pulse can be obtained and used to account for the near field effects in the image reconstruction.

The characterization of the transceiver can then be used to account for the superluminal behaviour of the near fields in imaging or other applications where the time of flight of the pulse-peak is used. We then show the impact of using the characterized pulse velocity in imaging applications, and present experimental verification to validate the near field radar imaging.

2.1.1 Theoretical Basis

Dipole radiation in the time-domain can be derived using the time retarded Hertz vector method [16], [51]. The radiated electric and magnetic fields are written as

$$\vec{E}(r,t) = \frac{1}{4\pi\epsilon_0}\left\{\hat{\theta}\frac{\sin\theta}{r^2}\left[\frac{p(\hat{t})}{r} + \frac{1}{c_0}\frac{dp(\hat{t})}{dt} + \frac{r}{c_0^2}\frac{d^2p(\hat{t})}{dt^2}\right] + \hat{r}\frac{2\cos\theta}{r^2}\left[\frac{p(\hat{t})}{r} + \frac{1}{c_0}\frac{dp(\hat{t})}{dt}\right]\right\} \tag{2.1a}$$

$$\vec{H}(r,t) = \hat{\phi}\frac{\sin\theta}{4\pi r^2}\left[\frac{dp(\hat{t})}{dt} + \frac{r}{c_0^2}\frac{d^2p(\hat{t})}{dt^2}\right] \tag{2.1b}$$

where $p(t)$, l, $\hat{t} = t - (r/c_0)$ and c_0 are the time-varying dipole moment, the length of the radiating dipole, retarded time, and speed of light in vacuum respectively. Additionally, θ is the angle between the vector along the dipole axis and the vector that joins the centre of the dipole to the observation point. The dipole moment and antenna excitation current

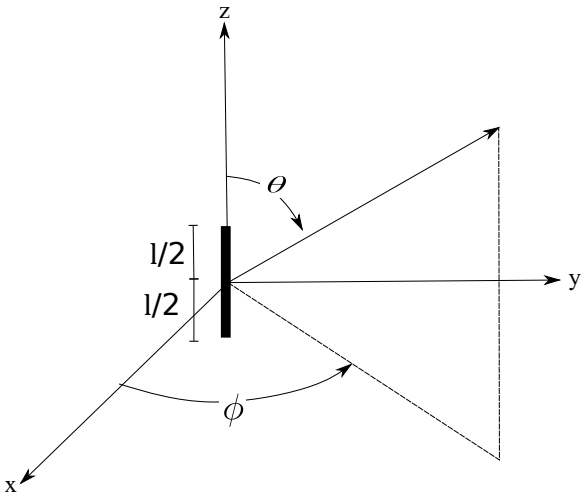

Figure 2.1: Infinitesimal dipole antenna.

are related through $i(t) = (1/l)(dp(t)/dt)$. As shown in (2.1), the radiated pulse is a superposition of three different components, which vary with $1/r^3, 1/r^2$ and $1/r$. Very close to the antenna, in the near field, the $1/r^3$ term dominates. As the observation point moves away from the antenna, into the far-field, the $1/r$ term dominates. The superposition of these waves changes the pulse shape with distance in the near field. The coherent addition of these waves forms the radiated pulse peak. The changing pulse shape makes the pulse shape travel at superluminal speeds, despite that all the individual terms in (2.1) are luminal. Once the pulse reaches the far-field, the contribution from the first two terms becomes negligible, and the pulse shape ceases to change and becomes stable [16].

In the special case where, $p(t)$ takes the form of a Gaussian pulse, the terms of the transverse electric field component ($\hat{\theta}$), for $\theta = 90°$, i.e. fields in peak radiation direction, become:

$$E_1 = \frac{1}{4\pi\epsilon_0 \mathbf{r}^3} P \tag{2.2a}$$

$$E_2 = \frac{1}{4\pi\epsilon_0 \mathbf{r}^2 c_0} \frac{-2(t-t')}{\tau^2} P \tag{2.2b}$$

$$E_3 = \frac{1}{4\pi\epsilon_0 \mathbf{r} c_0^2} \frac{2}{\tau^2} \left(\frac{-2(t-t')^2}{\tau^2} - 1 \right) P \tag{2.2c}$$

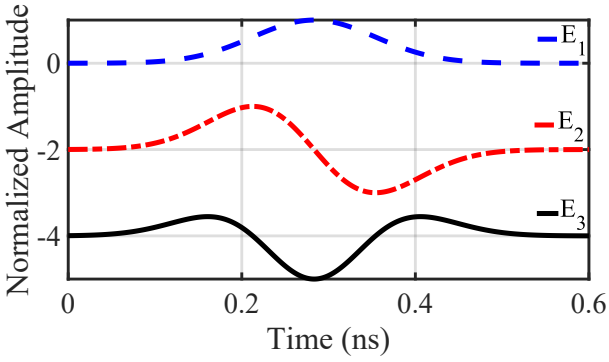

(a)

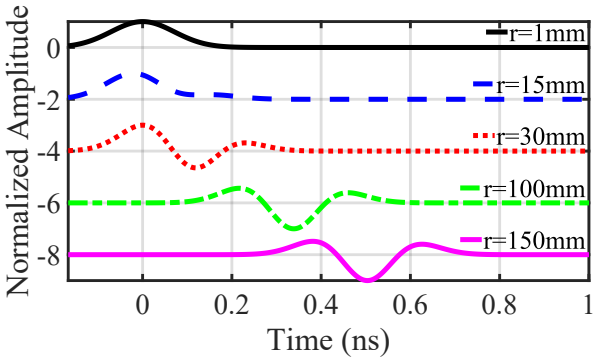

(b)

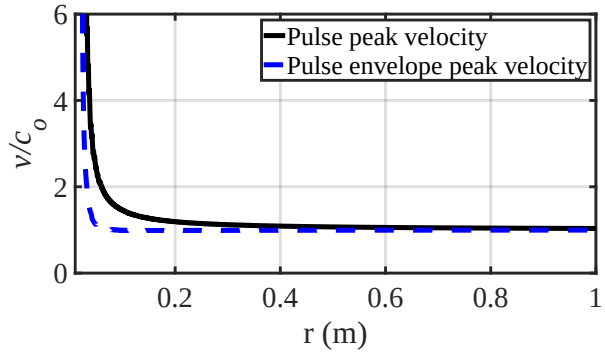

(c)

Figure 2.2: Dipole radiation of 1st derivative Gaussian pulse of bandwidth 6 GHz, for $\phi = \pi/2$; (a) Various pulse components of the radiated pulse at r=1 cm. (b) Total radiated pulse at different distances from the dipole. (c) Calculated pulse-peak and envelop velocity.

where

$$P = exp\left(-\left(\frac{t-t'}{\tau}\right)^2\right) \tag{2.2d}$$

$$t' = \frac{r}{c_0} \tag{2.2e}$$

$$E_T = E_1 + E_2 + E_3 \tag{2.2f}$$

where E_T is the total radiated field. The relationship between τ and the pulse's -20 dB bandwidth (BW) can be approximated to be [52]:

$$\tau = \frac{1}{2 \times BW\sqrt{ln(2)}} \tag{2.3}$$

The pulse components and the combined waveforms are plotted in Fig. 2.2. Fig. 2.2(b) shows the change in the radiated pulse shape over distance as the dominance of the various components varies as a function of distance.

The superluminal behaviour of the electromagnetic wave can be associated with one of the following wave interaction mechanisms: anomalous dispersion [53], evanescent propagation [54] or wave interference [55]. Different components of the radiated pulses change in a way which alters the shape of the radiated pulse as it moves from the near field into the far-field. Once in the far-field the pulse maintains a constant shape and the peak of the radiated pulse is luminal. However, in the near field when tracking the peak of the pulse, it will appear to propagate faster than the speed of light due to pulse reshaping. In microwave imaging, the peak of the pulse is often used as an indicator of the targets' positioning. Therefore, it is important to use the actual speed at which the peak of the pulse moves as opposed to an assumption that the pulse moves at the speed of light in the near field as well.

2.2 Characterization of Transmitted Pulse

This section discusses the radiated pulse shaping and speed of the radiated pulse-peak in the near field of UWB antennas. Several analytical and numerical techniques are

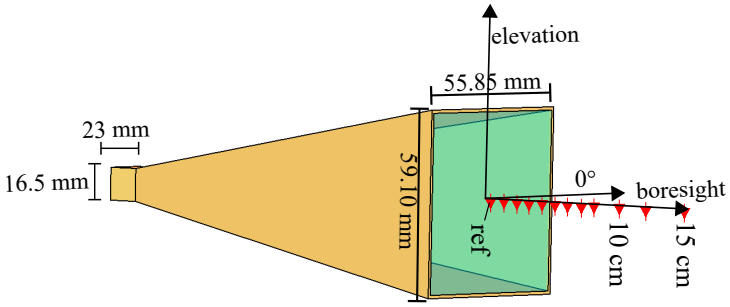

(a)

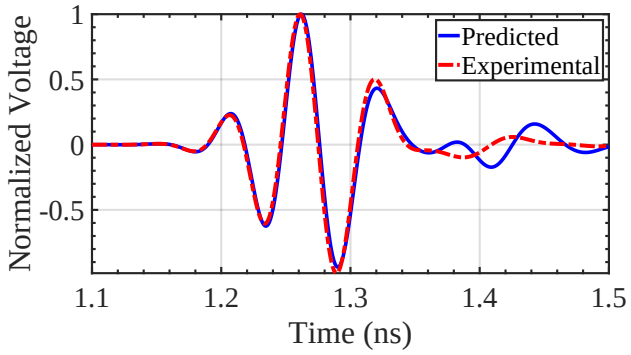

(b)

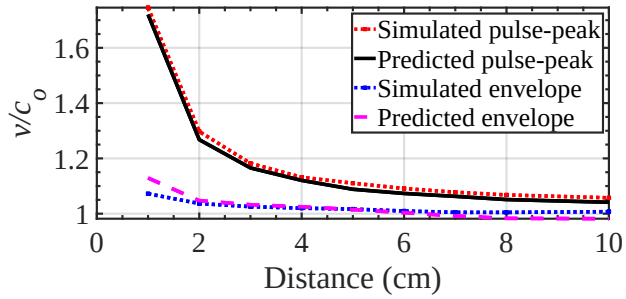

(c)

Figure 2.3: (a) Experimental setup. (b) Comparing the predicted and measured radiated pulse at a distance of 3 cm. (c) Comparing the simulated pulse-peak and pulse envelop velocities as a function of distance.

available in the literature to compute the radiated fields of an aperture antenna [21]–[23]. However, in this paper, a simple and straightforward Huygens-Fresnel principle is used to illustrate the physics behind the pulse shaping and pulse superluminality of the radiated pulse. Based on the Huygens principle, the antenna aperture fields can be replaced by a number of infinitesimal dipoles with excitations proportional to the aperture field amplitude and appropriate time delay. Radiation from the aperture is represented by the superposition of radiation from individual dipoles.

To illustrate the problem, consider a pyramidal horn shown in Fig. 2.3(a). The pulse radiating from the simulated horn antenna is a Gaussian modulated sin wave, whose frequency ranges from 6.4 to 8 GHz. The fields of the horn can be approximated to be $cos(\frac{x\pi}{b}$. If the peak of the pulse is considered as the reference for the time of the pulse, then with respect to the plane of the antenna aperture, the speed of the pulse can be seen to vary spatially and then exceeds the speed of light. The measured radiated pulse and predicted radiated pulse, based on (2.1) and the antenna aperture fields, at a distance of 3 cm are shown in Fig. 2.3(b). In Fig. 2.3(c), the simulated pulse-peak velocity using CST Microwave Studio and the predicted pulse-peak velocity, as well as the predicted and simulated pulse envelop velocities are compared. The number of dipoles used in the dipole expansion is a $81x81$ grid. Increasing he dipole expansion above this number did not show improvement. As can be seen from the comparison, the predicted, measured, and simulated results show good agreement despite the simplicity of the model. Measuring the radiated pulse in the near fields ($\leq$ 2 cm) of the antenna is difficult as the receiving antenna cannot be treated as a point receiver.

2.2.1 Printed UWB Antennas

To confirm and illustrate the near field effect on the radiated pulse, several frequently used printed antennas such as Vivaldi and monopole antennas were considered. Because the radiating aperture of the printed antennas is not strictly defined by a metallic boundary,

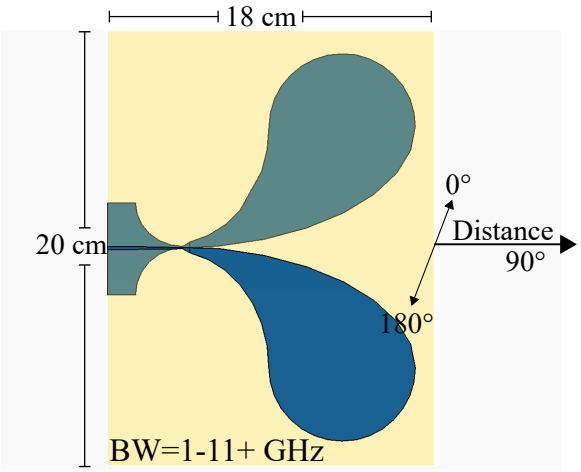

(a)

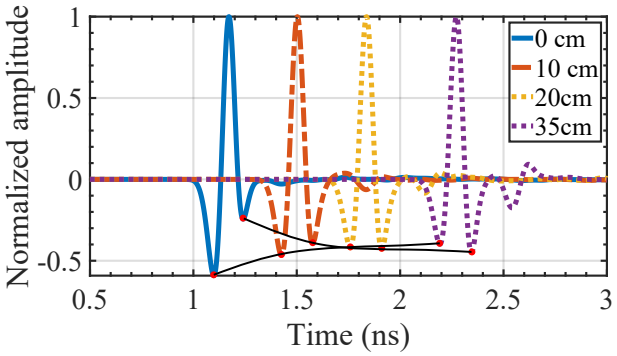

(b)

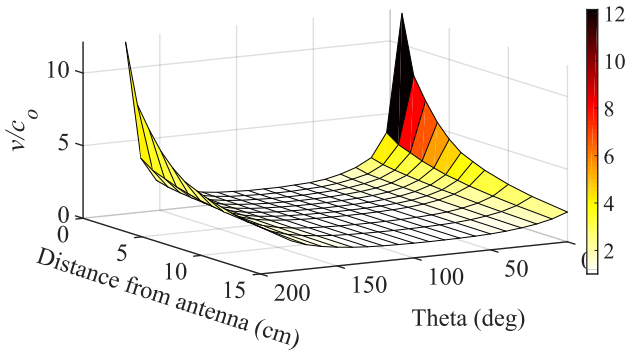

(c)

Figure 2.4: Simulation of the radiated pulse and pulse-peak velocity in the near field of the antenna. (a) Image and specification of the Vivaldi antenna. (b) Normalized radiated pulses at various distances along the boresight of the antenna, showing the pulse shape changing as it travels to the far field. (c) Pulse-peak velocity in the azimuthal plane of the antenna.

analytically capturing the aperture fields between the antenna leaves or currents on the antenna surface is very challenging. Therefore, this study includes only simulation results, not theoretical ones. Fig. 2.4(a) shows the image of a Vivaldi antenna (18 cm x 20 cm) whose operating frequency ranges from 950 MHz to 11 GHz [15]. Fig. 2.4(b) shows the radiated pulses by the antenna as a function of distance. The input pulse to the antenna is a first derivative Gaussian pulse with a FWHM pulse width of 62 ps. Very close to the antenna the radiated pulse looks closer to the input pulse, whereas in the far field the radiated pulse is a time derivative of the input pulse. The pulse-peak velocity in the azimuthal plane of the antenna is shown in Fig. 2.4(c), which is superluminal in the near field.

In addition to the previous results, this study includes two more Vivaldi antennas. One is the miniaturized Vivaldi antenna shown in Fig. 2.5(a), and the second antenna is a Vivaldi antenna with a higher cut-off frequency, shown in Fig. 2.5(c). Along with Vivaldi antennas, a printed monopole antenna (shown in Fig. 2.5(e)) is also studied. Figures 2.5(b), 2.5(d), and 2.5(f) show the simulated pulse-peak velocity of the radiated pulses, respectively.

This study concludes that the radiated pulse changes its shape as a function of distance from the antenna. In the near field, very close to the antenna, the radiated pulse looks more like the input pulse, whereas far from the antenna, the radiated pulse is a time derivative of the input pulse. Pulse-peak velocity also varies from near field to far field. In the near field, it is superluminal; however, in the far field it is luminal.

2.3 Reflected Pulse Characterization

Characterization of a reflected pulse from the metal surface can be studied based on the induced surface current profile and dipole radiation mechanism shown in (2.1a). For easy experimentation, in order to create a reflector with a large near field distance, a metal sheet of 28 x 28 sq. cm is illuminated with a radiated pulse. The experimental set up is shown in Fig. 2.6(a). The reflector is positioned at the far field distance from the transmitting antenna. Based on the radiation pattern of the transmitting antenna shown in Fig. 2.6(b)

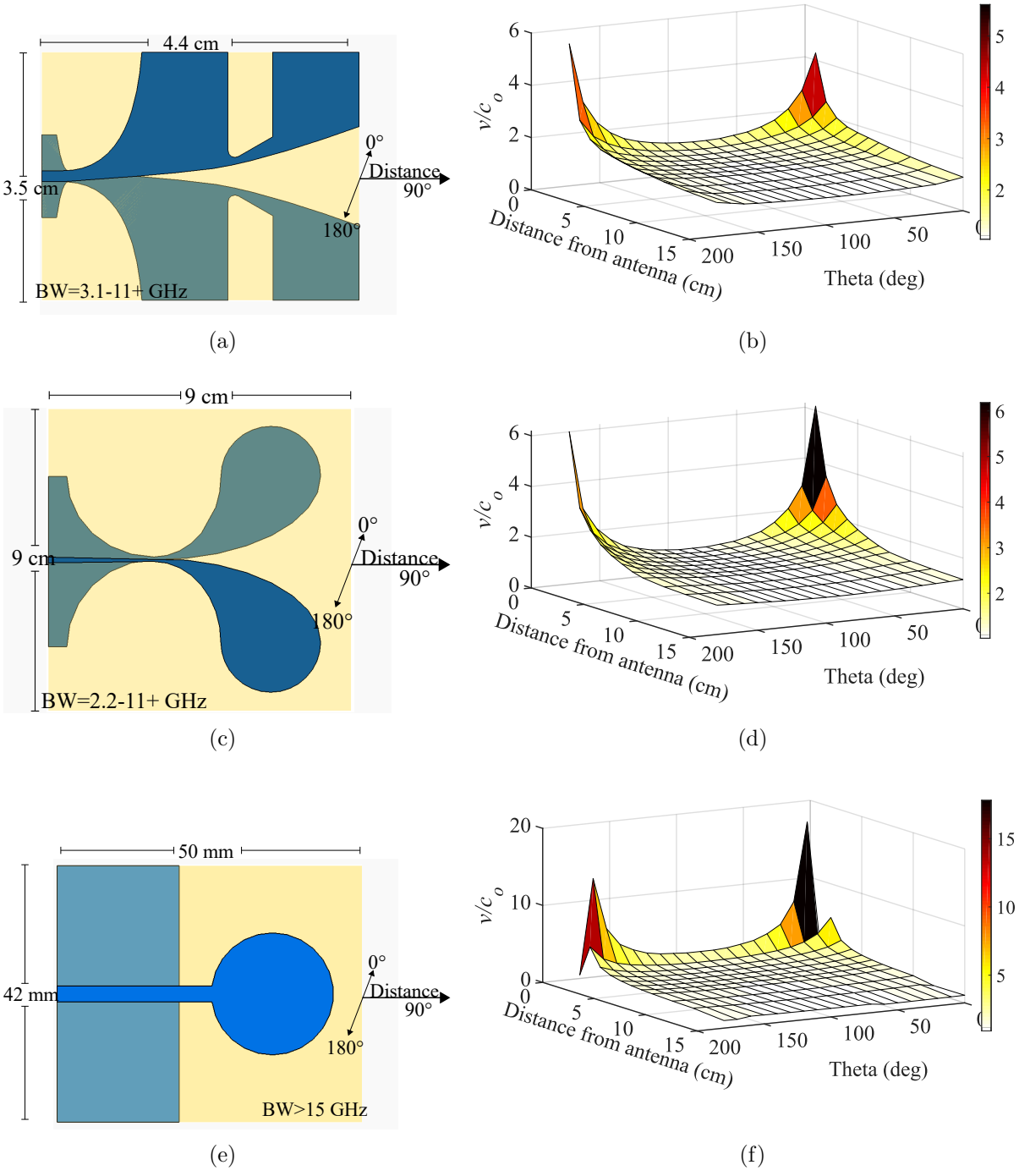

Figure 2.5: The simulated pulse-peak velocity in the azimuthal plane of miniaturized Vivaldi antenna (Antenna-1), Vivaldi antenna with a lower cut-off frequency of 2.2 GHz (Antenna-2), and printed monopole (Antenna-3). (a) Image and dimensions of Antenna-1. (b) The pulse-peak velocity of Antenna-1. (c) Image and dimensions of Antenna-2. (d) The pulse-peak velocity of the Antenna-2. (e) Image and dimensions of Antenna-3. (f) The pulse-peak velocity of the Antenna-3.

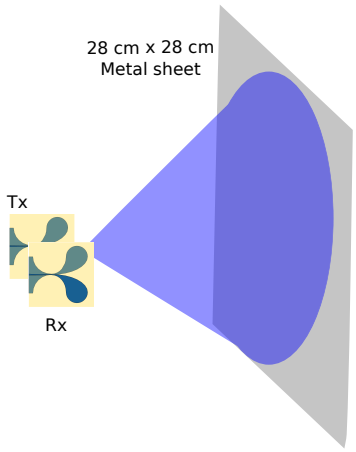

(a)

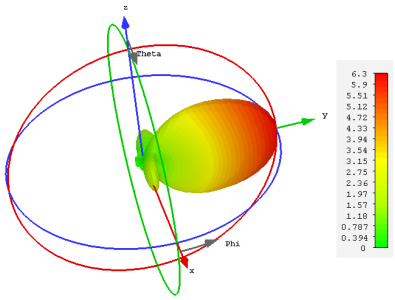

(b)

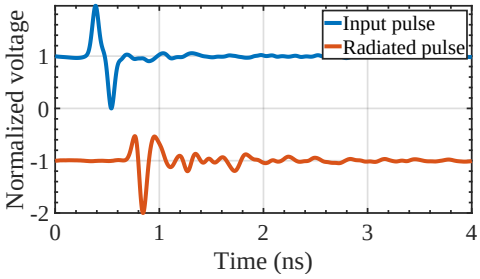

(c)

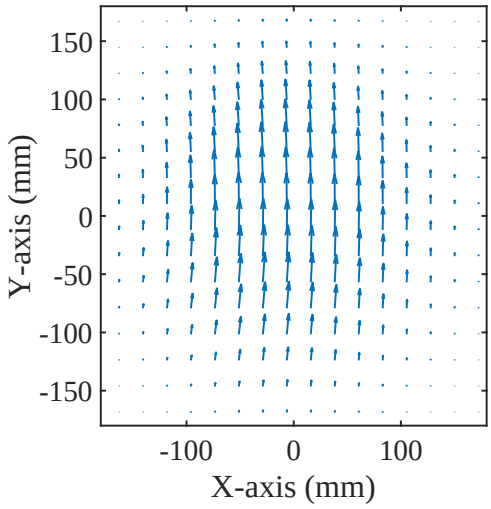

(d)

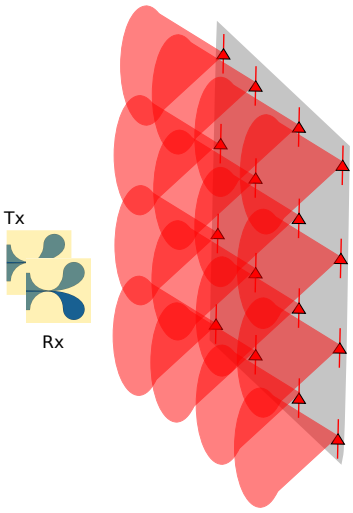

(e)

Figure 2.6: Characterization of the reflected pulse, (a) Experimental setup. (b) Transmitting antenna radiation pattern. (c) input pulse to the transmitting antenna and the radiated pulse that incidents on the reflector surface. (d) Induced current distribution on the reflector surface at an instant of time. (e) Reradiation of the reflected pulse from the surface currents on the reflector.

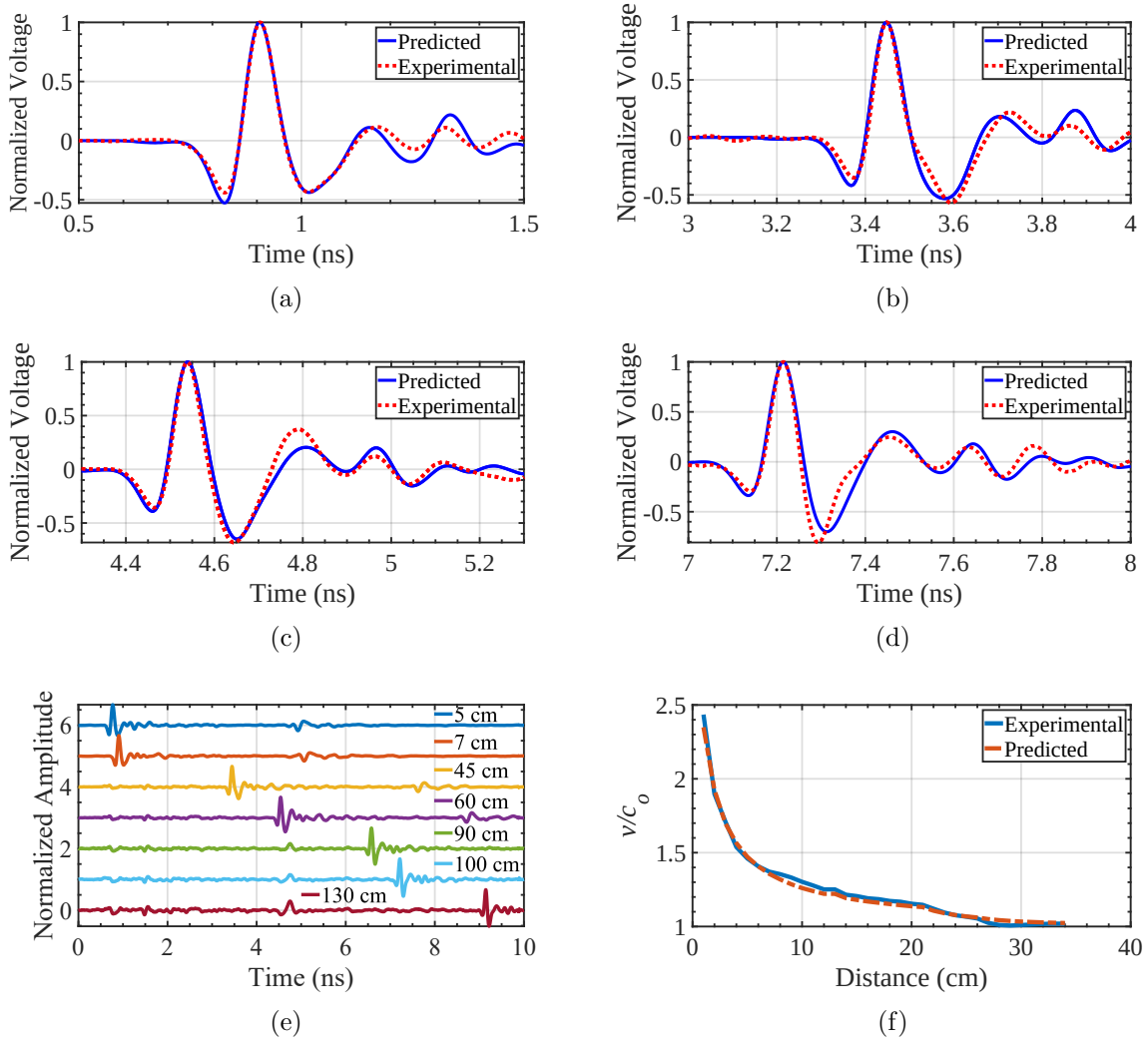

Figure 2.7: Comparison of predicted and measured reflected pulses at: (a) A distance of 7 cm, (b) at a distance of 45 cm, (c) at a distance of 60 cm, (d) at a distance of 100 cm. (e) Measured time of flight of the reflected pulse as a function of distance. (f) Pulse-peak velocity of the reflected pulse.

and profile of the transmitted pulse shown in Fig. 2.6(c), as a function of time, the induced currents on the reflector surface can be computed, as shown in Fig. 2.6(d). The reflected pulse is re-radiated from the surface currents on the reflecting surface, as shown in Fig. 2.6(e), which can be calculated based on the Huygens principle and dipole radiation shown in (2.1a). A comparison of these results with the experimental results is shown in Fig. 2.7 when the receiving antenna is moved different distances from the reflector.

The reflected pulse very close to the surface is essentially the inverse of the incident pulse, which explains the reflection coefficient of -1 on the metallic surface. However, as shown in Fig. 2.7(a)- 2.7(d), the reflected pulse shape changes as a function of distance from the reflecting surface, which is due to the superposition of contributions from various points on the reflector. In the far field, the reflected pulse is a time derivative of the incident pulse, which can be explained based on (2.1a). The agreement between theoretical predictions and measurements is excellent.

Fig. 2.7(e) shows the time of flight for the reflected pulses at different distances from the reflector to the Vivaldi antenna. The time of reference for these calculations is the time of reflected pulse for the case on which the reflector is placed on the face of the transceiver antennas. It includes all the time delays that occurred in pulse sources and cables, the delay due to antenna group delay. As shown in Fig. 2.7(f), based on the distance and time of flight, the pulse-peak velocity is calculated, and is then compared with the theoretical calculations. Both the measured and predicted pulse-peak velocities match very well and show the superluminal behaviour of the pulse in the near field of the reflector.

2.3.1 Radar Transceiver Characterization

Many commonly used antennas are difficult to analytically characterize, because their radiating apertures are not strictly defined by a metallic boundary. Therefore, an experimental method is used to understand the behaviour in the near field.

Radar image reconstruction methods, such as the GBP algorithm [56], rely on accurate knowledge of the speeds of the pulse in the target scene in order to create high-quality

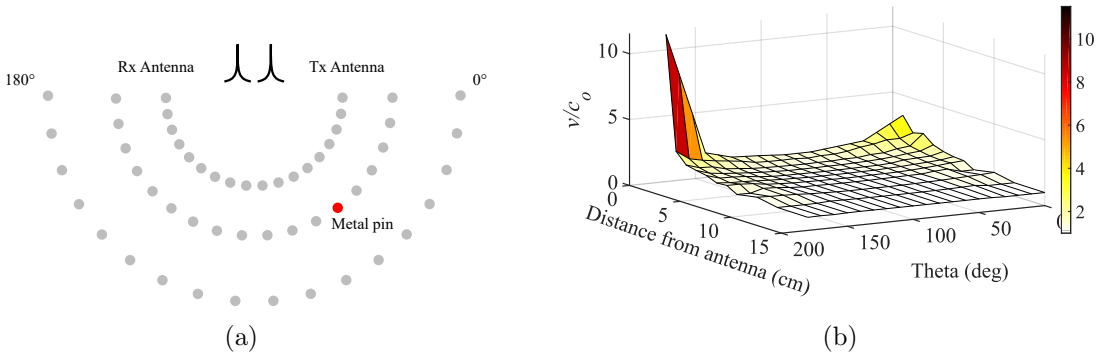

Figure 2.8: (a) Transceiver characterization setup. (b) Matrix of speeds of the pulse-peaks compared to c_0

images. Thus, one simple way to characterize the behaviour of radar transceivers in the near field for imaging is to measure the actual time it takes for the pulse to be transmitted, reflected and received by the transceiver, for a point target positioned at any location in the target scene. This is done by placing the transceiver as shown in Fig. 2.8(a). A small metal pin is placed one by one at all the locations, and the responses are measured. The experiment is calibrated using the same procedures as described in [57]. The received signal is then processed to determine the time delay taken for various features of the pulse. Here, the features of interest are the pulse-peak, the pulse envelop peak, and the first minima. Both the time delay for these features and the location of the pin allows for the calculation of the apparent speeds that these features travel in the target scene. The metal pin was placed in front of the transceiver at 1 cm intervals from 1 cm to 15 cm, with spacing of 10° from $0° - 180°$. Fig. 2.8(b) shows the apparent speeds of the pulse-peak when the transceiver consists of two miniaturized Vivaldi antennas [16]. The pulse-peak velocity decreases farther away from the antenna and varies rapidly in off boresight directions. Fig. 2.9(a) shows the boresight speeds of some of the pulse characteristics. Fig. 2.9(b) shows the speeds of different pulse features at a 60° off-boresight direction, i.e. 30° and 150° directions. Fig. 2.9(c) shows the pulse-peak speeds at different angles. Once characterized in this manner, the speed profile of a transceiver can be used in image reconstruction as is demonstrated in the following section.

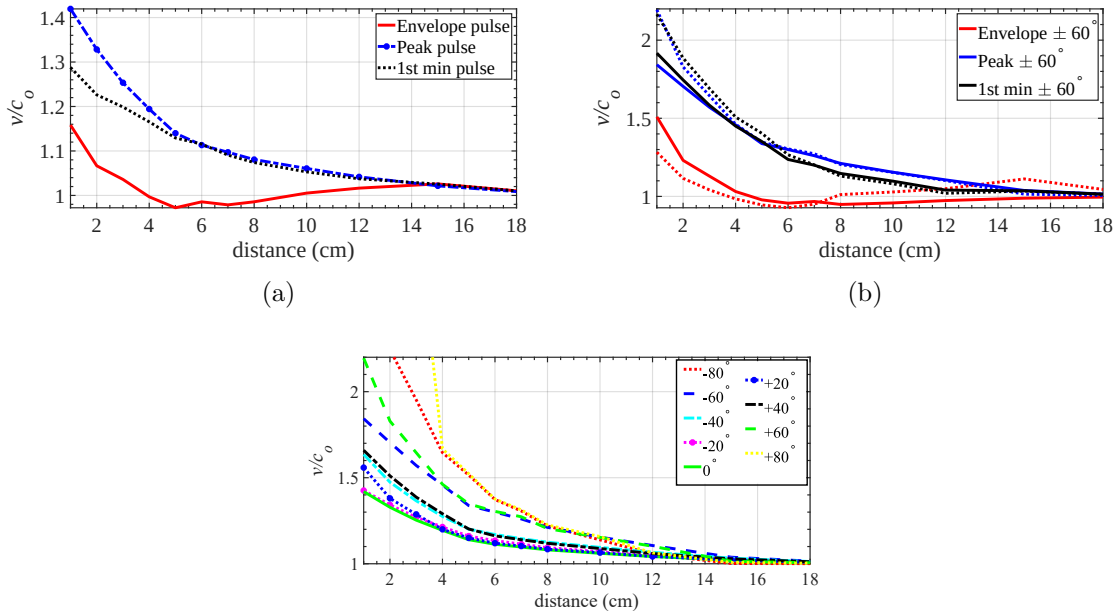

Figure 2.9: (a) Near field speeds of different features of pulse in boresight direction. (b) Near field speeds of different features of pulse in ±60°. (c) Near field speeds of the pulse-peak in various directions.

2.4 Imaging in the Near Field

This section examines several imaging examples using circular and linear synthetic aperture radar configurations in the radar near field. In each case the image is generated using both the conventional assumption that the pulse velocity is c_0 and the characterized pulse-peak velocity. The impact of the superluminal speed of the radiated and reflected pulses on the radar imaging is investigated. Synthetic aperture radar (SAR) techniques and global back projection (GBP) image reconstruction methods are analysed in the near field of the radar. This study includes both theoretical and experimental validation. In these experiments, the input pulse to the transmitting antenna is the first derivative Gaussian pulse of FWHM pulse width of 48 ps, and the receiver is a sampling oscilloscope of bandwidth 18 GHz. The transceiver consists of a transmitting and receiving antenna, which are miniaturized Vivaldi antennas [16]. The transmitter and receiver are placed side by side and are separated by 1cm. The pulse generator for these experiments is the AVTECH AVP-3SA-C which

generates a chain of 10 V steps at 1 MHz pulse repetition frequency [57]. The digital sampling oscilloscope collects the received pulses with a time average of 64 samples. The data for the experiments are processed in the following manner: The data are interpolated from the 4050 datapoints to 10000, next the data is passed through a low pass filter. At that point the data is aligned to minimize drift, next, the ambient pulse is subtracted from the data. The data is then time gated to remove as much residue of the ambient scene as possible. The time domain back projection is then performed on that data.

These experiments are important as the theoretical evaluation excludes the experimental errors and shows the effect of only near field characteristics, whereas the experimental validation shows the near field imaging accuracy and potential industrial applications.

2.4.1 Point Target Simulation

This section uses point target simulation data, which avoids experimental errors, to illustrate the effect of using different group velocities on target ranging and image reconstruction. The data is generated using point targets and applying the measured pulse-peak speed profile as a function of (r, θ). The profile is measured for the miniaturized Vivaldi transceiver, as shown in Fig. 2.8(b). The initial set-up for this demonstration is shown in Fig. 2.10(a), where the circular synthetic aperture radar configuration of transceivers is considered, and their locations are shown as red crosses. The point targets are shown as black circles. Fig. 2.10(b) shows the raw data collected from the aperture locations. Using the Global back projection, the image of the target scene has been reconstructed.

The reconstructed image using c_0 as propagation speed is shown in Fig. 2.10(c). Alternatively, the image reconstructed using the same speed profile that was used to generate the data is shown in Fig. 2.10(d). Green stars indicate the actual location of the targets. These figures illustrate that the images reconstructed using superluminal speeds show the point targets in their correct positions. As expected, the reconstruction using the characteristic speeds gives a more accurate representation of the target scene with proper visibility and

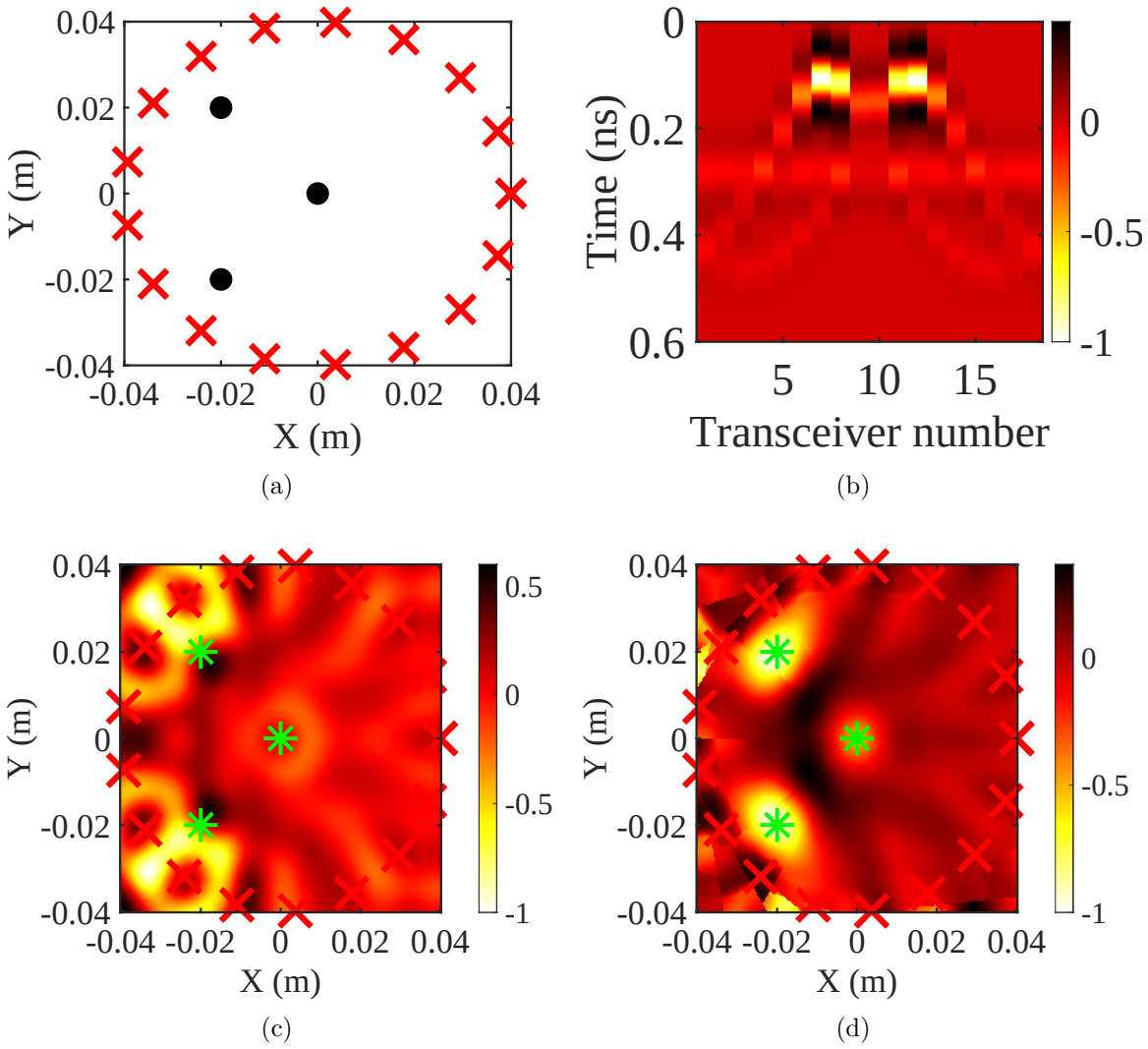

Figure 2.10: (a) Simulation set-up, point transceivers shown as red crosses, targets shown as black circles. (b) Raw data collected from transceivers. Raw image reconstructed using, (c) c_0 and, (d) characteristic speeds. Transceiver locations are shown as red crosses, actual target locations are shown as green asterisks.

precise ranging.

2.4.2 Experimental validation of circular SAR Near Field Imaging

In this experiment, the input pulse to the transmitting antenna is the first derivative Gaussian pulse of full width half max (FWHM) pulse width of 48 ps, and the receiver is a sampling oscilloscope of bandwidth 18 GHz. The transceiver consists of a transmitting and receiving antenna, which are miniaturized Vivaldi antennas [16]. The transmitter and receiver are placed side by side and are separated by 1cm. The pulse generator for these experiments is the AVTECH AVP-3SA-C which generates a chain of 10 V steps at 1 MHz pulse repetition frequency [57]. Time averaging using 64 samples is performed in the sampling oscilloscope. The data for the experiments are processed in the following manner: The data is interpolated from the 4050 data points to 10000, next the data is passed through a low pass filter. At that point the data are aligned to minimize drift, next, the ambient pulse is subtracted from the data. The data are then time gated to remove as much residue of the ambient scene as possible. The time-domain back-projection is then performed on that data.

Experiment-1

The experimental set up consists of three nails of 15 cm x 0.75 cm, which are glued to a circular wooden board with a radius of 15 cm, which is shown in Fig. 2.11(a). The transceiver is positioned at the edge of the board such that two of the nails are in the near field of the radar. The board is rotated in increments of 10° to obtain the data that forms the circular synthetic aperture configuration. The image is reconstructed using the global back-projection with different pulse-peak velocity profiles. The reconstructed image using c_0 is shown in Fig. 2.11(b), and the reconstructed image using the measured pulse-peak velocity is shown in Fig. 2.11(c). For comparison, both the images are normalized and are shown with the same colour profile. The image generated using the superluminal speeds has a higher

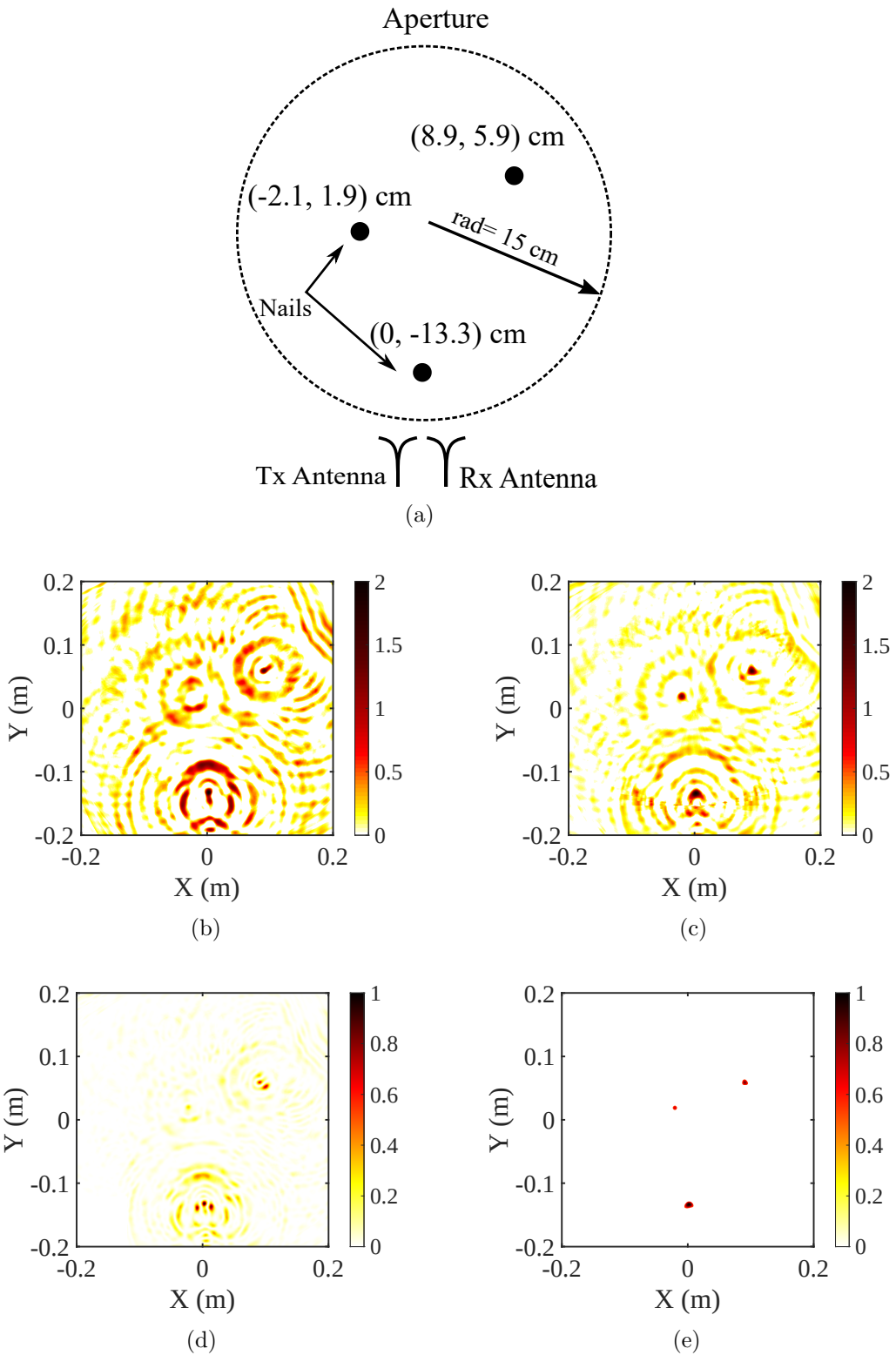

Figure 2.11: (a) Initial experimental setup. Reconstructed images using, (b) c_0, (c) characterized speeds. Threshold images using a threshold of 0.5 for, (d) c_0, (e) Characteristic speeds.

image quality, where the metal nails are clearly visible and positioned more accurately.

To further compare the image quality, a threshold of 0.5 the maximum pixel value, is used for both the images; the results are shown in Fig. 2.11(d) for the case of pulse-peak velocity of c_0, and in Fig. 2.11(e) for the superluminal speeds. In the case of the threshold images, the image generated with superluminal speeds has all three targets above the threshold level and are precisely located, and for c_0 case only two targets are above the threshold level and energy is spread all over. For the image created using c_0, one of the targets was completely missed, and artifacts from the closest target are above the threshold level.

Experiment-2

The experimental set-up consists of four metal pins in the plan of the aperture, arranged as the corners of a square with sides having a length of 2 cm. The transceiver is rotated around the targets with a radius of 5 cm in increments of 10° to obtain the circular synthetic aperture. This set-up is shown in Fig. 2.12(a). The image is reconstructed using c_0 as well as the characterized speed profile. The reconstructed image using c_0 is shown in Fig. 2.12(b), and the reconstructed image using the pulse-peak velocity is shown in Fig. 2.12(c). The reconstructed image using the characteristic speeds is of higher quality. The four targets are visible, wheras in the original image the four targets are completely blended together. There is some experimental error making one of the pins in Fig. 2.12(c) slightly paler than the other pins.

Using the brightest points of the reconstructed image as the location for the pins, we can compare the measured distance from the image to the actual distance of 2 cm used in the experiment. The results are overlayed on the reconstructed image and presented in Fig. 2.12(c). Using c_0, image reconstruction consistently places the locations too close together with an average error of 24%. Using the characteristic speeds (c_{cal}), the sides have a length much closer to 2 cm with an average error of 6%.

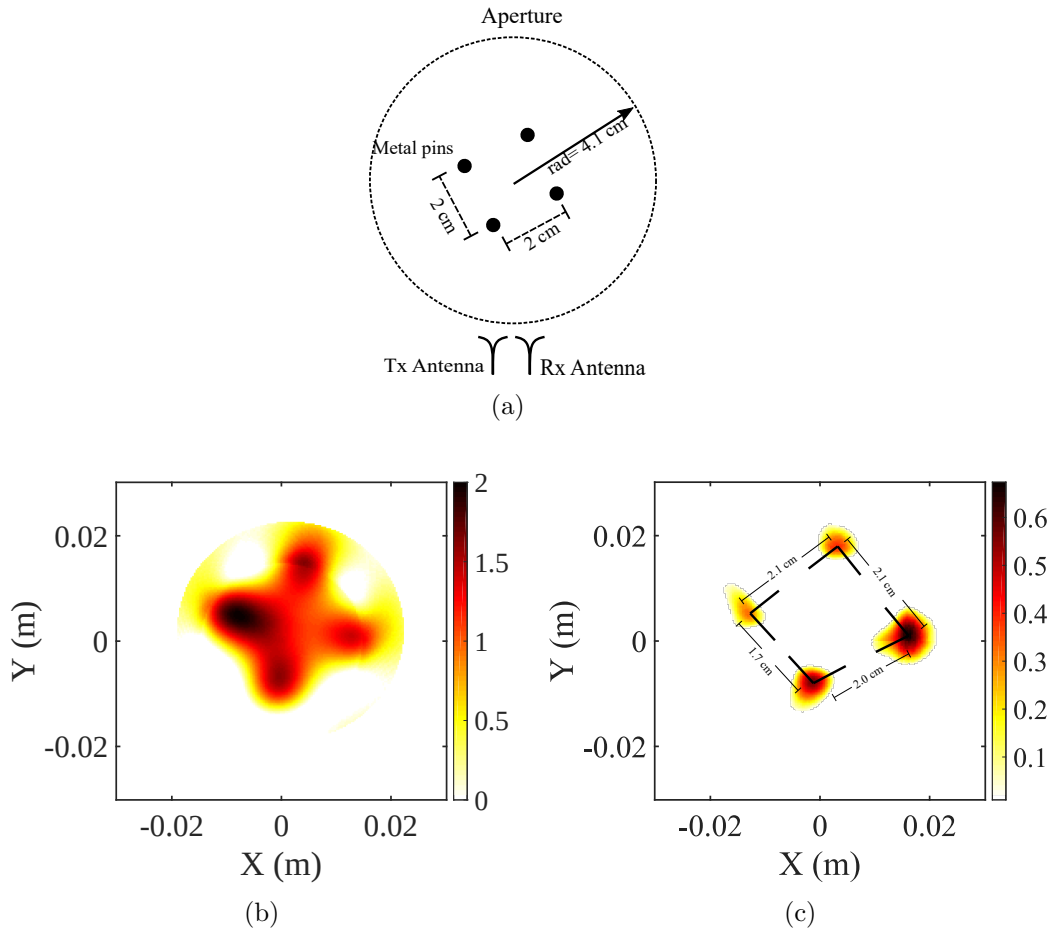

Figure 2.12: (a) Initial set-up with the three point-targets and the measured aperture locations shown with red crosses. Reconstructed images for, (b) c_0, (c) characterized speeds.

2.4.3 Experimental Validation of Linear SAR Near Field Imaging

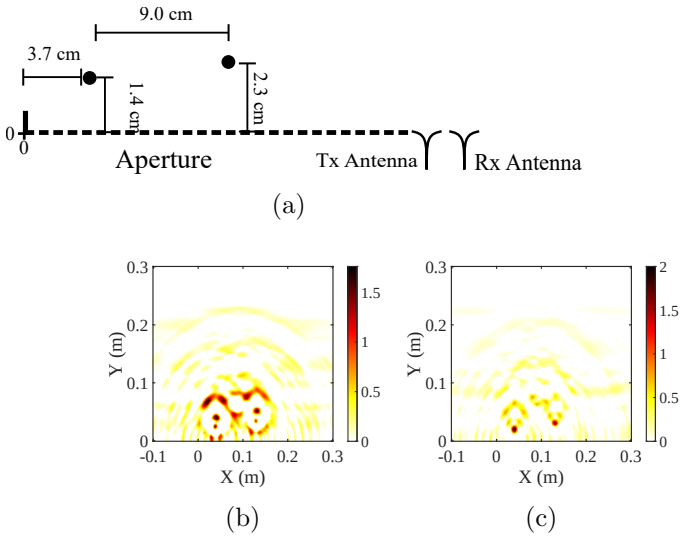

Figure 2.13: (a) Initial experimental set-up. Reconstructed images using, (b) c_0, (c) characterized speeds.

Experiment-1

The experimental set up consists of gluing two nails to a wooden board. This set up is shown in Fig. 2.13(a). The image is reconstructed using the global back projection and different velocity profiles. The reconstructed image using c_0 is shown in Fig. 2.13(b), and the reconstructed image using the pulse-peak velocity is shown in Fig. 2.13(c). Both images are normalized and shown with the same color profile. The reconstructed image using the characteristic speeds has a much higher quality.

Experiment-2

UWB radar has been used for inspection of oil well perforation [58], which is needed to measure the size of perforations in the metal casing as well as corrosion. The experimental set up consists of a metal plate with three holes made in it. The holes are 2.54 cm in diameter and are spaced 5.4 cm and 4.4 cm distance apart. The miniaturized Vivaldi transceiver is

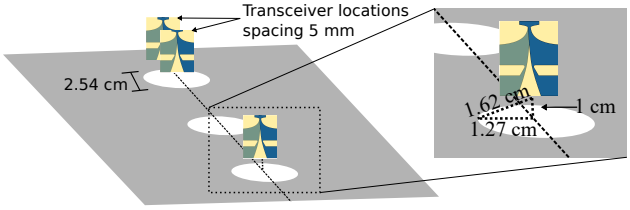

(a)

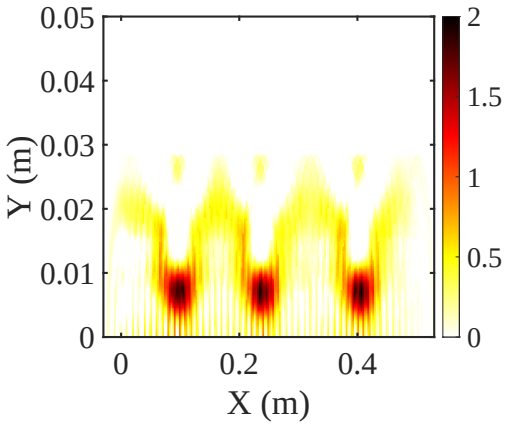

(b)

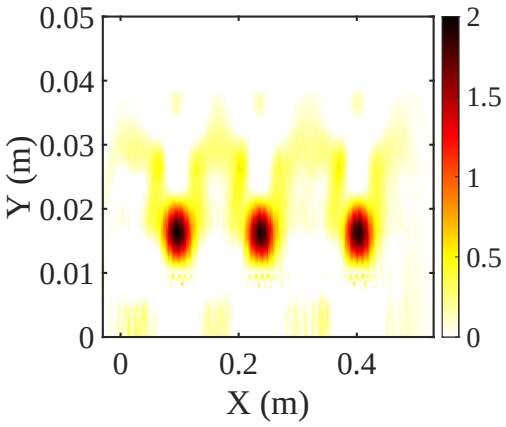

(c)

Figure 2.14: (a) Experimental set-up with the three holes. Reconstructed image using, (b) c_0, (c) characterized speeds.

then passed over the top at a distance of 1 cm above the metal plate. The set-up is shown in Fig. 2.14(a). Images are then reconstructed using c_0 and the characteristic speeds, and the positive images [59] are shown in Fig. 2.14(b) and Fig. 2.14(c) respectively. In both images, the three holes are visible. From these two images we can see that when c_0 is used as the pulse speed the objects are too close and are also blurry compared to the case of characterized speeds.

2.5 Chapter Summary

This chapter summarizes work done furthering the knowledge of time-domain characteristics of radar pulses in the near field, and demonstrates the effect of the near field on radar imaging. A solution to increase image quality when imaging in the near field is proposed. This solution involves characterizing the pulse propagation in the near field of the transceiver pair in use, and then using the characterization of the transceiver in the reconstruction of the image. The full length version of this work is published as [60].

Chapter 3

Time-domain Antenna Characterization and Imaging Impact for Time-Domain Near-Field Microwave Imaging

3.1 Introduction

Antipodal Vivaldi antennas are a popular choice in wireless devices as they provide improved return loss, low cross-polarization, wide bandwidth, and enhanced gain. In this chapter, we present a miniaturized elliptical antipodal Vivaldi antenna. The design is customized based on the input pulse, and its radiation characteristics are analysed for near-field imaging applications. The antenna has an $|S_{11}| \leq -10dB$ from 1.2-11 GHz with a size of 9 cm x 9 cm and a gain of $\geq$7dB along the entire operating bandwidth.

We analysed the important characteristics of the antenna, such as the spread of the phase centre and pulse synchronization of the radiated pulse for the time domain near-field microwave imaging. We then use the antenna to compare time-domain and frequency domain imaging comprehensively. Finally, we demonstrate the antenna's performance using a real-world imaging application.

Typically the antenna designs are characterized by consistent use of frequency-domain analysis. Frequency domain techniques have proved powerful and easy to employ. Today, most communication, worldwide happens with a high frequency sinusoidal carrier which is

modulated by a data signal. As the bandwidth of the modulated signal is small compared to the carrier, the signal is usually treated as a singe tone; and is designed almost exclusively using purely frequency-domain techniques.

When novel UWB antennas are proposed in the literature, they are rarely presented with significant time-domain analysis. Often proposing novel UWB antennas involves purely frequency-domain analysis [61]–[63], or a simple plot of phase delay [64]. This is understandable as most readers are interested in the application to frequency-domain imaging [65], or the use of the UWB antenna in a specific band [66]. However, readers interested in the antenna for time-domain imaging applications [4] will have little idea if the antenna is applicable based purely on frequency-based analysis. For this reason, several analysis techniques are proposed to present the time-domain characteristics of a designed antenna. These include phase centre analysis, Radiation analysis [17], and point spread image validation.

In this chapter, the design of a novel antenna is presented. Frequency-domain analysis in combination with time-domain analysis is presented.

3.2 Antenna Design

To illustrate the time-domain analysis of antennas, we have designed a new customized Antipodal Vivaldi Antenna (AVA). We chose the AVA design as it is simple to construct and easy to use for imaging applications, and there has been much research done on AVA miniaturization. AVA [67] are a commonly used antenna in many wideband applications, such as communication devices in the Ka Band [68], 5G band [69], and UWB bands [70]. Other applications include radar [71], and imaging applications in civil [71], biomedical [71] and elsewhere [71]. AVA antenna are a subset of Vivaldi antennas that tend to have desirable characteristics such as a low side-lobe level, compact size, stable radiation pattern, high operating frequencies, and high front to back ratio [72].

A new antenna is designed as many antennas available in the literature are designed specifically for the FCC-UWB spectrum [73]. These designs are not helpful for many radar imaging applications. In radar imaging applications, signals are radiated locally and can

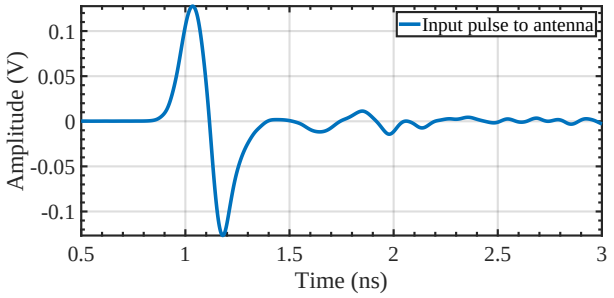

(a)

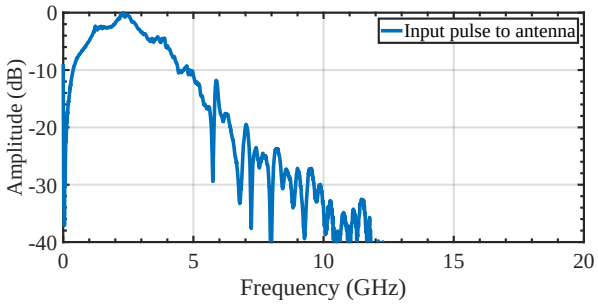

(b)

Figure 3.1: Signal fed to the antenna, (a) Time-domain pulse. (b) Frequency content of input pulse.

be shielded in a restricted area and do not need to conform to FCC regulations. In our design, instead of the FCC spectrum, the antenna is designed to match our Gaussian pulse-shaping network [74]. The resulting input pulse has most of its energy content below 4 GHz. Antennas that accept lower frequencies are often physically larger [15]. Larger antennas are difficult to employ in near-field imaging applications, as they cannot be considered a point emitter, making imaging of small target scenes difficult.

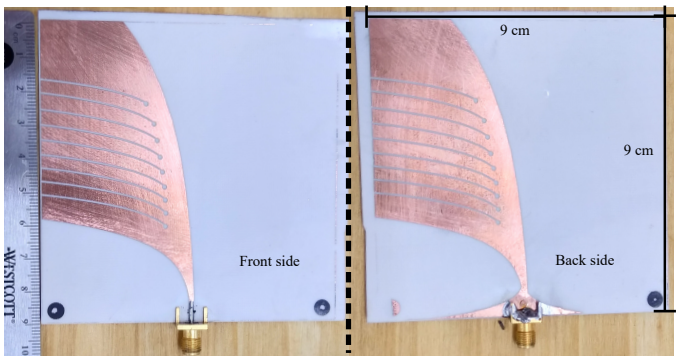

Figure 3.2: Picture of manufactured antenna, both front and back side.

The input pulse for the antenna is of an approximate first derivative Gaussian pulse shown in Fig. 3.1. The frequency profile of the pulse is shown in Fig. 3.1(b). The frequency profile shows, despite the relatively high-resolution nature of the pulse, most of the frequency content is less than 4 GHz. In fact, the -10 dB bandwidth of the pulse is from 0.4 GHz to 4.9 GHz.

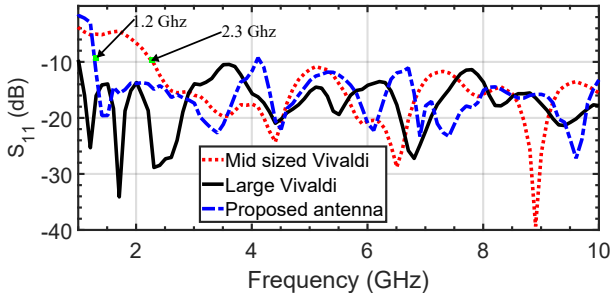

Figure 3.3: S_{11} results comparing a conventional Vivaldi antenna, a size expanded Vivaldi and the proposed antenna. Measured S_{11}.

A conventional antipodal Vivaldi would require an unreasonably large structure to match the spectrum properly [15]. The large size of this antenna is inconvenient for the vast majority of measurement scenarios. Miniaturization of the antenna is therefore desired.

Efficient and complicated, miniaturized Vivaldi antennas have been designed for a myriad of various applications. These enhancement techniques fall into several notable categories, including: slots [73], parasitic patches [75], corrugations [76], adding meta-materials [77], adding dielectric lenses [73], as well as using different versions of the AVA such as the balanced AVA (BAVA) [78] or using the antenna in an array configuration [79]. For our spectrum of interest, we found that slots could achieve sufficient miniaturization. We could not successfully employ other miniaturization techniques without degradation of time-domain behaviour.

To contextualize the proposed antenna, we will compare it to two antennas throughout the chapter. The first is the conventional antipodal Vivaldi antenna of size 9 x 9 cm [80]. This antenna will be referred to as the mid-sized Vivaldi throughout. The second is an enlarged version of the first (18 x 20 cm) [15] and will be referred to as the Large Vivaldi.

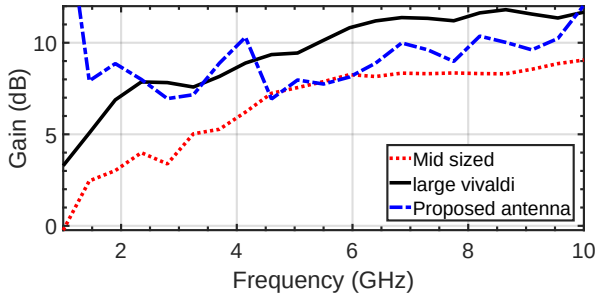

(a)

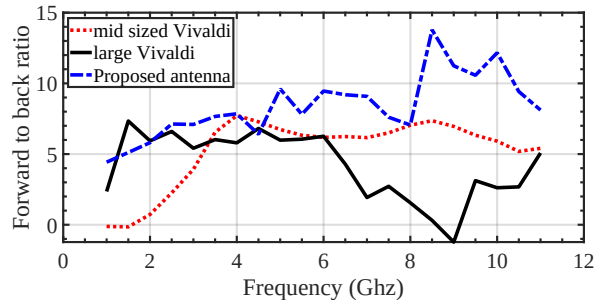

(b)

Figure 3.4: (a) Max Gain comparison between the different antennas over frequency. (b) Front to back ratio comparison between the different antennas over frequency.

The mid-sized Vivaldi has a low-frequency cut-off of 2.3 GHz. The enlarged version has a cut-off of 900 MHz and many desired characteristics such as high gain. However, with an 18 cm x 20 cm footprint, the antenna is inconvenient to use in most imaging applications. The comparison of the measured S11 plots is shown in Fig. 3.2. These results demonstrate that the antenna has a low-frequency cut-off lower than the mid-sized Vivaldi, despite being the same size. The proposed antenna does have a break in its bandwidth at 4.1 GHz, where the S11 rises to -9.2 dB. This is a minor problem and can be ignored.

3.3 Conventional Antenna Analysis

3.3.1 Analysis of Cutoff Frequencies

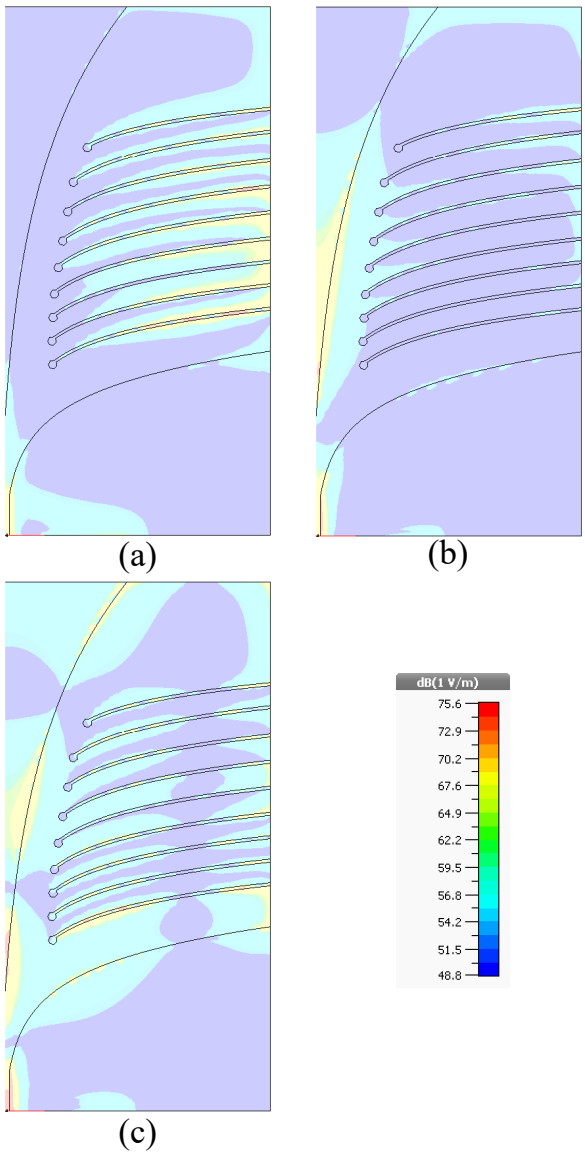

Figure 3.5: Image of simulated E-fields at, (a) 1.3 GHz, (b) 2.5 GHz, (c) 4 GHz.

One can better understand the operating frequencies by viewing the simulated electric fields at various frequencies. The field profile at different frequencies are shown in Fig. 3.5. Fig. 3.5a shows the field at around the low-frequency cut-off. From the figure, the strong fields are extended to the very end of the antenna. Additional lowering of the frequency would mean the fields would be extended past the end of the antenna and cause reflections. Fig. 3.5b shows operation within the operational antenna bandwidth. Fig. 3.5c shows the fields at 4GHz, which is not near the end of the -10 dB spectrum but is towards the end of the important spectrum of the input pulse as detailed in Fig. 3.1(b).

3.3.2 S-Parameters Evaluation

Matching the operating bandwidth of the antenna over as much of the frequency spectrum of the input pulse is traditionally the most important aspect of antenna design. However, as our emphasis is on the time domain, the impact of the spectrum in the time domain should also be analysed.

We placed two copies of the antenna 10 cm from one another, corresponding to the far-field of this antenna, aligned in the bore-sight direction. We repeated this for the mid-sized Vivaldi antenna and the large Vivaldi as well. The antenna input pulses are taken from a pulse shaping network tuned to provide different pulse widths. The radiated pules are shown in Fig. 3.6. Fig. 3.6(a) shows the input pulse corresponding to the spectrum that the antenna was designed for, as shown in Fig. 3.1(b). The received signal from the second antenna is shown in Fig. 3.6(b). This demonstrates that the antenna has an improved gain and an improvement in ringing when compared to the mid-sized Vivaldi. To quantify this we can use a metric of ratio of peak voltage using the pulse to the peak voltage during the subsequent ringing. This figure of merit can be calculated as $FOM = \frac{argmax|V_r|}{argmax|V_p|}$, where V_p is the region of the signal containing the pulse and V_r is the region of the signal not including the pulse. In this case the FOM for the mid sized Vivaldi is 0.26 and the FOM for the proposed antenna is 0.13. This represents an improvment of over 100%. Fig. 3.6(c) shows a different input pulse

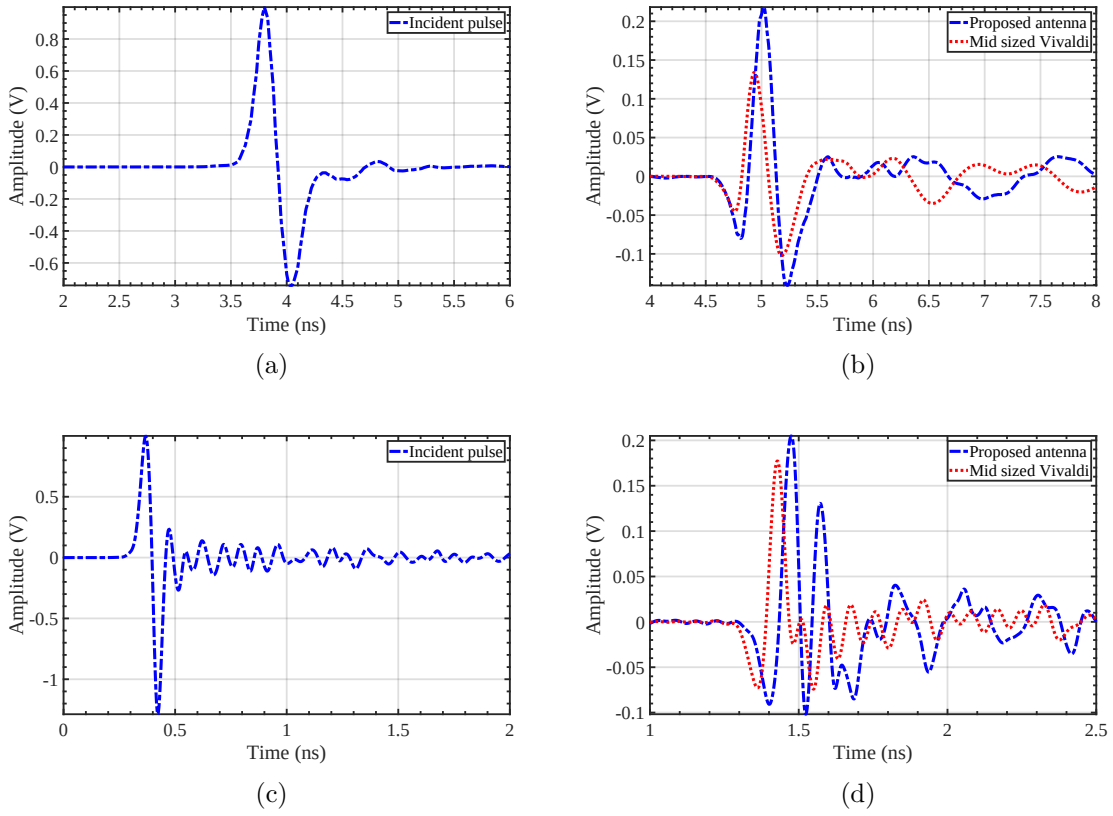

Figure 3.6: Comparison of the miniaturized antenna and the medium sized Vivaldi antenna. (a) Incident pulse to the antennas for the case of 170 ps PW. (b) Received signals from the two antennas for the 170 ps signal. (c) Incident pulse to the antennas for the case of 46 ps PW. (d) Received signals from the two antennas for the 46 ps signal.

with a smaller pulse width, corresponding to a spectrum of higher frequency. The output is shown in Fig. 3.6(d). This figure shows that the proposed antenna has a higher gain, even at this higher frequency. However, significant pulse distortion and ringing has occurred. We can conclude that proposed antenna is performing well at the lower frequencies that it has been designed for, at the expense of worse performance at higher frequencies.

3.3.3 Antenna Field Patterns

The simulated and measured field patterns of the proposed antenna are shown in Fig. 3.7 and Fig. 3.8. The field patterns follow most of the behaviours expected from AVA Vivaldi antennas. This includes relatively high cross polarization when compared other wideband antennas, as well as predominately isotropic radiation at the low frequency cutoff, which becomes more directive as the frequency increases. The simulated and measured results show good matching, however, there appears to be a offset in the azimuthal plane of the measurement results. Because we expect symmetric behavior we can conclude that this is very likely due to measurement error.

3.3.4 Antenna Details

The antenna design is based on other works of AVA Vivaldi miniaturization [81]. The design starts with the leaves, after which the slots are added. Small circular perforations are added to slots' ends to increase the apparent length of the leaves further. The thickness of the slots, the slope of the leaves, and other constants are found by a parametric search in simulation. The antenna is described in Fig. 3.9. The details of the constants are detailed in Table. 3.1.

$$C_A = \alpha e^{a_1(u_x+25)} v_x + 4e^{a_3(t-u_x-w_x)} \tag{3.1a}$$

$$C_B = \alpha e^{a_2(t-top)} - \alpha + \beta * 0.5 \tag{3.1b}$$

$$C_C = \alpha e^{a_1(t-top)} - \alpha + \beta * 0.5 \tag{3.1c}$$

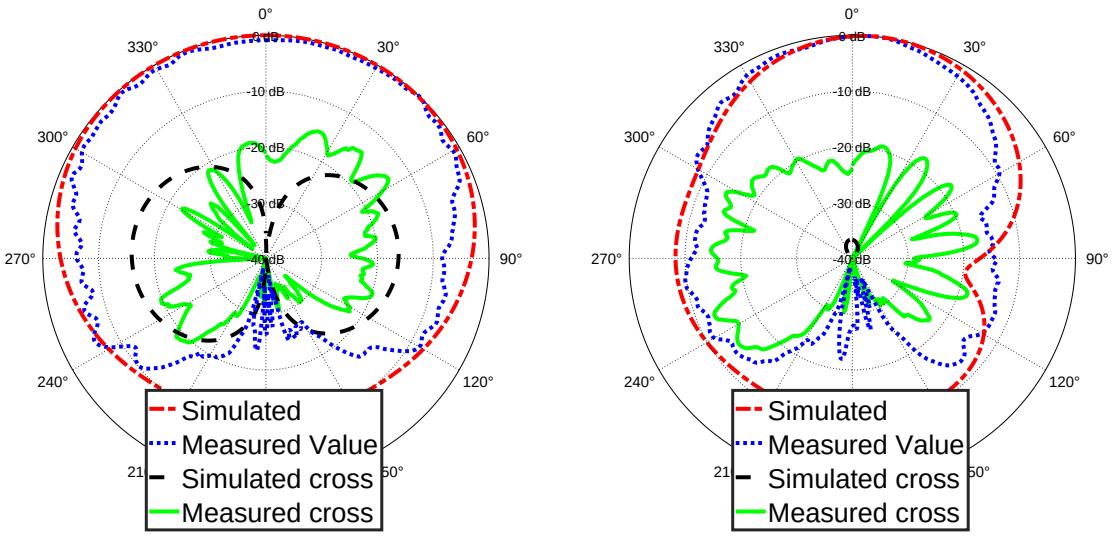

(a)

(b)

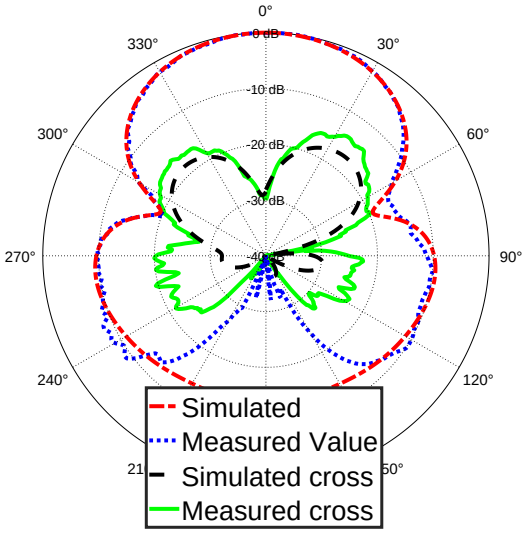

(c)

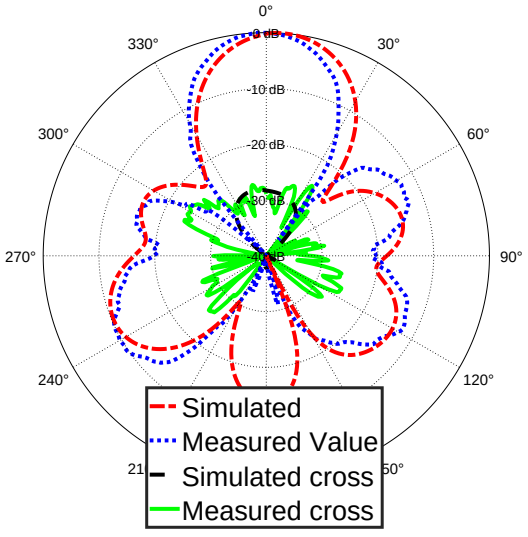

(d)

Figure 3.7: Antenna simulated and measured field patterns. (a) Normalized field in the E-plane at 2 GHz. (b) Normalized field in the H-plane at 2 GHz. (c) Normalized field in the E-plane at 4 GHz. (d) Normalized field in the H-plane at 4 GHz.

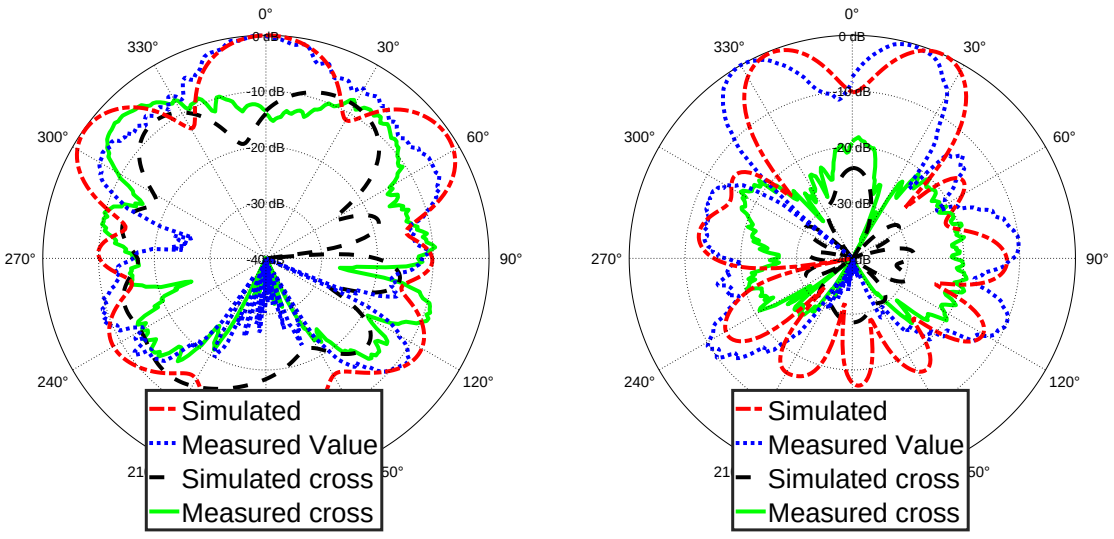

(a)

(b)

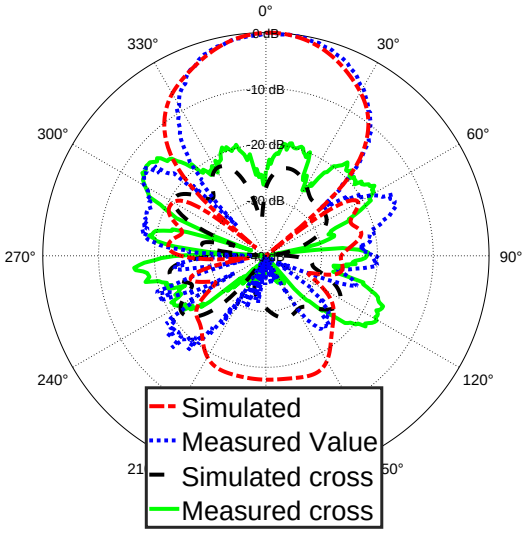

(c)

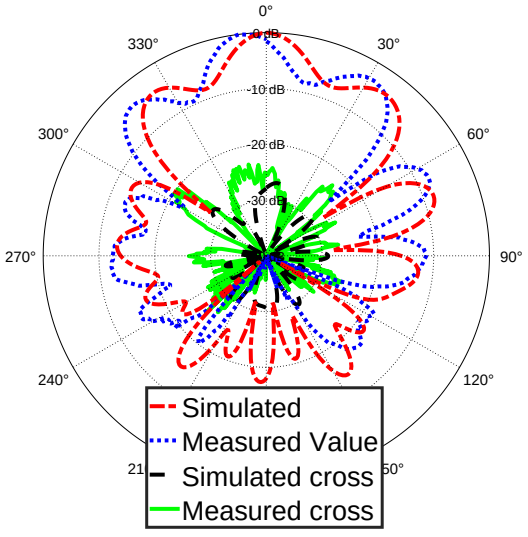

(d)

Figure 3.8: Antenna simulated and measured field patterns, (a) Normalized field in the E-plane at 7 GHz. (b) Normalized field in the H-plane at 7 GHz. (c) Normalized field in the E-plane at 10 GHz. (d) Normalized field in the H-plane at 10 GHz.

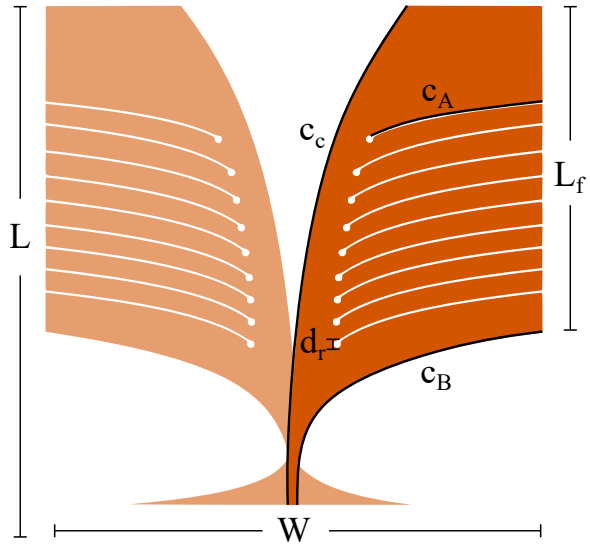

Figure 3.9: Details of antenna design.

Where the curve of the bottom of the slots is identical to C_A when $w_x = 0$. u_x and w_x are scaling variables that correspond to the number of the slot. The slot parameters are detailed in Table. 3.1

Parameter	value	Parameter	value	Parameter	value
u1	-5	v1	-0.5	L	6
u2	9	v2	v1-0.5	W	9
u3	12	v3	v1-0.75	Lf	12
u4	1.23	v4	v1-1	α	1.23
u5	1.5	v5	v1-1	β	1.5
u6	1.5	v6	v1-1	d_r	1.5
u7	0.035	v7	v1-1.25	a_1	0.035
u8	0.15	v8	v1-1.5	a_2	0.15
u9	0.15	v9	v1-1.5		

Table 3.1: Antenna dimensions

3.4 Time-Domain Characteristics

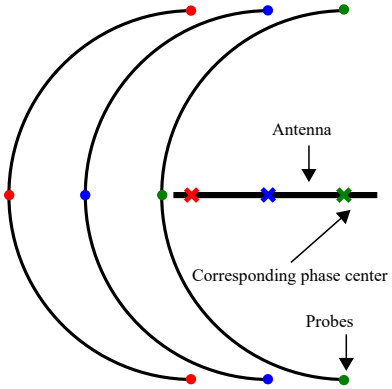

(a)

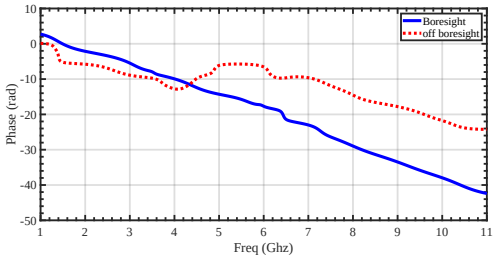

(b)

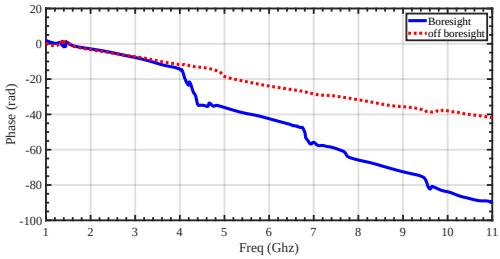

(c)

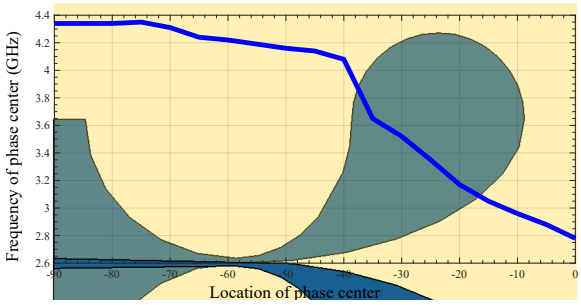

(d)

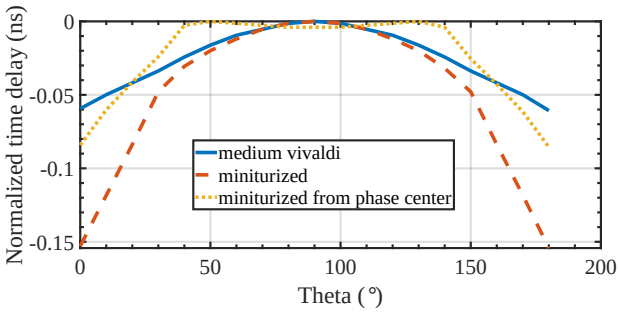

(e)

Figure 3.10: Analysis of phase centre, (a) Simulation setup. (b) Phase plot for the mid-sized Vivaldi at 2.5 cm from the antenna edge. (c) Phase plot for the miniaturized antenna at 3.5 cm from the antenna edge. (d) Plot of phase centre as a function of location in antenna. (e) Plot of group delay as a function of angle.

3.4.1 Phase Centre

Antenna phase centre is a convention that is primarily used in the field of GPS antennas [82]. The phase centre is a location on or near the antenna from which the fields, are approximately in phase, when equidistant from the phase centre [83]. The phase centre was developed and is used most commonly to calibrate GPS antennas [82]. The phase centre is not guaranteed to exist and is usually concerned with phase fronts of the main beam. We did not find anyone exploring the use of phase centre in wideband antennas in the literature. Here we propose phase centre as a way to explain antenna behaviour. To analyse the phase centre of the antennas, we set up a simulation framework as follows; The antenna edge is at the origin (0,0,0), facing the positive z-direction. Probes are placed in the boresight direction starting at 15 cm from the antenna, at 5 mm intervals with a total of 20 probes. The location of the probes are therefore from (0,0,15) to (0,0,5.5) cm. Another linear array of 20 probes is placed at locations (15,0,0) to (15,0,-9.5). Thus using the two probes located at (0,0,15) and (15,0,0) we can analyse the phase centre at the antenna edge. If we use other sets of probes we can view possible phase centres at different locations, farther into the antenna. The simulation setup is shown in Fig. 3.10(a).

For the mid-sized Vivaldi, the phase from the bore-sight and off-boresight probes can be compared. One such example is shown in Fig. 3.10(b). This corresponds to an analysis of the phase at 2.5 cm from the antenna edge. The graph demonstrates that this location is a potential candidate for the phase centre at 4.3 GHz. Other locations correspond to different frequencies. From this, we conclude that the phase centre from 2.7-4.3 GHz can be found and are arranged from the antenna edge to a location 8.5 cm from the front antenna edge. This distribution is shown in Fig. 3.10(d).

In contrast to the mid-sized Vivaldi, the miniaturized antenna has different behaviour. The phase of the miniaturized Vivaldi 3.5 cm from the antenna edge is shown in Fig. 3.10(c). This figure shows that this location is a good candidate for the phase centre for a large spectrum of frequencies. These frequencies also correspond to the spectrum of the antenna

as shown in Fig. 3.2 and are also the frequencies of interest that the antenna was designed for as shown in Fig. 3.1(b). This indicates that the frequencies of the pulse originate from the exact same location. This explains how this antenna shows improved pulse shapes for certain frequencies and not for others.

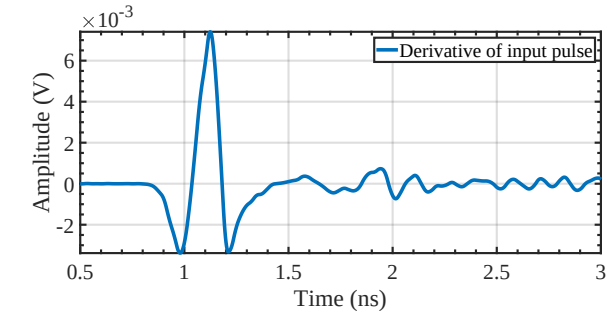

(a)

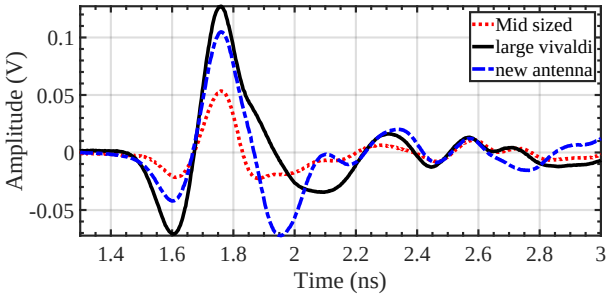

(b)

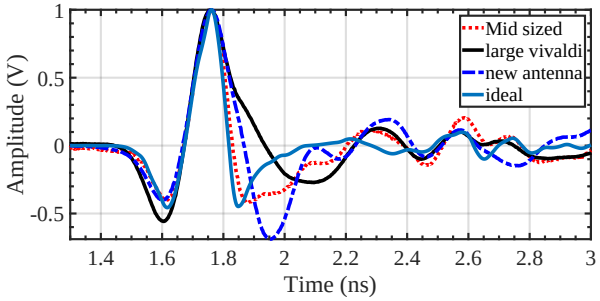

(c)

Figure 3.11: Comparison of antennas time-domain performance. (a) First derivative of the input pulse. (b) Received pulse between two antennas placed 30 cm apart. (c) Scaled results, and comparison with the first derivative of the input pulse.

The corresponding time-domain analysis is shown in Fig. 3.10(e). This is a plot of when the peak of the pulse is arriving at locations 15 cm from the edge of the antenna as a function

of angle. For ideal behaviour, this should be a flat line as it would be arriving at all radial locations simultaneously. As we can see from the graph, the Vivaldi antenna has slightly flatter profile than the miniaturized antenna. However, let's take the information we have just gained from the phase centre analysis. We can measure the propagation of peaks, from the true phase centre of the antenna, not simply with respect to the edge of the antenna. This is shown to have slight variation as a function of frequency for a large beamwidth which includes the entire main beam.

Radiation Analysis

For a Vivaldi antenna, the ideal behaviour radiation in the transmit mode is differentiation the pulse [17]. The measured output pulses of the three antennas used in the comparisons are shown in Fig. 3.11(a). These waveforms are measured using two of the same antenna aligned in the bore-sight plane, in the far field from one another. For these traveling wave antennas the expected result is a differentiation in the time domain [17], [20] . A comparison with the idealized result and the results from the three antennas is shown in Fig. 3.11(c). This is an unexpected result as the mid-sized Vivaldi has a spectrum that is not properly matched to the input pulse. Thus we would expect it to have the worst behaviour when compared to the ideal output. The large Vivaldi is the best at coping with the low frequencies, so it is surprising that it has such a poor fit with the ideal result. In this respect, the mid-sized Vivaldi performs the best, with behaviour closely mimicking the first derivative of the input pulse. However, ideal behaviour is not exactly related to performance. When creating certain types of images such as positive and negative [4], having an ideal second derivative pulse can mean good quality reconstructed images, in other cases, it is not beneficial.

3.4.2 Near-Field Superluminal Speeds

For antennas operating in the near-field, the near-field radiation characteristics is im-

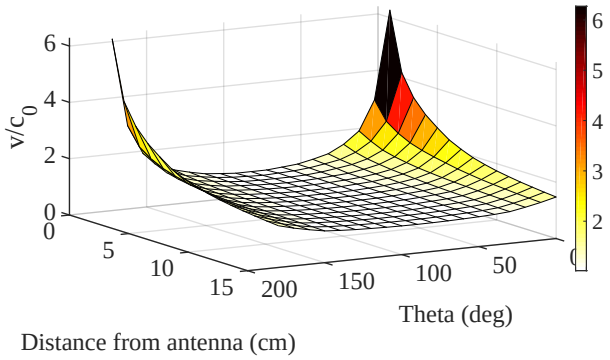

(a)

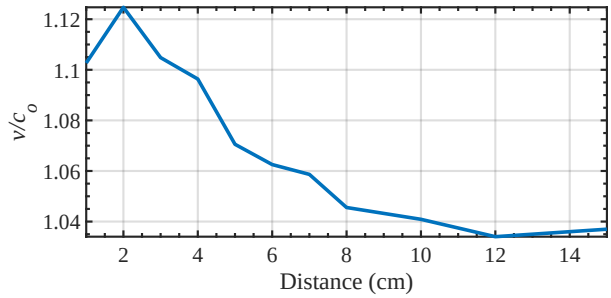

(b)

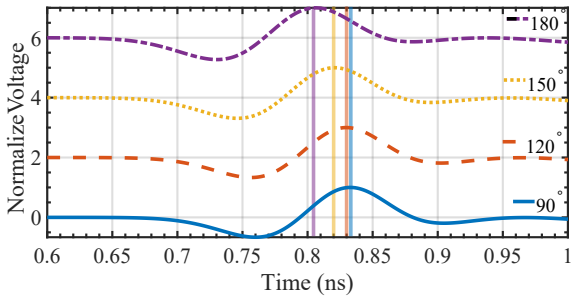

(c)

Figure 3.12: (a) Group pulse-peak velocity of apparent transmitted velocity derived from simulation. (b) Measured speeds along the bore-sight direction. (c) Different way to visualize the speeds by showing the peaks at different angles 1 cm from the antenna end-fire.

portant. Recently, a method to characterize the near-field of a transmitter and the entire transceiver was proposed [60]. It measures a point spread function of the time the pulse travels to different locations in the field of view. Here we make use of this technique to analyse the behaviour of the proposed miniaturized antenna. The results are presented in Fig. 3.12. The antenna is simulated and voltage probes are used to measure the time taken to travel to locations in the field of view. The time taken for the peak of the pulse to travel to those locations with respect to the time the pulse was at the edge of the antenna is used along with the distance to measure the apparent speed that the pulse peak took to each point in the field of view. Due to pulse reshaping, the pulse peak can appear to travel faster than c_0 [60]. These values depend on (r, θ). As r goes to the far-field the speeds approach c_0; Additionally, due to fields detaching from the antenna before the end of the antenna, the pulse appears to travel to oblique angles with high speeds. Fig. 3.12(a) can be represented in a different manner to show the waveforms as a function of time at various angles as shown in Fig. 3.12(c). Here it is clear that the pulse is arriving at locations equidistant from the end of the antenna at different times, equating to different speeds. The measured values for the bore-sight speeds of the proposed antenna are shown in Fig. 3.12(b). Crucially, this antenna has reduced pulse reshaping in the near-field, with an apparent pulse velocity not exceeding $1.12 \times c_0$. As the mid-sized Vivaldi has a more present near-field [60], it will cause more errors if it is neglected.

3.4.3 Imaging Analysis and Comparison

Here we will further investigate [84] and compare time-domain and frequency domain imaging. Time-domain imaging is conducted with either one or two antennas. It involves a Gaussian pulse generator, a pulse-shaping network, and a differentiator block prior to the transmitting antenna [74]. The receiving hardware consists of a time-sampling oscilloscope in the laboratory; or a time expansion architecture and off-the-shelf analog to digital and processing hardware in real-world applications [14]. The frequency-domain setup consists of a vector network analyser and connected antennas. There are different algorithms to recon-

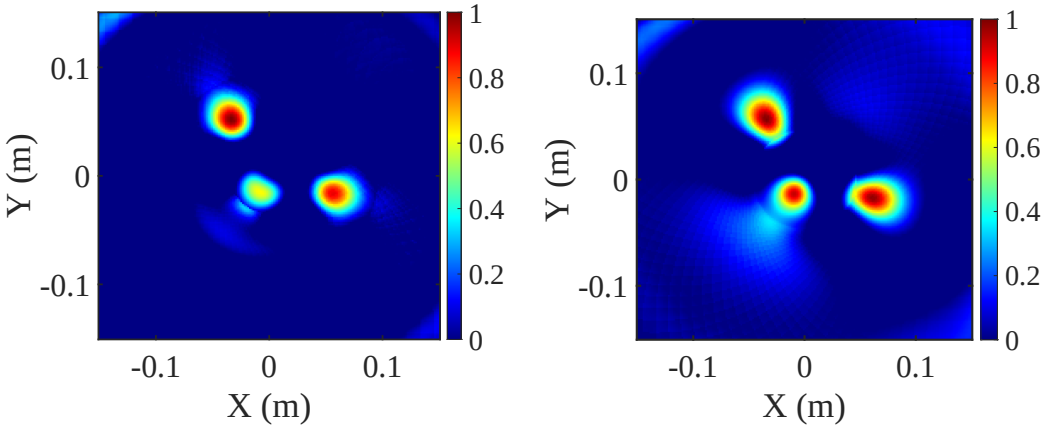

Figure 3.13: Time-domain reconstructed image for the, (a) mid sized Vivaldi and, (b) for the proposed antenna.

struct images, such as the back-projection algorithm or Kirchhoff migration algorithms [85]. Here we will collect data using the same targets and an identical environment. The data are collected in the respective domains, and the frequency data is converted to the time domain; after that, identical reconstruction processes are followed.

The experiment consists of three metal rods placed on a rotating table. The table is then rotated to create circular synthetic aperture imaging for the antennas, which are placed at the edge of the table.

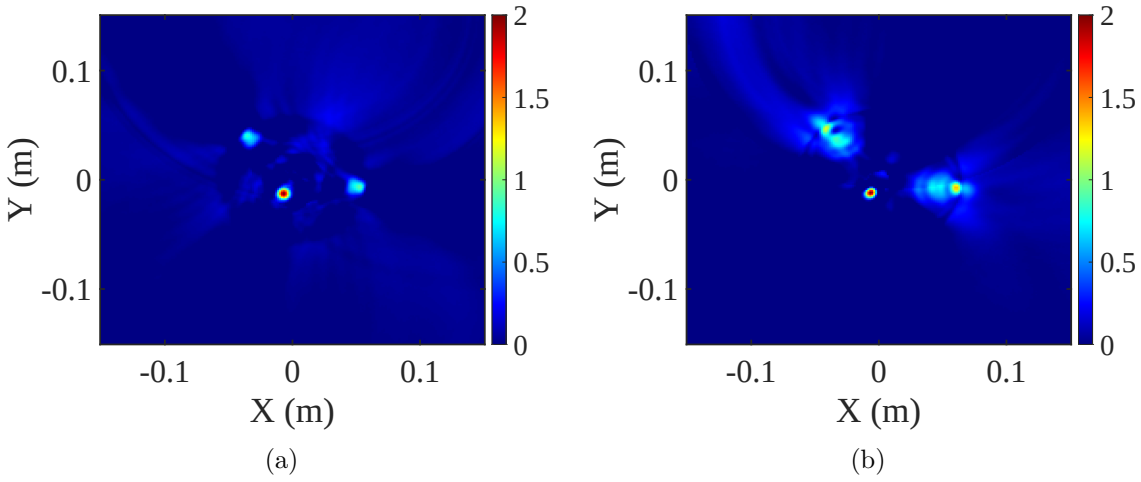

Figure 3.14: Reconstructed positive images using (a) mid sized Vivaldi, (b) proposed antenna.

3.4.4 Comparing Imaging in Different Domains

For the time-domain imaging, the reconstructed images are shown in Fig. 3.13. The positive images for the mid-sized Vivaldi and the miniaturized Vivaldi are shown in Fig. 3.13(a) and Fig. 3.13(b) respectively.

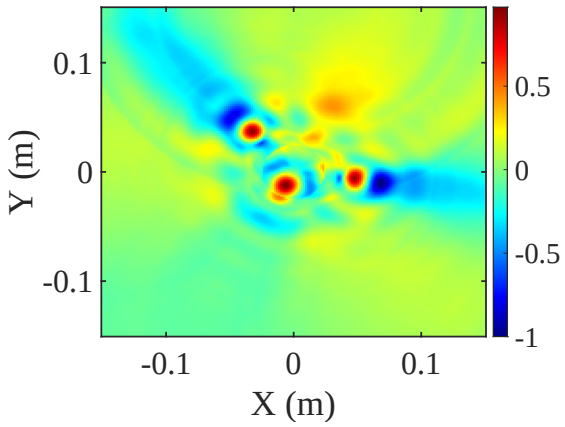

Figure 3.15: Frequency domain images reconstructed after restricting the frequency spectrum to up to 6 GHz.

Overall, the higher gain of the miniaturized antenna leads to the farther target being more equally illuminated to the other two. Apart from that small difference, this simple situation does not illuminate significant differences between the antennas.

The same experiment is conducted in the frequency domain. The reconstructed images are shown in Fig. 3.14. The positive images are shown in Fig. 3.14(a) and Fig. 3.14(b) for the mid-sized Vivaldi and miniaturized Vivaldi respectively. As the frequency domain has a higher maximum frequency, 20 GHz vs 6 GHz, the resolution is higher. We can show a different comparison by zero-padding the frequency values over 6GHz, the reconstructed image for that result is shown in Fig. 3.15. This shows a similar resolution when compared to the time-domain results as they now have similar maximum frequency, and therefore, similar resolution. However, due to the lack of ambient subtraction, and artefacts introduced in the fast Fourier transform, there is higher background noise in the frequency domain image. Here we can also see that the high-frequency behaviour of the miniaturized Vivaldi is worse than the mid-sized Vivaldi, this is because frequencies much above the spectrum that the

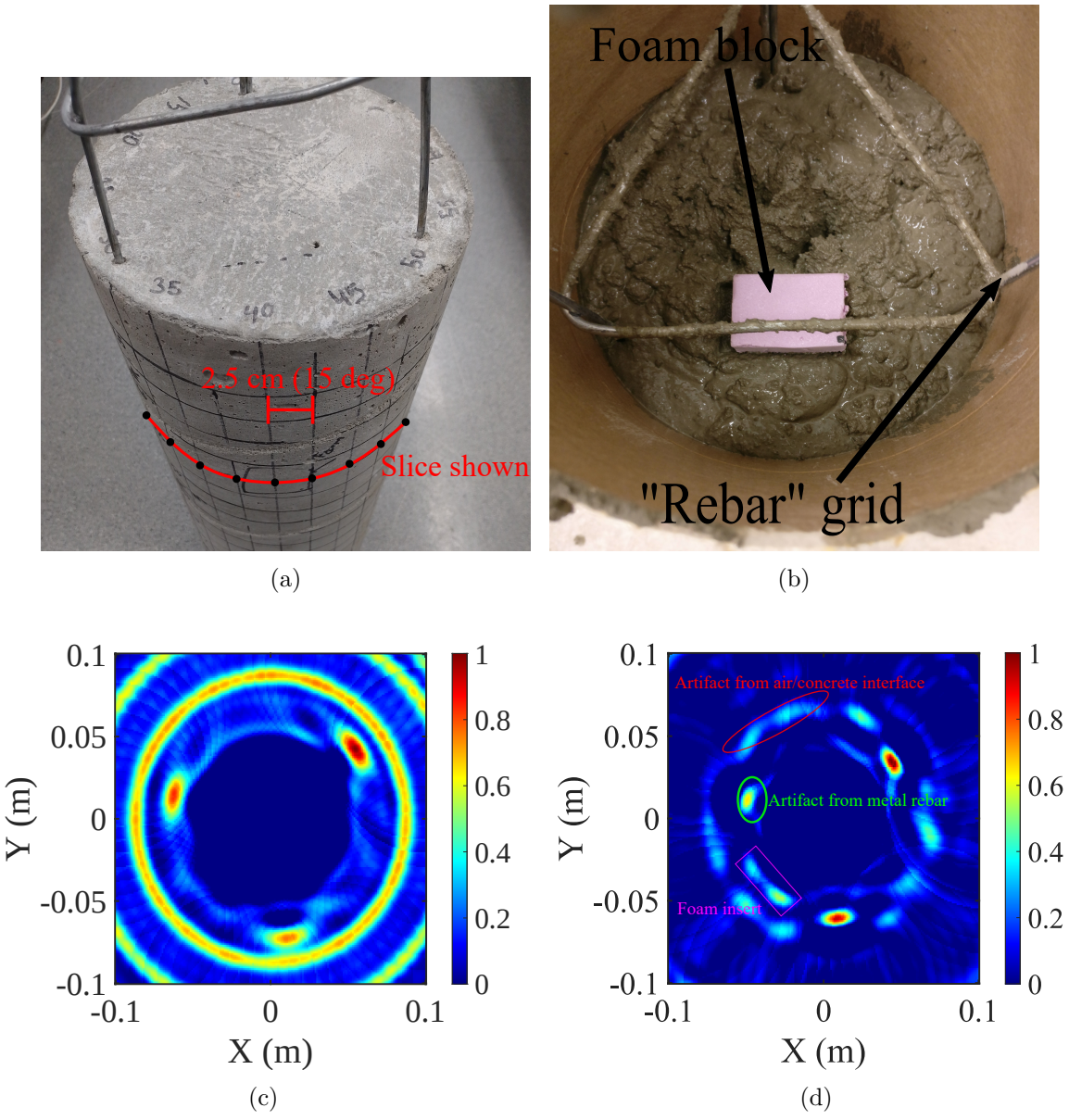

Figure 3.16: (a) Image of finished concrete pillar. (b) Image of concrete pillar under construction. (c) Positive reconstructed image. (d) Negative reconstructed image after average value is removed.

proposed antenna is customized for are included.

3.4.5 Practical Imaging Application

An antenna customized to a specific input pulse has been presented. Different aspects of the antenna and different metrics on which antennas should be judged have been proposed. In this section, the capabilities of this antenna are demonstrated in a situation where it is well suited to perform. The setup consists of a concrete pillar with a rebar skeleton. The pillar is 60 cm in circumference and consists of aged concrete ($>$ 3 years of drying). The rebar skeleton consists of a triangular grid with sides of 10 cm and a metal rod of a diameter of 5 mm as shown in Fig. 3.16(b). A foam block is added during the manufacturing process to simulate an imperfection in the concrete for imaging purposes. Measurements are taken at an axial slice, 2.5 cm apart (15 deg). This is done to achieve circular synthetic aperture (CSAR) imaging.

The positive reconstructed image from this experiment is shown in Fig. 3.16(c). The image clearly shows three strong reflections coming from the rebar grid as well as the outline of the pillar. From this image we can conclude that the rebar structure is not perfectly aligned with the pillar, causing one vertical rebar section on the bottom to be closer to the outside than the other two rebar, this is consistent with measurement of the visible portion where the distance from the metal to the edge of concrete for the three rebar is: 19.0 mm, 20.6 mm, 11.1 mm. To remove the concrete interface we can substract the average aperture value from each aperture location. To obtain the average value we sum along the aperture locations and then divide by the number of aperture locations. This is shown in the following equation:

$$C(i,:) = D(i,:) - \frac{1}{N}\sum_{i=1}^{N} D(i,:) \tag{3.2}$$

where N is the number of aperture locations, D is the measured data, and C is the calibrated data where the air/concrete interface has been removed. The negative reconstructed image using this data is shown in Fig. 3.16(d). Due to the average subtraction, the concrete

interface is mostly removed, the metal rods do not show up strongly in the negative image either [4]. Because the image features that were not previously visible have become more apparent, the foam block in the concrete is now visible and appears in the location that was expected.

This experiment is a demonstration of a difficult situation for microwave imaging. The air/concrete interface means less energy is able to penetrate into and return from the concrete. Additionally, to try to mitigate that, the antenna is placed directly on the concrete. This loads the antenna and can affect the antenna performance and return loss. Additionally, the concrete surface was cylindrical, increasing the difficulty to match as it was difficult to maintain the transceiver at the normal angle from the surface. Even with these issues, the antenna was able to image the internal structure of the pillar easily, and the salient details of the structure can be observed.

3.5 Chapter Summary

In this work, a miniaturized antenna is presented. It is then customized to match the spectrum of the input pulse. This miniaturized antenna is shown to have good characteristics in the conventional analysis, including gain, return loss, and fields. It also has good behaviour in the time-domain radiation. The antenna is then used to investigate the effect of antenna characteristics on imaging applications. Finally, the performance of the antenna was tested on a real-world application of imaging a concrete pillar with an internal metal structure. The antenna shows promising characteristics for applications for which it was designed.

Chapter 4

Virtually Developed Synthetic Aperture Radar: Theory, Simulation and Measurements

4.1 Introduction

UWB-SAR devices can be used as an effective imaging tool where high image resolution and relatively good probing depth are required. Generally, imaging using UWB-SAR involves three steps including raw data collection, calibration/preprocessing and refocusing/reconstruction. A complete set of optimally sampled raw data [86] is essential to obtain a high-quality image with comprehensive information. However, the optimal number of aperture samples is not practically obtainable in most circumstances. In military applications, radar may be called upon to perform other tasks during a SAR scan, introducing gaps in the data [87]. Cold heavy oil production with sand (CHOPS) [88] requires imaging to be done with a synthetic aperture significantly limited to the perforations in the metal casing. In biomedical imaging applications, acquiring a large number of aperture positions requires a long time, increasing the chance of body movement resulting in artefacts. Additionally, in the case of linear SAR [89], significant spatial aliasing effects occur at the aperture edges when the aperture is unable to be extended past the beamwidth of the target scene due to physical restrictions.

Different approaches have been investigated to repair or recover missing raw data in SAR applications. Certain approaches seek to provide spectral estimation for missing segments of the data based on missing data amplitude and phase estimation (MAPES) [90], the iterative adaptive algorithm (IAA) [87], the CLEAN algorithm [91]. In addition to the mentioned methods the sparse-driven technique can also be used to recover the missed data [92], [93]. Other approaches seek to provide estimation of missing aperture positions in a SAR data collection using linear predictive algorithms such as the BURG algorithm [94]. Others attempt to recover spectral segments and aperture positions simultaneously [95]. These approaches are restricted to the frequency domain and do not present a method of extrapolation to arbitrary aperture positions, limiting the applicability of these techniques. This work proposes a time-domain technique to produce synthetic data to correct aliasing at the edges of the aperture and inadequately sampled or missing data. The introduced technique is a general approach capable of dealing with data shortcomings created by non-ideal aperture sampling. This technique is developed fully in the time-domain, which prevents artefacts due to domain conversions.

To generate the missing part of data using extrapolation, first, the location of major scatterers, depending on the system sensitivity, is found. Based on the locations of the scatterers an approximation of data obtained at any arbitrary location can be generated. The final data set is the combination of the original measured data, and the synthesized virtual data, which can be processed using the Global Back-Projection algorithm [96] to reconstruct the image. This method is especially helpful in cases where the aperture is physically restricted, to generate lost data, or to decrease data collection time by decreasing measurement points, in biomedical applications, for example, where data collection time is a very important constraint.

4.1.1 Virtual Aperture Method

This section demonstrates a step-by-step procedure of how the major scatterers are lo-

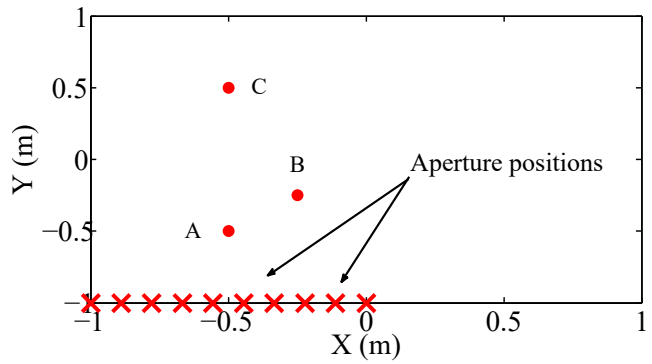

(a)

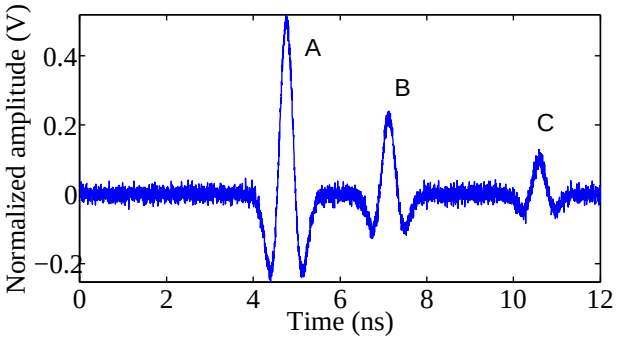

(b)

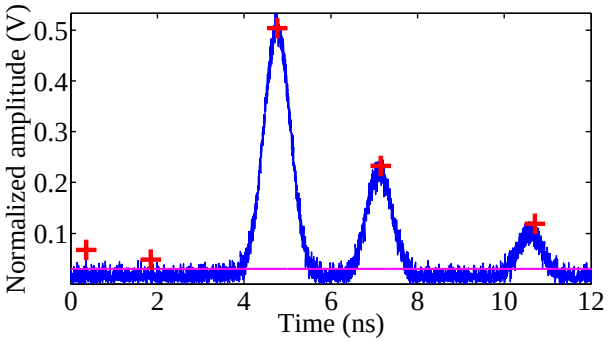

(c)

Figure 4.1: (a) Initial setup with the three point-targets and the measured aperture locations shown with red crosses. (b) Measured data from the first aperture location, (-1,-1). (c) Envelope data with threshold and peak detection applied.

cated and how their positions are used to generate the virtual data. The data are generated using a second derivative Gaussian pulse as described in (4.1), [97]

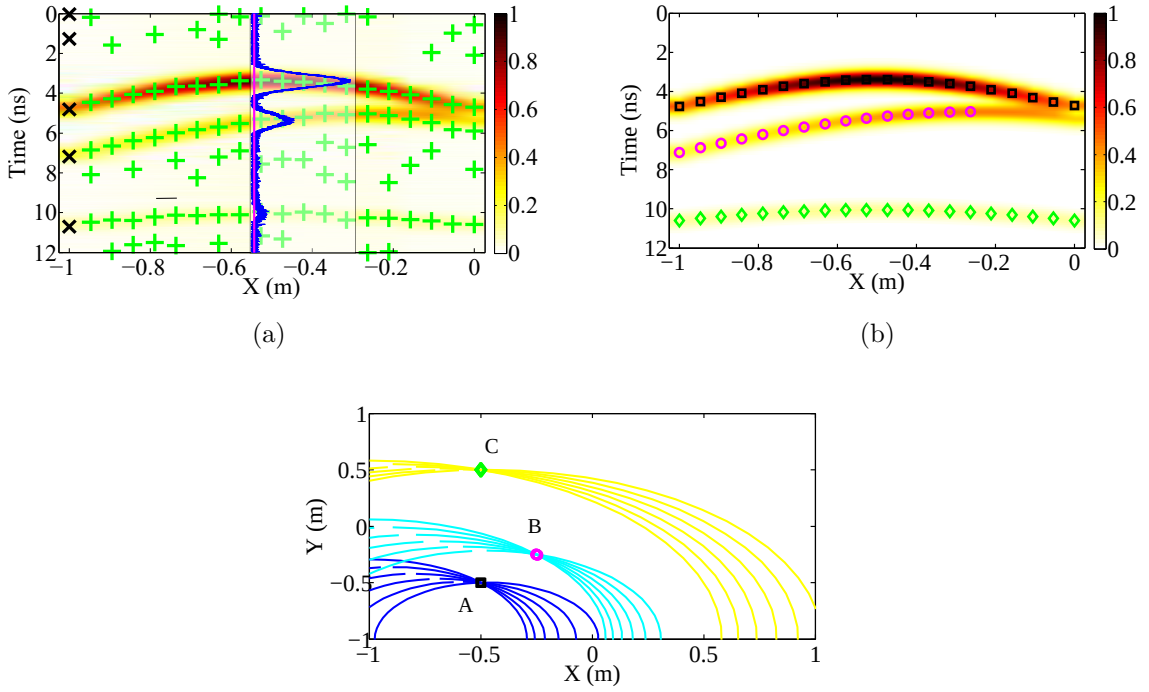

Figure 4.2: (a) Raw data from aperture positions with peak detections and data from Fig. 4.1(c) superimposed. (b) Raw data from aperture positions overlaid with peaks attributed to different objects. (c) Projection into the spatial domain of the detected objects, using the intersection of circles to localise the objects.

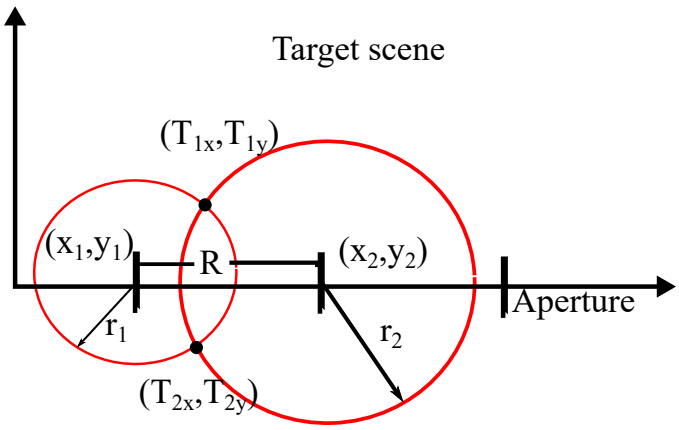

Figure 4.3: Circle intersection diagram.

$$P(t) = (\frac{2}{\tau^2})e^{(\frac{t}{\tau})^2}(\frac{2t^2}{\tau^2} - 1) \tag{4.1}$$

where $P(t)$ is the second derivative Gaussian pulse, t and τ are the time and time constant

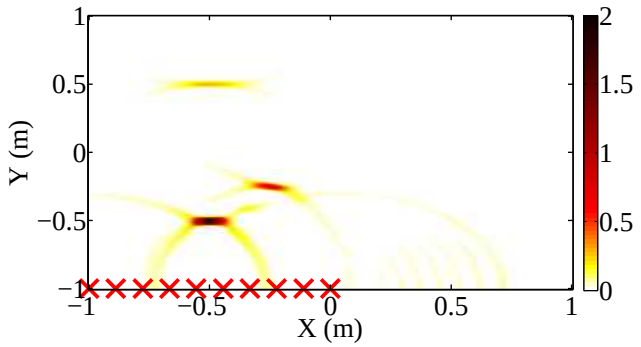

(a)

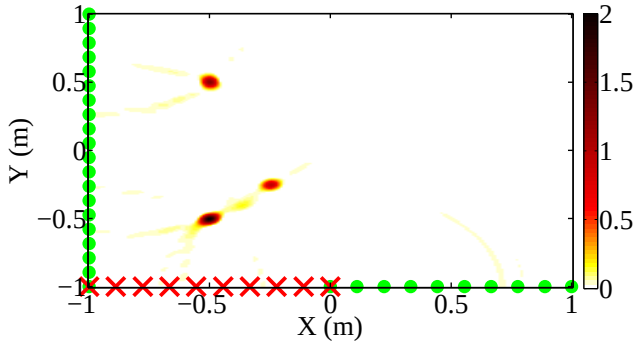

(b)

Figure 4.4: Reconstructed images using, (a) original data, (b) Combined original and virtual data.

respectively.

White Gaussian noise of -10 dB power is added to emulate a practical situation. The simulation is conducted in air with three ideal point targets (A, B, C). The data are collected from the shown aperture positions in Fig. 4.1(a). The transmitted signal is a second derivative Gaussian pulse with a full width at half maximum (FWHM) of 282 ps which corresponds to a -10 dB bandwidth of 2 GHz. The received raw data for transceiver location (-1,-1) are shown in Fig. 4.1(b). The three reflections from the three point targets are clearly visible. Fig. 4.1(c) shows the envelope of the received pulse used to locate the targets. The envelope is detected using the Hilbert transform [98]. In UWB applications a threshold of -30 dB covers most of the significant targets; therefore in this simulation we considered -30 dB as the threshold line, which is shown as a red line in Fig. 4.1(c). The minimum distance

between two targets that can be resolved is limited by the transmitted pulse width; therefore if the signal peaks are detected within the pulse width, they are considered to be a single target. The detected peaks over the threshold line are shown in Fig. 4.1(c). Five peaks have been located despite there being only three targets. These additional peaks have occurred due to the added noise. Data from all aperture positions is collected and shown together in Fig. 4.2(a). The peaks from Fig. 4.1(c) are shown in black along with the other aperture positions, which are shown in green. The data from one of the central aperture positions are also superimposed to illustrate the transition from viewing the data at a single aperture position to viewing all the positions together.

As we know the data from true targets should fall on a hyperbolic path, hence the other targets are considered to be noise effects. All the peaks are grouped together into objects, as shown in Fig. 4.2(b). Objects with less than a certain number of peaks are then discarded, since only the large scatterers are desired and in an attempt to reduce the noise. In this idealized scenario, the hyperbolic curves are detected at a high proportion of the receivers. In practical situations, however, this portion would be much smaller and would depend on the specific setup. Objects with a few peaks may correspond to small scatterers but they may equally be caused by interference, multiple reflections, or purely noise. The probability of missed detection or false alarms can be reduced by appropriately selecting the signal threshold.

After the targets have been identified in the raw data they are then projected into the spatial domain based on the time of flight, which is shown in Fig. 4.2(c). Each measurement represents a circle in space of radius r,

$$r = \frac{1}{2}(t - t_{dl})v_g \tag{4.2}$$

where t is the time of flight of the target, t_{dl} is the calibration time delay that includes, the delay due to the measurement system, cables, and the group delay of the antennas, v_g is the group velocity in the medium. The calibration time delay can be measured by placing a target just in front (d=0) of the radar transceiver.

For the first measurement let the circle have radius r_1 and be centred at the transceiver location (x_1, y_1). The intersection of the circles of adjacent aperture positions is then found. The intersection of two circles indicate two possible locations of each target, one will be inside the target scene and the other will occur outside. The location occurring inside the target scene is taken to be the target. The cumulative intersections from the entire aperture will determine the actual targets and eliminate false targets. The circle intersection locations are calculated using (4.3)-(4.9).

An example is shown in Fig. 4.3: two circles of radius r_1, r_2 centred at (x_1, y_1) and (x_2, y_2) the distance R between circles is determined by,

$$R = \sqrt{(x_1 - x_2)^2 + (y_1 - y_2)^2} \tag{4.3}$$

if $R > (r_1 + r_2)$ or $|r_1 - r_2| > R$ the circles will not cross. Otherwise the intersection points will be determined by the following equations:

$$(T_{x1}) = \frac{1}{2}(x_1 + x_2) + B((x_2 - x_1)) + C((y_2 - y_1)) \tag{4.4}$$

$$(T_{x2}) = \frac{1}{2}(x_1 + x_2) + B((x_2 - x_1)) - C((y_2 - y_1)) \tag{4.5}$$

$$(T_{y1}) = \frac{1}{2}(y_1 + y_2) + B((y_2 - y_1)) + C((x_2 - x_1)) \tag{4.6}$$

$$(T_{y2}) = \frac{1}{2}(y_1 + y_2) + B((y_2 - y_1)) - C((x_2 - x_1)) \tag{4.7}$$

where,

$$B = \frac{r_1^2 - r_2^2}{2R^2} \tag{4.8}$$

and

$$C = \frac{1}{2}\sqrt{2\frac{r_1^2 + r_2^2}{R^2} - \frac{(r_1^2 - r_2^2)^2}{R^4} - 1} \tag{4.9}$$

A new virtual aperture is now chosen by the user to best correct the data for the given setup. After the targets are localized, the virtual data may be generated for the desired radar locations. The time delay between the i^{th} localized target and the n^{th} new virtual aperture location is known from,

$$t_{in} = \frac{dist_{in}}{v_g} + t_{dl} \tag{4.10}$$

where t_{in} is the time delay between the i^{th} target and new transceiver location n given by (X_n, Y_n), $dist_{in}$ is the distance between the target and transceiver locations, and v_g and t_{dl} are the group velocity and measurement delay respectively.

For each aperture position the total response is the summation of the individual target responses. The response for the n^{th} aperture position and M located targets is generated using,

$$V_n = \sum_{i=1}^{M} \frac{1}{4\pi dist_{in}^2} P(t - t_{in}) \tag{4.11}$$

where V_n is the generated data for the n^{th} new aperture position, $dist_{in}$ is the distance from target i to new aperture position n, and $P(t - t_{in})$ is the pulse delayed by t_{in}. The $\frac{1}{4\pi dist_{in}^2}$ is the energy normalization factor, which accounts for the power lost over distance.

For the current example, c.f. Fig. 4.1(a), the reconstructed image using the Global Back-Projection algorithm is shown in Fig. 4.4(a). The aperture is shown as red crosses. Fig 4.4(b) shows the reconstructed image using the original and virtual data, the virtual aperture is shown as green circles. When comparing Figures 4.4(a), and 4.4(b), the image quality is enhanced significantly. In the reconstruction using the original aperture, the targets are stretched in the x-direction and the third target appears very faint. These problems have been alleviated after incorporating the virtual data.

4.1.2 Algorithm Development

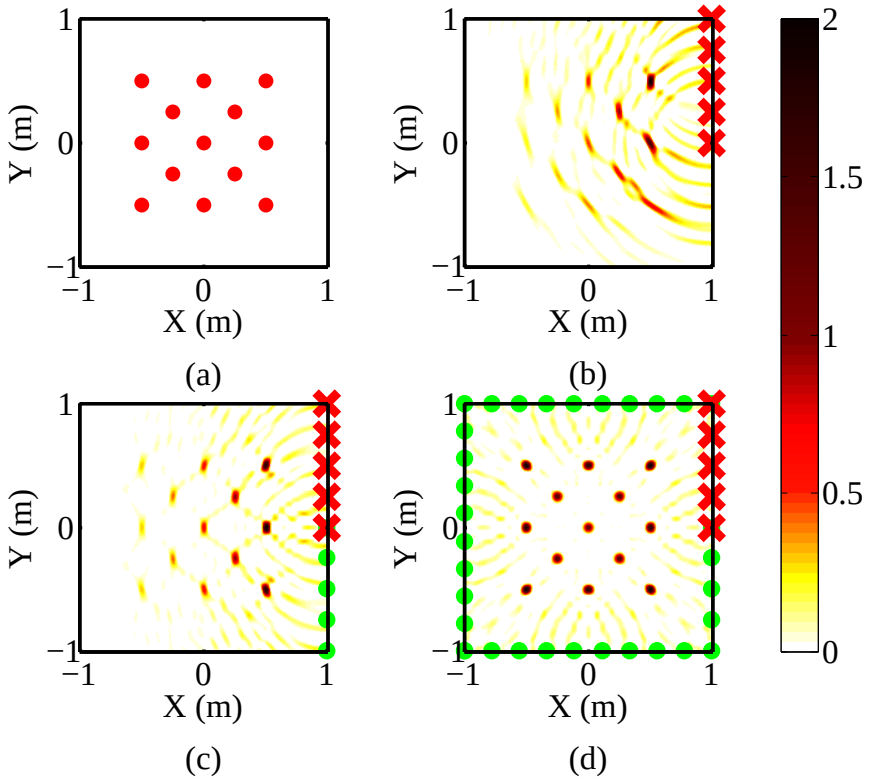

Figure 4.5: Point target simulation, (a) Point target positions. Reconstructed image, (b) Using original aperture, (c) Using aperture extended in y-axis, (d) Using aperture extended along entire perimeter.

The algorithm is implemented in MATLAB as follows: the data are initially collected as explained in Section 4.1.1; the data are smoothed using a moving average filter with the span set to 0.5% of the data points [99]; a matched filter [100] is applied to the data to make the reflections more evident. The envelope of the data is found using the Hilbert transform [98] as shown in 4.1(c).

The local maxima above the threshold are considered to be signal peaks. The peaks are then sorted in ascending order of time. The data now consists of a two column data set consisting of the time in one column and the corresponding aperture position in the second column. The peaks are now compared to determine if they belong to the same distributed scatterer. This is done by comparing the first row to a subset of rows that are one aperture

position on either side of the first peak:

$$|t_{N\pm1} - t_N| < \delta \tag{4.12}$$

where t_N, $t_{N\pm1}$ are the time of flights of the first peak and the peaks in adjacent aperture positions respectively, and δ is the allowed error. After the first peak has been added on either side of the first peak comparisons are made along the aperture, linear prediction is used to determine if peaks should be part of the same object.

$$|2t_b - t_a - t_c| < \delta \tag{4.13}$$

where t_b, t_c, and t_a are the time of flights of the: last peak to be added to the object, the peak in question, and the second to last peak added to the object respectively. δ is a measure of the allowed difference in the time of flights. As a first approximation

$$\delta = \frac{2\Delta Tx}{v_g} \tag{4.14}$$

where, ΔTx is the distance between aperture positions, and v_g is the group velocity in the medium. This number can be varied depending on noise and density of hyperbolic curves.

This process is continued in both directions along the aperture. If at any aperture position no peak that meets the desired criteria can be found, then the hyperbolic curve is terminated at that side of the aperture. When both sides are terminated, all the peaks that have been assigned to the current hyperbolic curve are removed, and the process is repeated for the remaining peaks.

After all the peaks have been attributed to objects, a decision is made to determine if the objects are significant enough to be considered. Whether an object is large enough to be considered depends on the amount and size of objects and noise in the target scene. Generally this number is from 10% to 20% of the aperture positions. If the object does not contain a large enough number of peaks it is discarded.

The objects are then transformed into the spatial domain. This is done in the following

way: for each object, the peaks are organized in ascending aperture position. The radius of each peak is then found using (4.10), solving for $dist_{in}$. The intersections of the circles are now found by comparing the circles from closest neighbouring aperture positions. The circle intersection ((4.3)-(4.9)) generates two solutions. One solution falls inside the target scene, and is considered the point target.

The virtual data can be generated at any aperture position- between the original aperture positions or anywhere in the target space, based on the virtual aperture and the target location, using (4.11). The pulse shape used in the manuscript is the second derivative Gaussian pulse as mentioned earlier. However, there is no restriction on the pulse shape. Once the virtual data is generated, both the virtual and original data are used to reconstruct the image using the Global Back Projection algorithm.

Concept Validation

The following example demonstrates the effect of virtual apertures on image quality for point targets. The target scene consists of 13 point targets placed as shown in Fig. 4.5a. The reconstructed image using only the original aperture positions is shown in Fig. 4.5b. From this image the targets that are close to the aperture appear strong, whereas those farther away appear faint. Using the proposed method, a virtual aperture is added to extend the aperture along the y-axis, as shown in Fig. 4.5c, where the quality of the image is enhanced to some extent. However, by extending the virtual aperture around the target scene, the image quality is significantly enhanced as all the targets are detected with the same quality (shown in Fig 4.5d).

4.2 Full-Wave Simulation

The proposed technique is validated through full-wave simulation for some practical applications. The input pulses used in Section 4.2.1 and Section 4.2.2 have -10 dB BW of 5

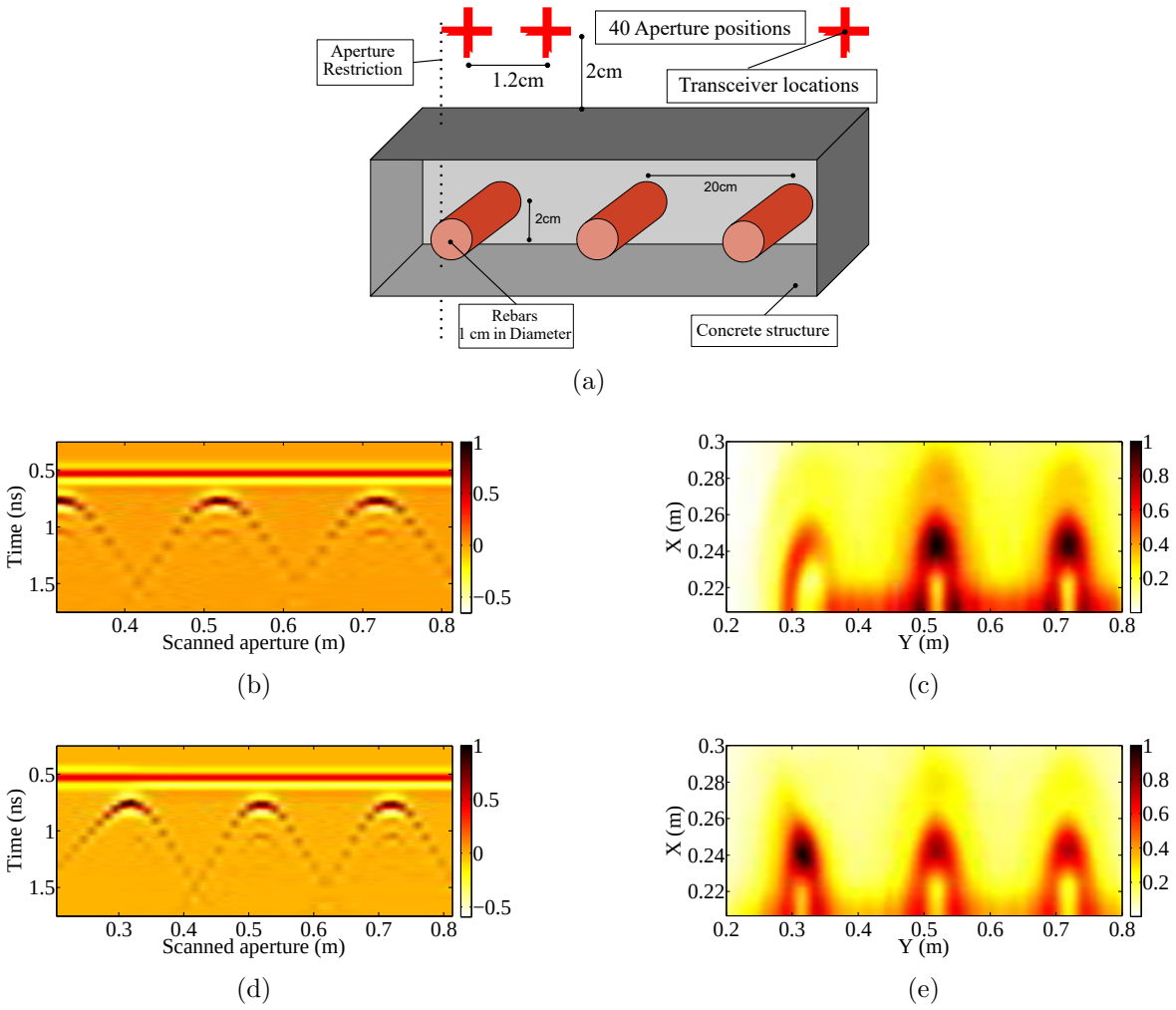

Figure 4.6: Concrete with rebar simulation results. (a) Simulation setup. (b) Restricted raw data. (c) Reconstructed image using restricted data. (d) Combined data. (e) Reconstructed image using combined data.

GHz and 10 Ghz respectively.

4.2.1 Concrete Wall Monitoring with Limited Access

Here we considered a physical restriction on aperture positions to model a practical scenario, for example imaging of a partially buried concrete pillar. Here the pillar is scanned to evaluate the configuration and the quality of the reinforced bars inside the concrete. The simulation set-up consists of 3 pieces of reinforcing bars (rebar) placed inside a concrete medium. Aperture positions are shown in Fig. 4.6(a). The concrete is modelled as a lossless

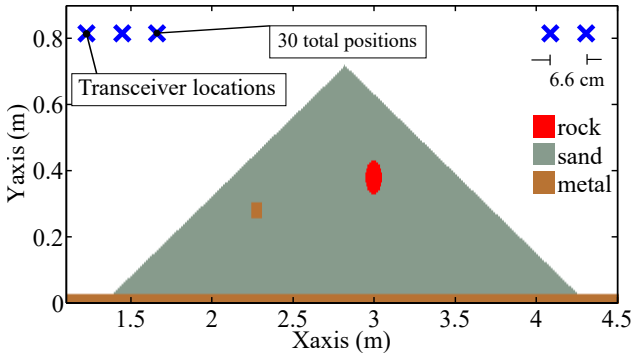

(a)

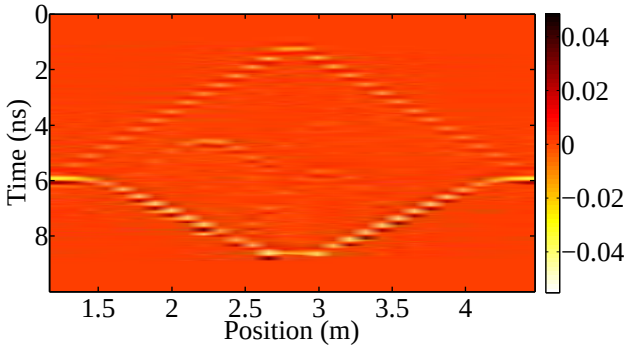

(b)

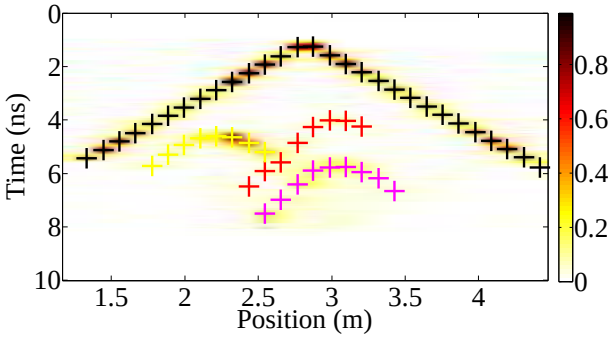

(c)

Figure 4.7: Oil sands simulation results. (a) Simulation set-up. (b) Raw data. (c) Envelope data with object detections superimposed.

material with $e_r = 4.0$. The conductivity of the metal is defined to be $\rho = 5e7$. The original data is collected and is shown in Fig. 4.6(b).

The reflection off the concrete and rebar is clearly evident. The reconstructed image using the original aperture is shown in Fig. 4.6(c), which shows the concrete boundary and

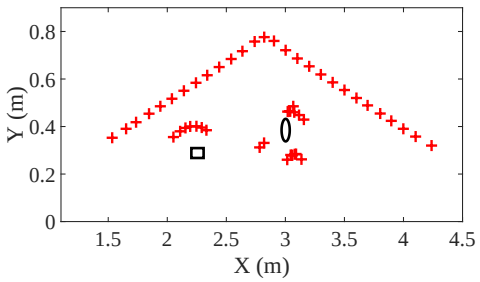

(a)

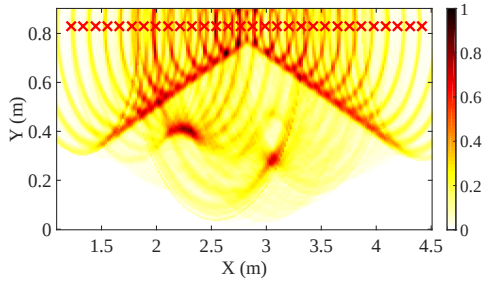

(b)

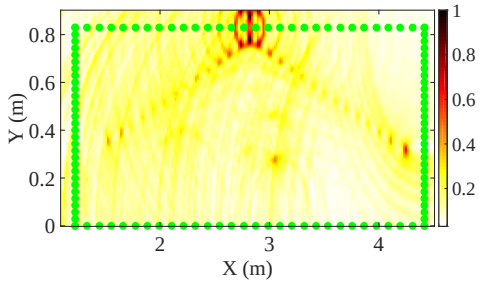

(c)

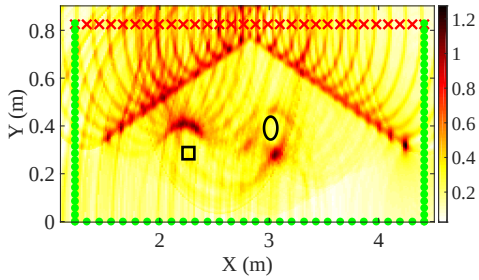

(d)

Figure 4.8: Oil sands simulation. (a) Point target positions. Reconstructed image using, (b) original aperture, (c) a virtual aperture, (d) combined original and virtual aperture.

the rebar. However, due to the aperture limitation the rebar at the left edge is deformed. Using the available information, one might conclude that this rebar has been corroded in

some way and requires maintenance. However, this is an incorrect assumption.

The proposed method can develop a virtual aperture. The aperture is extended to generate nine additional aperture positions. The combined virtual and original data is shown in Fig. 4.6(d). The reconstructed image using this data is shown in Fig. 4.6(e), which shows an improved image.

4.2.2 Oil Sands on Metal Belt

In oil sand mining operations, the ore travels on conveyor belts between processing stages. Tramp metal that has been broken off equipment and large rocks damages the processing equipment. Therefore, detecting the presence of these objects is very important. The simulation set-up shown in Fig. 4.7(a) is developed based on the oil sand operations in Alberta, Canada. The oil sands is modelled as a lossy medium $e_r = 2.7$, with $tan(\delta) = 0.0063$. The conveyor belt is modelled as a metal plane ($\rho = 5e7$). A metal piece of rectangular shape (4 cm x 6 cm) ($\rho = 5e7$) and a rock of 10 cm in diameter ($e_r = 5$) are placed in the oil sands.

The original data from this set-up is shown in Fig. 4.7(b). The reflections from the oil sand, the two buried objects and the metal belt are visible. Time-gating is used to remove the reflections from the metal belt. Due to the different group velocity in the oil sands an average group velocity is used to reconstruct the target scene [101]. The proposed method is then used to localize the targets, which is shown in Fig. 4.7(c). The spatially located targets are shown in Fig. 4.8(a). Because an average group velocity is used the objects do not appear exactly where expected.

The reconstructed image using the original data is shown in Fig. 4.8(b) where the rock is hard to see. A virtual aperture and the reconstructed image are shown in Fig. 4.8(c). The image is not as high quality as the image with the original data due to the approximations used to create the virtual data. The reconstructed image using both the original and virtual aperture is shown in Fig. 4.8(d). The original aperture is shown as red crosses while the virtual aperture is shown as green circles. Both the rock and the metal rectangles are more

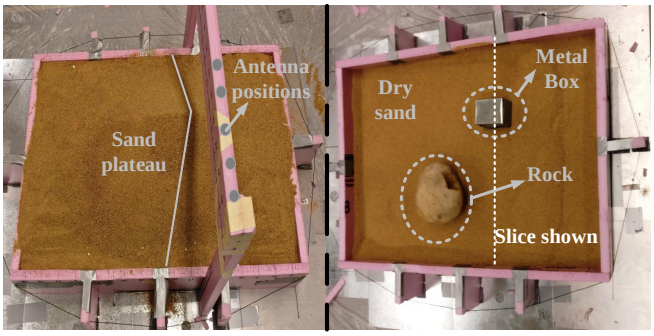

(a)

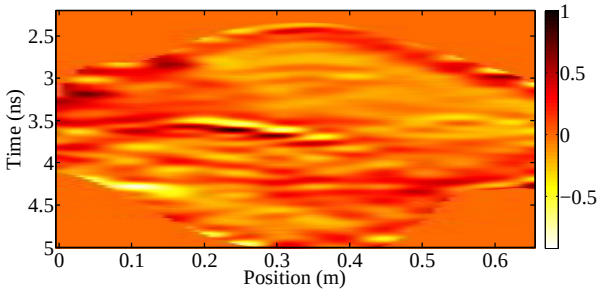

(b)

Figure 4.9: Oil sands experiment. (a) Experimental set-up. (b) Raw data.

visible than in the original image. As the specific group velocity was not considered here, the rock and metal appear lower in all the reconstructed images than in actuality.

4.3 Experimental Validation

The technique was further verified with two experiments. One experiment was designed to replicate the results from a full-wave simulation shown previously in Section 4.2, which is shown below in Section 4.3.1. The second experiment is shown in Section 4.3.2, detailing the proposed method with a significantly restricted aperture. The experimental set-up is detailed in the introduction and more formally here [97]. The pulse generator used was a AVTECH AVP -3SA-C, which generates pulses with 50ps rise time, with a variable amplitude up to $10V$ at a $1MHz$ pulse repetition frequency (PRF). The pulse has an peak power of 2W. The outputted pulse has a centre frequency of 6.5GHz and a -10dB bandwidth of 10GHz. The

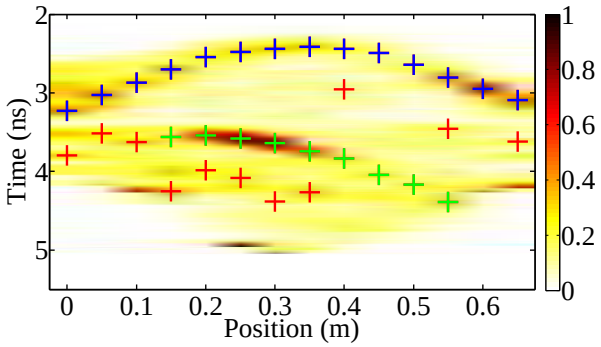

(a)

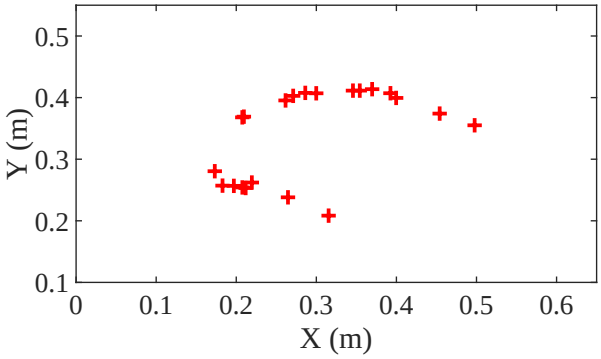

(b)

Figure 4.10: Oil sands experiment, (a) Objects superimposed over raw data. Oil sands shown in blue, metal in green, and peaks not associated with an object in red. (b) Target localization.

transmitted pulse has a -10 dB BW of 8 GHz, considering antenna operational bandwidth. The signal is digitized by a Keysight Infiniti Vision DSOX3024A Digital storage Oscilloscope. Mid sized Vivaldi antennas are used as the transmitting and receiving antennas. The data of the target scene is collected, along linear apertures for the examples in this chapter. Interpolation from 4500 points to 10000 as well as a low pass filter is used.

4.3.1 Oil Sands on Metal Belt

The experimental set-up is constructed by placing a metal sheet on the ground and then piling dry sand (in pyramidal shape) on top of it.A rectangular metal box (8.5 x 6.5 x 6.0 cm) and a rock (15 cm in diameter), $e_r = 3.34$ are buried in the sand [102]. The set-up is shown

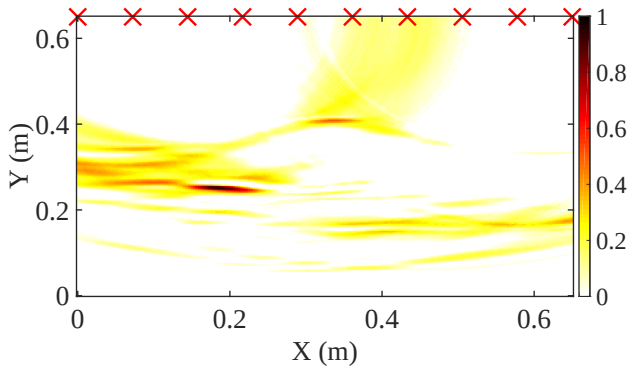

(a)

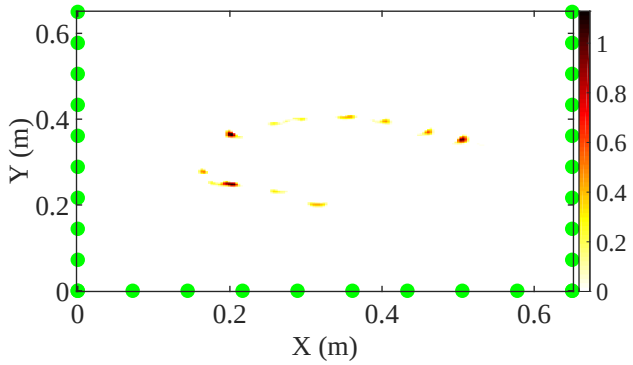

(b)

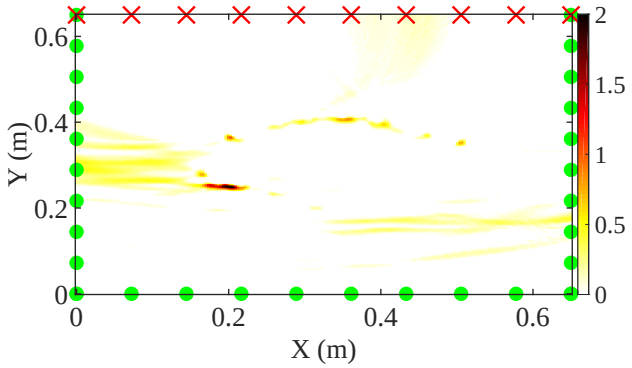

(c)

Figure 4.11: Oil sands experimental results. Reconstructed images using (a) raw data, (b) virtual data, (c) combination of virtual and original data.

in Fig. 4.9(a). Data is collected from a transceiver placed 65 cm above the metal plate and moved in increments of 5 cm from one side to the other. The data from a slice taken near the rock is shown in Fig. 4.9(b) this data has been time-gated to remove the reflections from the metal sheet and any noise occurring before the reflections off the sand. Using the proposed

method, the objects are found. The objects are shown as "plus" signs superimposed over the original data in Fig. 4.10(a). Here the blue and green peaks have been attributed to large objects (the sand and metal respectively) and the red ones have been discarded as noise. The targets spatial locations are then found and are shown in Fig. 4.10(b). The reconstructed image derived from the original data is shown in Fig. 4.11(a), where the image of the metal target is elongated. The aperture and the reconstructed image created from the virtual data is shown in Fig. 4.11(b). The reconstructed image using both the original and virtual data is shown in Fig. 4.11(c). The metal object in the combined image is much more visible than using the original data alone. Additionally, the object has become more defined and representative of the size and location of the metal box. Using a threshold of 0.5 times the maximum value of the image, the metal has 8.5 cm length in Fig. 4.11(a), in Fig. 4.11(c) this has been reduced to 5.8 cm; the actual length of the metal in the X axis is 6.0 cm.

During this analysis the group velocity was taken to be the average group velocity [101] of the target scene. The final images are not fully converged since an average group velocity is used for all different regions.

4.3.2 Limited Aperture

The proposed method is investigated in this example with a significantly restricted original aperture. The set-up consists of a metal plate with holes restricting the original synthetic aperture to three points as shown in Fig. 4.12(a).

The reconstructed image using the original data is shown in Fig. 4.12(b). The image is of poor quality and the rods are difficult to identify. Using the proposed method virtual data is generated to increase the quality of the reconstructed image. The reconstructed image using the combined data is shown in Fig. 4.12(c); the original aperture is shown as red crosses while the virtual aperture is shown as green circles. The rods are identifiable and very prominent in the reconstructed image using the combined datasets.

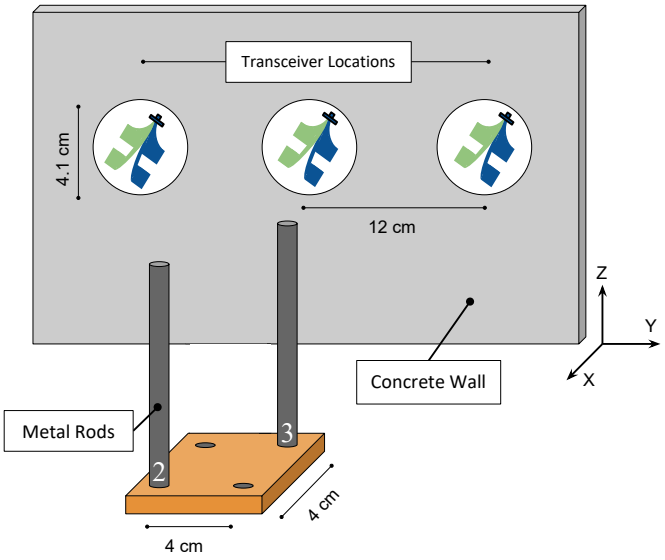

(a)

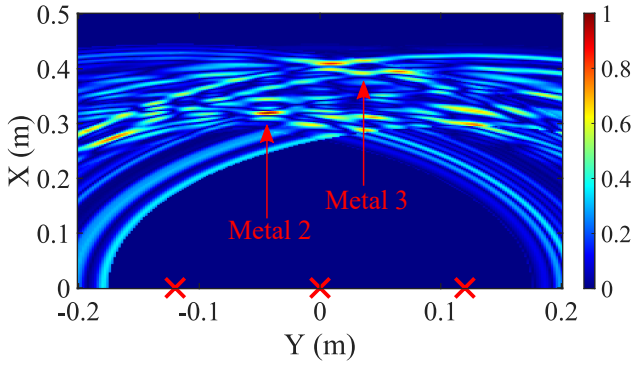

(b)

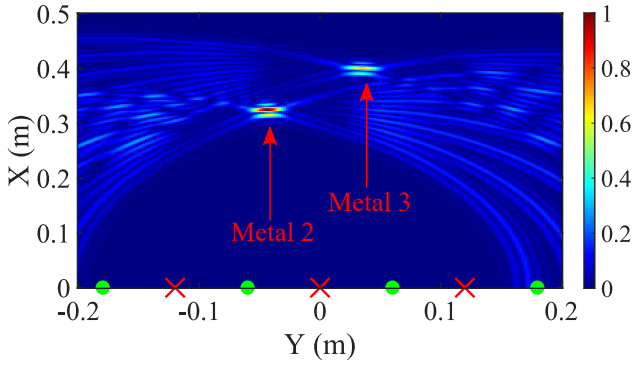

(c)

Figure 4.12: Limited aperture experiment. (a) Experimental set-up. Reconstructed images from, (b) original data, (c) combined original and virtual data.

4.4 Chapter Summary

In conclusion, this chapter first presents a new technique for detecting objects in SAR data. This knowledge can then be used to project the object locations into the spatial domain. The locations of the major scatterers in the spatial domain can be interpreted directly or can be used to synthesize additional data in UWB-SAR applications. The solution is novel in that it is a purely time-domain technique, eliminating artifacts caused by domain conversion. This chapter presents a theoretical basis for the technique, then validates the technique using full-wave simulations and experiments. The technique is shown to improve image quality when the initial data set is incomplete.

Chapter 5

The Sectional Imaging Technique

5.1 Introduction

Early detection of breast cancer is the key to reducing the risk of mortality. For that reason, different imaging modalities have been developed to detect tumours in the human breast. X-ray mammography is the most commonly used method for early screening of breast cancer, as it is relatively inexpensive [103], [104]. However, X-ray mammography has limited sensitivity, and in many cases fails to detect cancerous tissues in the breast [105]. Also, the use of ionizing radiation in mammography can be harmful to patients [106]. The American cancer society (ACS) recently recommended reducing the frequency of mammography for women due to drawbacks such as false detection and ionizing radiation. The ACS also pointed out the necessity of developing other early-stage screening methods [107].

Magnetic resonance imaging (MRI) using contrast agents provides the most distinctive images of the breast, especially in the case of dense breasts [108]. Even though MRI is a safe modality (non-ionizing), it is very expensive and time-consuming, which makes it an inappropriate option as an early stage screening and/or monitoring method. Computed tomography (CT) is a faster imaging modality. However, it uses X-rays, with a much higher dosage compared to X-ray mammography, and is unsafe for frequent screening. Even suppos-

ing CT could provide high spatial resolution, it does not provide high soft tissue contrast[109]; which is a key element for detecting tumours.

The high cost, complexity, and safety aspects of current methods highlights the necessity of microwave imaging, as an early diagnostic tool as well as monitoring tumour changes during chemo/radiotherapy. The contrast of the dielectric constant of various tissues is exploited by microwave imaging. To study the possibility of using microwave imaging for the detection and localization of breast tumours, extensive numerical and experimental studies have been performed which resulted in several approaches and algorithms. These approaches include methods such as confocal microwave imaging [65], [110]–[112], inverse scattering [113]–[117], and microwave tomographic imaging [118]–[123]. Confocal microwave imaging focuses mostly on identifying the presence and location of strong scatters in the breast rather than using all the reflections to reconstruct the breast image completely. This may lead to false or missed detection in some cases as the breast is a complex medium. Breast image reconstruction by solving the inverse scattering problem using iterative methods is computationally intensive and time-consuming.

Microwave tomographic imaging can be a supplemental method to the current modalities for breast tumour detection and imaging. This chapter proposes a new sectional imaging technique to reduce the errors due to the difference in permittivity of various tissues in the breast. This method is very fast and easy to implement, compared to frequency domain tomographic methods [114], [115], [123]. Time-domain data acquisition and processing avoid artefacts due to Fast Fourier transform (FFT) or inverse fast Fourier transforms (IFFT) which enhances the image quality. Experimental verification and demonstration through measurements on a 3D advanced breast phantom and their comparison with the MRI image of the phantom proves the competency of this method.

5.2 Problem Statement

High-quality image reconstruction using a time-domain method requires the knowledge of

group velocity in the medium of propagation. To reconstruct the image of a complex object such as a human breast with minimal error, the group velocity considered in signal processing has to be as close as possible to the group velocity of the pulse in the medium. Generally, image reconstruction in a multilayer medium is performed using the effective or average group velocities of the mediums, i.e., volumetric averaging. However, the dimensions of the high and low dielectric constant regions in the reconstructed image might appear larger or smaller than the actual dimensions. The exact dimensions and locations of different regions of a multilayer medium, in the reconstructed image, occur only if the correct value of the dielectric constant of each region is used.

A simple multilayer model is considered for simulations to observe the effect of different group velocities on a time-domain reconstructed image. The fat, glandular tissue and tumour have dielectric constants of 5, 36, and 45, respectively, with corresponding radii of 80 mm, 58 mm, and 8 mm. The matching liquid, $\epsilon_r = 3$, encloses the whole structure. As the structure is unchanged in the z-direction, the simulation is conducted in 2D using ideal/point transmitters and receivers. Two variations of the model are employed to illustrate the reconstruction. These two models are shown in Fig. 5.1(a) and Fig. 5.1(b), the former has all components centred whereas the glandular and tumour layer in the later situation are both off-centred in different directions.

Fig. 5.1(c) shows the reflected raw data, at the angle of 0° for Fig 5.1(b). This raw data shows the dielectric constants of different regions as well as the locations of reflections from different layers. The first and second reflections are due to oil/fat and fat/glandular tissue interfaces, respectively. The third reflection is due to the boundary between the glandular and tumour tissues. The fourth reflection is due to the tumour/glandular boundary on the other side of the tumour. The data can also be visualized by looking at all the transceiver data shown together in Fig. 5.2(a) and Fig. 5.2(d) for the centred and off-centred simulation models respectively. The three reflections are visible as well as interlayer reflections. The reflection from the fat and glandular tissue are overlayed with green and blue crosses respectively to illustrate their locations.

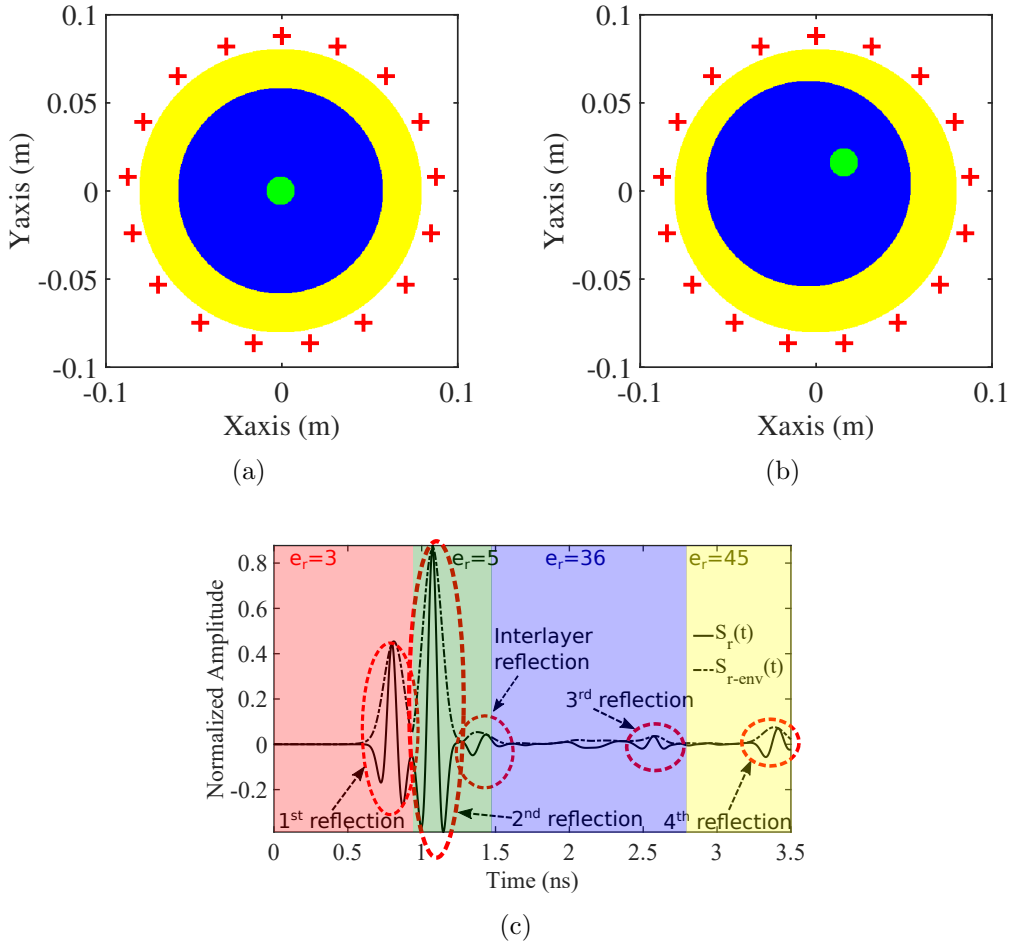

Figure 5.1: (a) Centred three layer simulation set-up. (b) Off-centred three layer simulation set-up. For both simulations, the outer yellow layer is $e_r = 5$, middle blue layer is $e_r = 36$, and the central green layer $e_r = 45$, the red crosses represent the locations of the transceivers. (c) Pulse and envelope pulse from the simulation with permittivities overlayed.

The shape of the received pulse depends on the antenna transfer function, target material, and the number of reflections that the pulse undergoes [18], [124]. In this case, as the input is an idealized point source, there are no antenna effects. Therefore the input and received pulses are both second derivative Gaussian pulses. This knowledge is helpful for identifying the interlayer reflections. The interlayer reflections do not provide any additional information to the reconstructed image; however, they might degrade the image. Matched filtering and time-gating can be applied to reduce these undesired effects [125].

After analysing the scattered pulses, the next step is the image reconstruction. Image

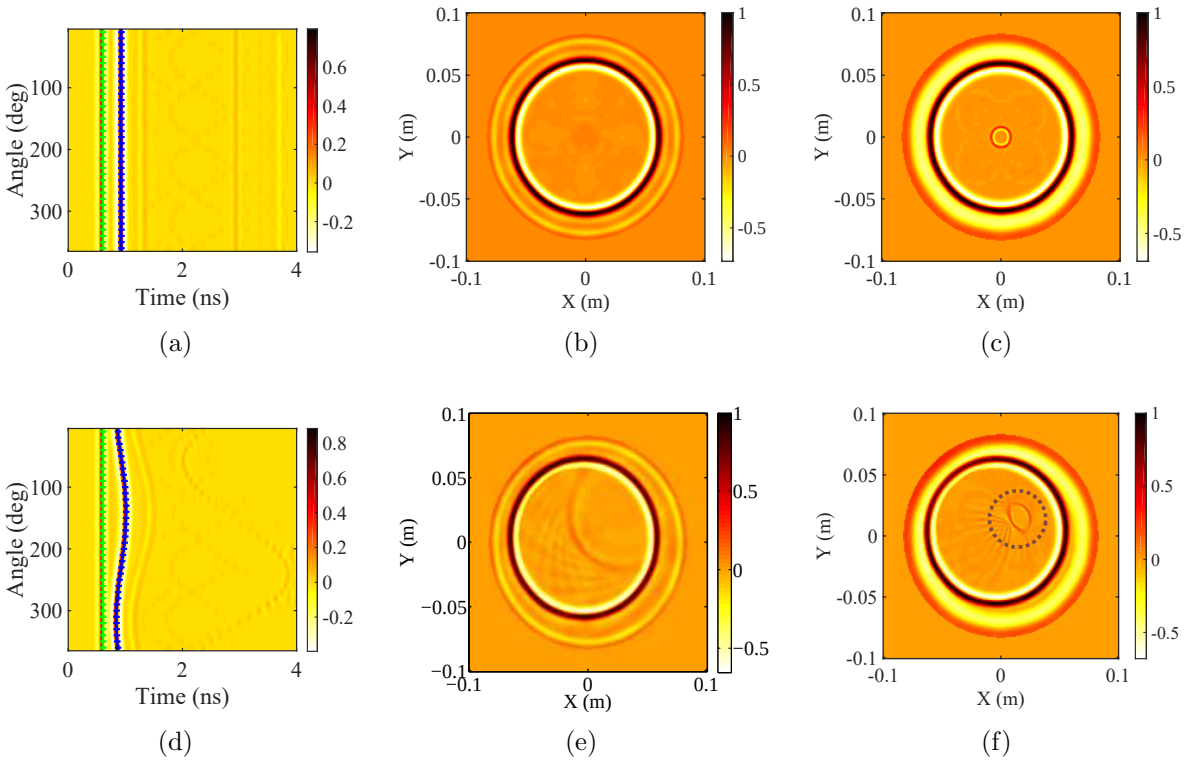

Figure 5.2: Three layer simulation reconstruction results. Time data showing the transitions into different layers for, (a) centred case, (d) off-centre case. Reconstructed images using the Average group velocity for, (b) centred case, (e) off-centre case. Reconstructed images using the sectional method using the sectional method for, (c) centred case, (f) off-centre case.

reconstruction is performed using the Global Back Projection (GBP) in the time domain, which works very well for UWB pulses [71], [126]. Moreover, image and signal processing techniques such as positive image [127] and envelop detection can be applied to acquire more information about the targets (i.e., tumours). For a pulse to reach the tumour, it experiences three different group velocities: oil, fat, and glandular tissues, which need to be considered to reconstruct the image fittingly. Here the first image is reconstructed based on the average speed in the medium, using the volumetric average. Fig. 5.2(b) and Fig. 5.2(e) show the reconstructed images for the centred and off-centred models respectively. As one can see, the tumour is not detected and imaged in Fig. 5.2(b) and Fig. 5.2(e). Additionally, in both the cases, the diameter of the fat and glandular tissue are enlarged. These are all due to the difference between the actual group velocity and the average group velocity causing incorrect

convergence of the weighted sum of pulses for the image reconstruction.

To solve this problem and to minimize the errors, the image can be reconstructed section-wise with different values of dielectric constant for each individual layer. The sectional imaging can be automated by detecting the most significant reflections using an algorithm developed in Section of 4.1.1. The algorithm compares the reflection at each aperture location to find the major tissue interfaces inside the breast. As the algorithm uses the data from all aperture locations together is able to rigorously find the major reflections even in the presence of high levels of noise.

Assuming the breast layers are, somewhat continuous and circularly symmetric, allows the data to be segmented into different regions with a specific dielectric property. In a real case scenario, the dielectric constant of the layer is not known. In that case the way forward is to use the average electrical properties, available in the literature [128], based on the age group of the subject. Inverse methods can also be used, for coarse mapping of the electrical properties of the breast, based on the measurements.

In this simulation, the model is divided into three regions, i.e., fatty and glandular tissues and the matching liquid with three different group velocities. After outlining the regions, the image of each regions is reconstructed using the approximate dielectric constant of that region and appropriate time delays. The section-wise image reconstruction method will provide improved results compared to using the average dielectric value. By dividing the target scene, this method uses better approximations in the different regions compared to the conventional method resulting in higher image quality. Moreover, methods such as solving a coarse meshing inverse problem [129] can provide better estimates of the values of each region. Additionally, the dielectric constant of the outer layer can be determined through measurements.

Fig. 5.1(c) gives an illustration of the sectional technique. The reflections at the boundaries are detected, then the raw data are divided into a number of sections. The sections are reconstructed separately from the outer layer to inner layer. While a section is reconstructed, all other sections are set to zero, and appropriate time delays applied. Finally the images of

the different layers can be added together to create the final image.

The sectional image reconstruction technique is implemented for the simulation models demonstrated previously in Fig. 5.1. The reconstructed images using the sectional technique are shown in Fig. 5.2(c) and Fig. 5.2(f). The images are much more accurate than the image using the average group velocity, due to the fact that energy is converged to the right location in the reconstructed images. For example, Fig. 5.2(c), 5.2(f) are high quality images and the tumour is very clear. However, in Fig. 5.2(f) the tumour shape has been changed to an oval, this error is due to the reconstruction process of sectional imaging. As is discussed earlier, this method works better for layers in circular shape. If the layers are not in circular shape, the target in the line of sight may not get affected, but off the line of sight targets get affected due to the error in the path length of the signal in the outer layers. In this example it results in the tumour expanding in the direction where the assumption of circular layers are not met; leading to a oval shape as shown in Fig. 5.2(f).

5.3 Reconstructed Images of the Advanced Phantom

This section presents experimental measurements and discusses the reconstructed images of the advanced phantom. The advanced phantom contains a $1cm^3$ emulated tumour. Fig. 5.3(a) shows the phantom structure in different views. A $1cm^3$ plastic container is filled with solution to emulate the tumour. The tumor located in the middle of phantom affixed to the ABS wall as shown in the 3D view. The tumour container is made using a plastic of half a millimetre of thickness in order to eliminate the container effects on the measurements.

A slice of the phantom at tumour height is shown in Fig. 5.3(a). The advanced phantom is scanned in the circular path to acquire the raw data. Images are reconstructed, in the time-domain, within a square $10cm \times 10cm$ area that encloses the biggest dimension of the phantom. Different formats of the images are shown to elevate different dielectric interfaces and sharpen the boundaries of the target. For example, the raw image (I) uses the complete data of the received pulse and its normalized image intensity. The absolute image is defined

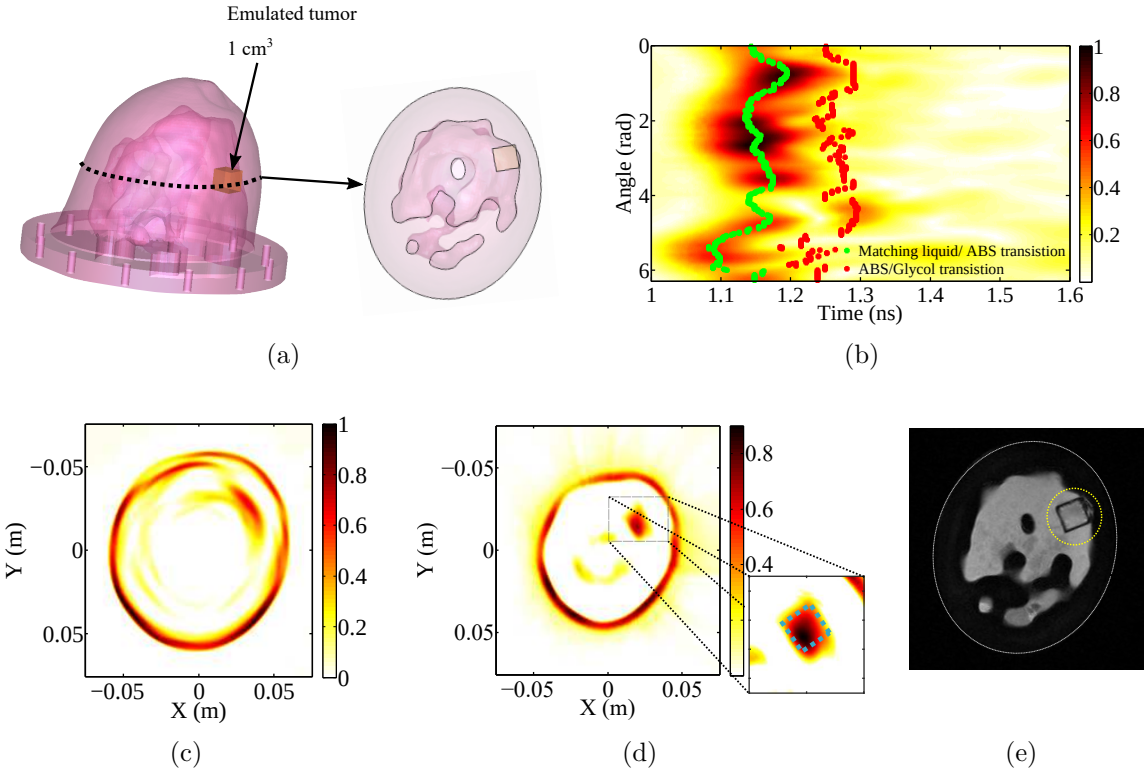

Figure 5.3: Cancerous advanced phantom; (a) Transparent phantom in different views (the cube region is the simulated tumorous tissue). (b) Plot of transition into different medium. Reconstructed positive images using, (c)ϵ_{avg}, (d) Sectional reconstruction. (e) MRI image for comparison.

as abs(I), applied on every pixel of the image. Likewise the positive image is defined as the sum of: abs(I) + (I) at every pixel. Similarly the negative image is is defined as: abs(I) - (I) at every pixel [127].

Fig. 5.3(c) shows the positive image reconstructed using the average group velocity in the medium. As it can be seen, the image is blurred, the diameter of the fat, and the glandular tissues also changed, due to the difference between actual and the average group velocities.

To solve this problem and minimize the errors, the sectional image reconstruction method that uses different group velocities is applied. The major reflections, at the matching liquid/fat interface and the fat/glandular interface are found and displayed in Fig. 5.3(b). Fig. 5.3(d) shows the sectional reconstruction of the image that is vivid and demonstrates the dimensions of phantom, shape and location of the tumour fittingly. The square shape of

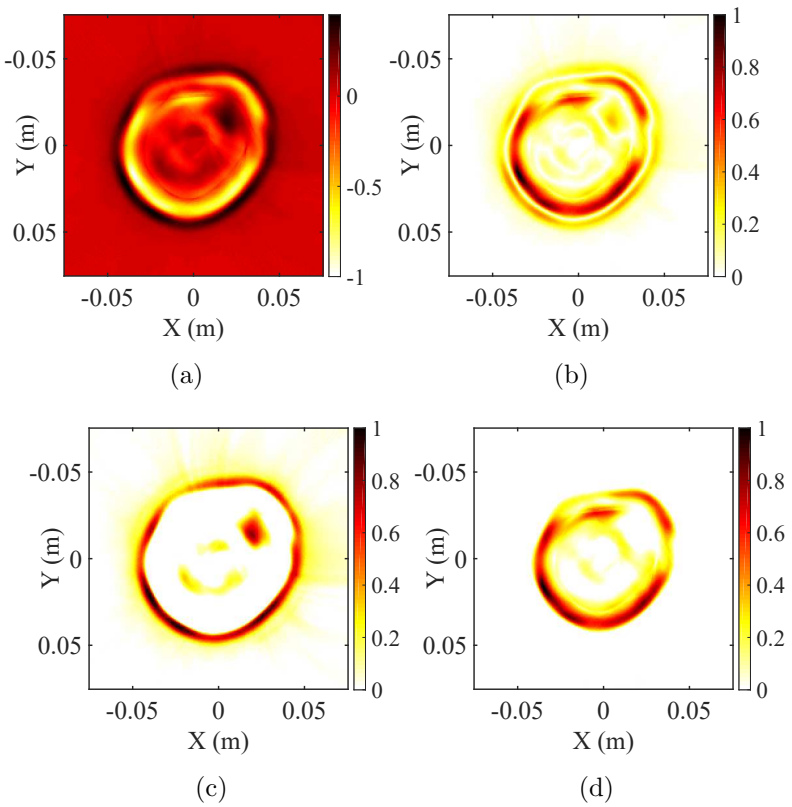

Figure 5.4: Reconstructed images using the sectional method. (a) Real image. (b) Absolute image. (c) Positive image. (d) Negative image.

the tumour is clearly visible, additionally the dimensions are 1.1×1.1 cm which is very close to the actual dimensions of 1×1 cm. We also scanned the phantom using a 3T MRI system to evaluate the competency of the UWB-CSAR technique. Comparison between Fig. 5.3(d) and Fig. 5.3(e) demonstrates the ability of UWB-CSAR for complex applications such as breast scanning. Fig. 5.3 uses the positive images to show the high dielectric contrast interfaces. The visual impact of the blurring in these images can be reduced by applying image processing techniques such as filtering and thresholding. Fig. 5.4 contains shows the different possible image formats.

Based on the relative contrast between the two layers, different interfaces will be more visible by using different image formats [127], namely the raw image, absolute image, positive, and negative images as shown in Fig. 5.4. The raw image is shown in Fig. 5.4(a), this contains all the information of the discontinuities. Fig. 5.4(b) shows the absolute image, which also

contains all the information of the discontinuities. Fig. 5.4(c) shows the positive image, which highlights the interfaces of low to high dielectric contrast. Here we can see the tumor very clearly. Fig. 5.4(d) shows the negative image, here the interfaces from high to low contrast have been highlighted.

5.4 Discussion

The results obtained in the experiment clearly demonstrate the impact of using a variable group velocity on the quality of the reconstructed image. The results also demonstrate the potential of UWB radar, with CSAR image reconstruction methods, for breast cancer screening. Operating in the time domain, allows for accurate time referencing and a simpler calibration procedure. However, there are some limitations to the proposed technique. Accuracy of microwave imaging depends on the contrast in electrical properties of tissue regions and tumours. Image brightness depends on the amplitude of the reflected signals, which depends on the contrast in electrical properties of different interfaces. If the tumour is formed inside the fibro-glandular region, sometimes the contrast between neighbouring tissue and the tumour can be below 10% making imaging very difficult. However, in some cases, signal processing techniques can be used to improve the image quality to an acceptable level.

The phantom used in this experiment does not consider the effect of skin and the dispersive nature of the adipose tissue. The effect of skin and dispersive nature of adipose tissue may cause a further attenuation of the signal. However, numerical simulations show that the distortion of the signal is not significant for the given operating frequency band.

The quality of the reconstructed image depends on the accuracy of the dielectric constants of the various layers; in a clinical applications the permittivity will vary among different subjects [128].

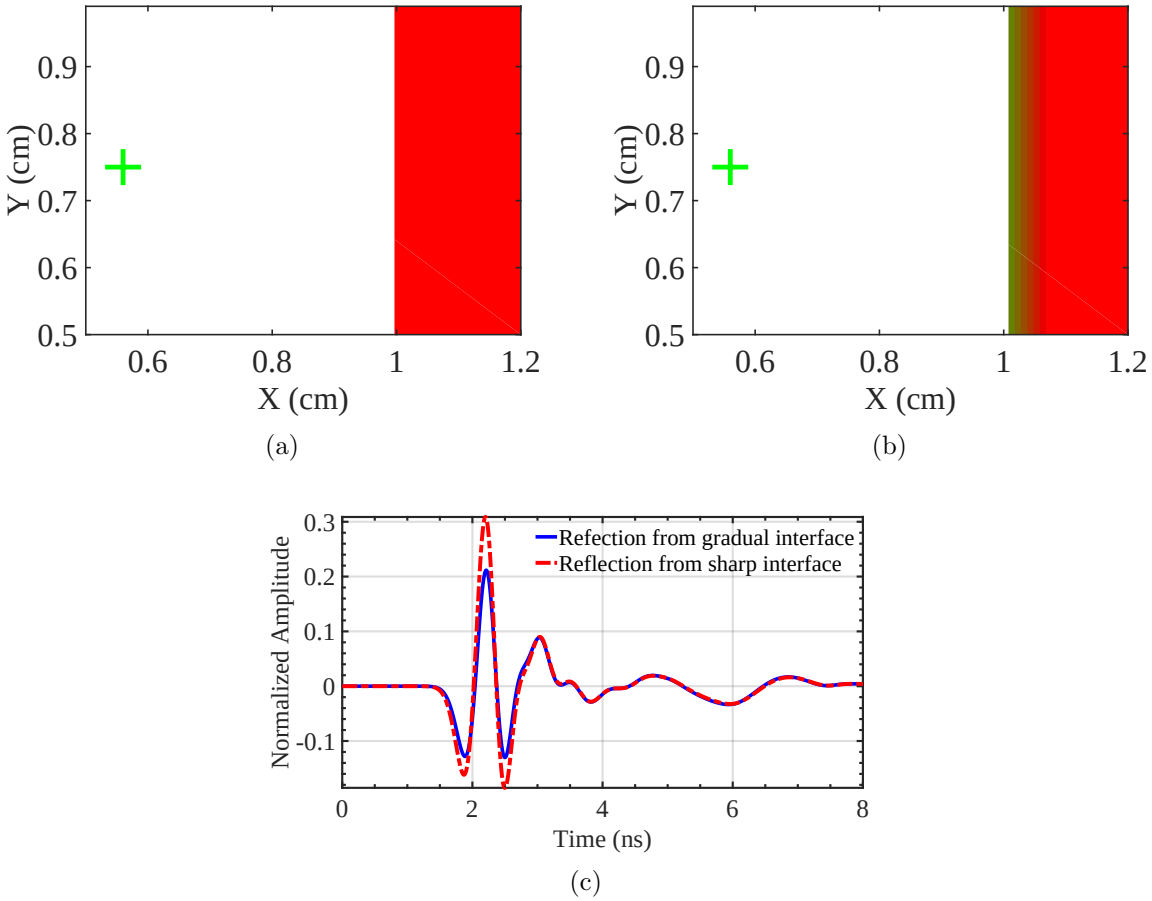

Figure 5.5: Simulation to examine the effect of discrete interfaces, (a) Simulation setup with a sharp interface from $\epsilon_r = 1$ to $\epsilon_r = 5$. (b) Simulation setup with a gradual interface from $\epsilon_r = 1$ to $\epsilon_r = 5$ over a gradient of 9 mm. (c) Comparison of reflected pulses from the interfaces.

5.4.1 Effect of Gradual Transition from Layer to Another Layer on the Reflected Pulse Characteristics:

The boundaries between different layers of the phantom are sharp, unlike in vivo, where the layer to layer transition is gradual. To study the effect of gradual transition between the layers, the reflected pulses are compared with the sharp transition case. The pulse width considered is 100 ps, and its spatial pulse length is 15 mm in the matching liquid. Fig. 5.5(a) shows the sharp transition between air and adipose tissue. Fig. 5.5(b) shows the transition between air ($\epsilon_r = 1$) and adipose tissue ($\epsilon_r = 5$) of transition length 9 mm. Fig. 5.5(c)

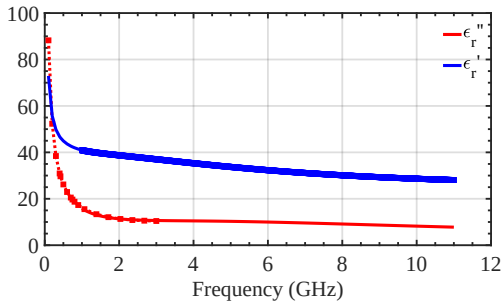

(a)

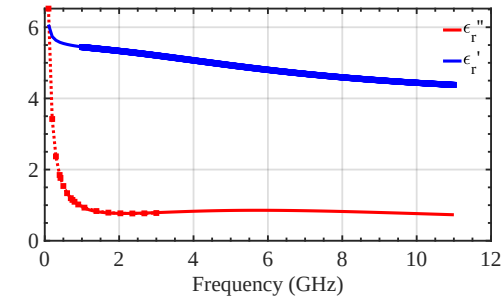

(b)

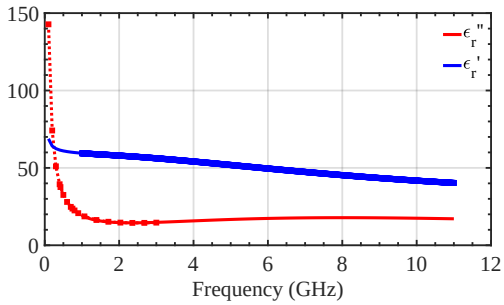

(c)

Figure 5.6: Tissue properties used in the CST simulation; (a) Electrical properties of skin layer. (b) Electrical properties of adipose layer. (c) Electrical properties of the breast glandular tissue.

shows the reflected pulse characteristics of abrupt and gradual transitions. It is seen that the amplitude of the reflected signal has been affected slightly; the other parameters remains the same. This study confirms that the transition has no significant effect if the transition length is smaller than the spatial pulse length.

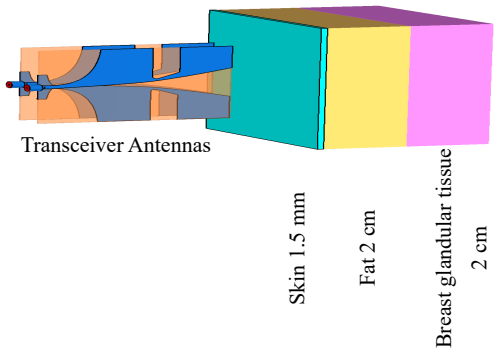

Figure 5.7: Simulation setup showing the breast layers.

5.4.2 Effect of Skin and Adipose Tissue with Dispersive Electrical Properties:

The measured electrical properties of skin, adipose, and glandular tissues as a function of frequency [130] are shown in Fig. 5.6. Several numerical studies are conducted to quantify the effect of skin and adipose tissue whose electrical properties are shown in Fig. 5.6. The simulation setup, along with the transmitting and receiving antennas is shown in Fig. 5.7. The gap between the antennas is 2.54 cm, and the medium around the model is a matching fluid whose dielectric constant is 3. The antennas are placed 1 cm away from the first layer. The skin layer is considered as 1.5 mm thick followed by the adipose and glandular tissues with 2 cm thickness each. Fig. 5.8(a) shows the different configurations of the study. Reflected radar pulses for various cases are shown in Fig. 5.8(b). The calibration procedure to remove the mutual coupling between the antennas and simulation boundary effects has been followed as described in [4], section III.

The reflected signal from the all layer configuration contains the energy reflected from all the interfaces, including the matching liquid-skin, skin-adipose tissue, and adipose-glandular tissue interfaces. As can be seen, the first interface, i.e., matching liquid and skin interface reflects most of the energy. To analyse the characteristics of the reflected pulse originated from glandular tissue region, the reflections from the first two layers need to be calibrated by subtracting the reflected signal from the skin-adipose case from the reflected signal from the

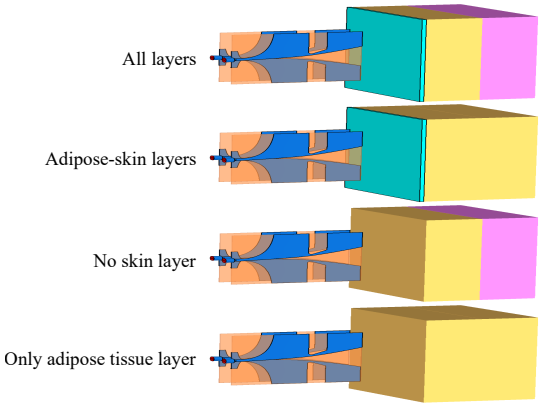

(a)

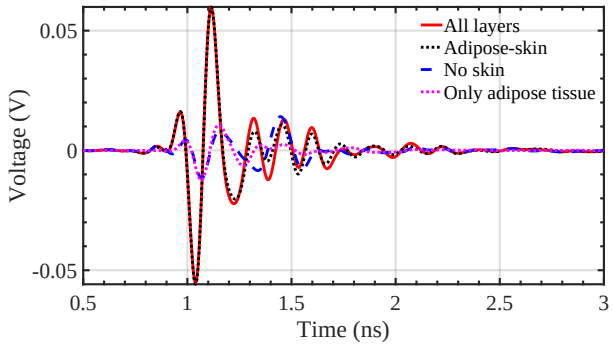

(b)

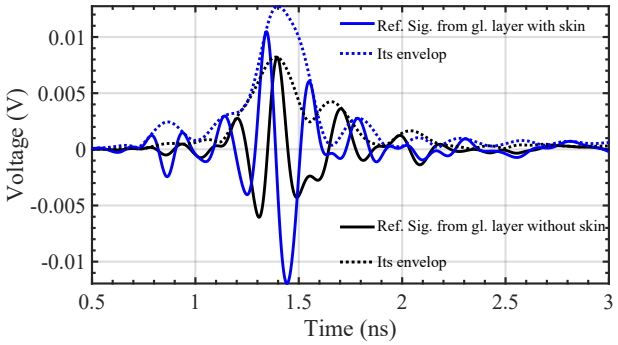

(c)

Figure 5.8: Numerical study to investigate the impact of not including a skin layer. (a) Different simulation setups considered. (b) Reflected pulses for the different setups. (c) Comparison of the reflections emanating from the glandular tissue when the skin is included to when it is not.

all layers case. The calibrated signal shows the effect of skin on the reflected pulse originated from the glandular region. Similarly, subtracting the reflected signal of the adipose case from the reflected signal of the no-skin case provides the reflected pulse originating from

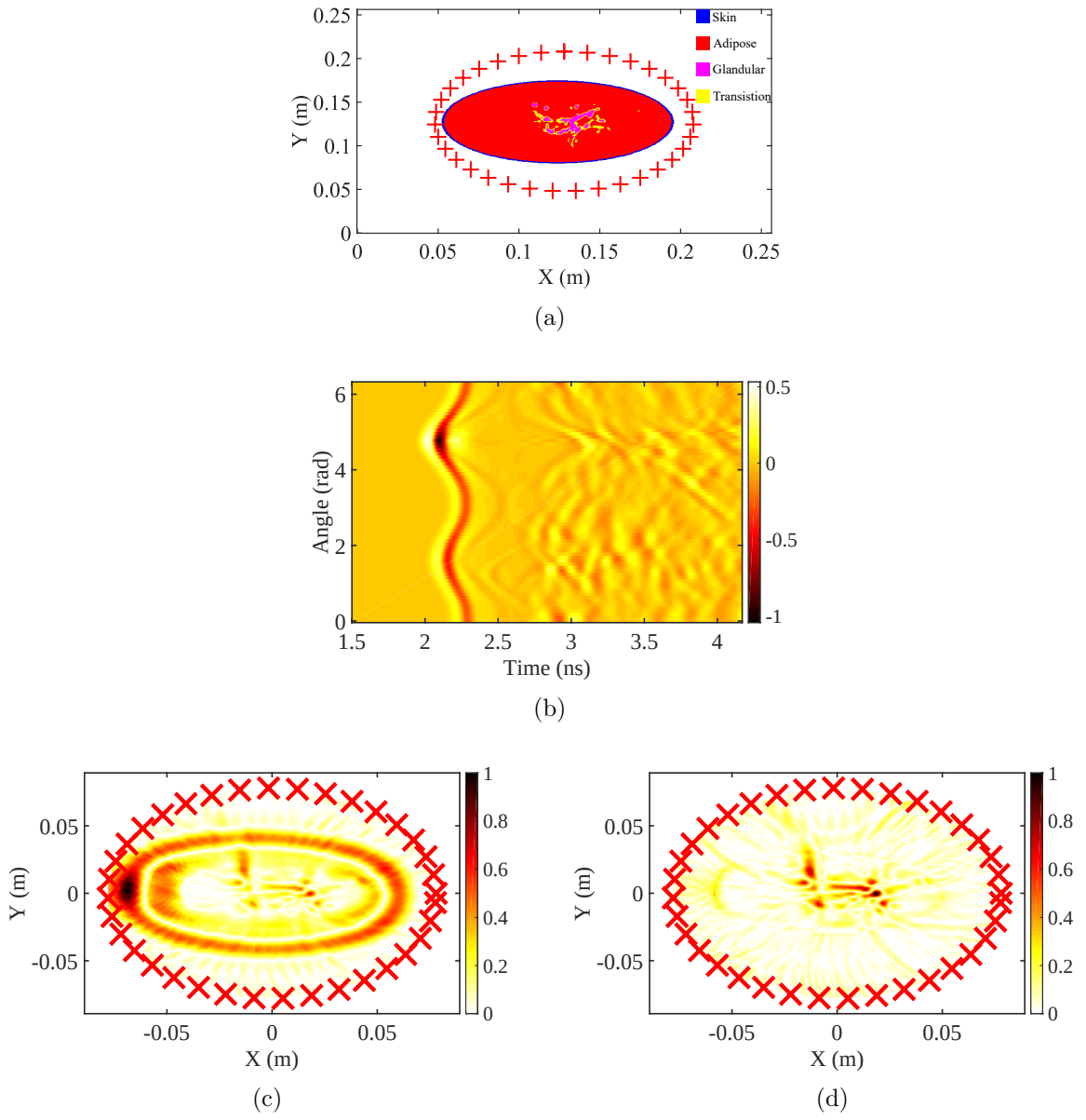

Figure 5.9: Simulation demonstrating how the large skin reflection could be mitigated. (a) A cross section of numerical phantom. (b) Sinogram of the raw data. (c) Reconstructed Abs(I) using the sectional imaging method, with skin layer. (d) Reconstructed Abs(I) using the sectional imaging method, without skin layer.

the glandular region without the skin effect. Fig. 5.8(c) shows the reflected pulses with and without skin. Quantitatively the results indicate that neglecting the skin increases the reflected pulse amplitude from the glandular layer by 1.9 dB in terms of voltage.

The effect of dispersive properties of adipose tissue can be analyzed by conducting the

simulations shown in Fig. 5.8(a) by replacing the adipose tissue with ABS plastic. Following the same procedure described above to calculate the reflected pulse from the glandular region and comparing them for the case of adipose tissue and ABS plastic cases. The results indicate that the phantom without skin layer and ABS plastic instead of dispersive adipose tissue have higher reflected signal than the more realistic scenario by 6.16 dB in terms of voltage.

Strong reflections from the matching liquid and skin interface diminish the image brightness of internal layers and tumours. However, the effect of the skin on the reconstructed image can be mitigated by the proposed sectional imaging method. As stated earlier, in this method, image is reconstructed layer by layer, from outside to inside, with appropriate group velocities. Reconstructing the image without skin reflections enhances the contrast of the internal layers and tumours, which may provide a better perspective of tumours. To illustrate the effectiveness of sectional imaging method, a numerical phantom [131] is considered. Fig. 5.9(a) shows a cross-section of the numerical phantom with data collection aperture locations. Fig. 5.9(b) shows the sinogram of the raw data. In this graph, the bright red colour indicates the skin boundary, which shows the strongest reflections. Fig. 5.9(c) shows the reconstructed image using entire data in the sinogram. Fig. 5.9(d) shows the reconstructed image without strong reflections, i.e., without skin interface.

As one can see from Fig. 5.9(d) that using time-domain sectional imaging method the internal layers, and boundaries of the breast can be imaged more effectively. The glandular features are clearly visible, and the correspondence with the shape of the phantom is good. Using this method, the effects of the unwanted layer/s can be mitigated. In this case, removing the first layer, that is skin layer, increases the brightness of the glandular tissues in the image.

5.5 Chapter Summary

This chapter presents a sectional image reconstruction method that can be applied to reduce image distortions due to group velocities errors in different regions. The preliminary

results from measurements and comparison with MRI image of the phantom demonstrated the capability of this method to improve the image quality. The experiment is conducted on a widely used breast phantom for validating the proposed method. This study clearly demonstrates the importance of sectional imaging to improve the image quality. The use of the phantom is validated by analysing the shortcomings of the model and demonstrating that model presents adequate quality to demonstrate the impact of the algorithm. This chapter is based on Section IV and V from [4]. Section I, II, and III of that document are part of the thesis project of another student and should are not claimed as part of this current thesis project.

Chapter 6

UWB Non-Linear Radar: Simulation, Theory, and Experiments

6.1 Introduction

Certain radar applications contain such low radar cross-sections (RCS) that targets are not visible above the noise floor using conventional radar. Exploiting non-linear characteristics inherent in the object, or making them part of the transponder, can allow these objects to be detected. Previously this is done using harmonic radar in the frequency domain. This chapter proposes the use of time-domain analysis to solve the same problems. This technique shows promise as an alternative to using harmonic radars in situations where the time-domain is preferable to the frequency domain based on complexity, cost, resolution and need for high power requirement of the harmonic radars.

With the exception of ferromagnetic rocks, everything in nature behaves linearly when radiated with electromagnetic waves. However, non-linear devices are ubiquitous in electronics and electrical devices. Any electronic device more complicated than a few components likely contains an np junction.

This can be exploited in certain applications in which ordinary radar methods are not suitable. One such application relates to the tracking of endangered or invasive species of small size. For large threatened animals, radio transceivers can be fixed and used to track the animals. However, the radio collars cannot be made arbitrarily small. For smaller species, another way of tracking is required. This usually consists of affixing a diode with some

leads to the organism and altering the receiver of a more conventional radar transceiver to filter out all but the second harmonic of the transmitted frequency. This allows for a reduction of the noise floor and allows objects with small radar cross-section (RCS) to be tracked [27]. Harmonic radars have been used to track species of interest, such as the endangered snails [24], invasive hornets [132], bees [25], [26].

A second similar application is the detection of electronics that have not intentionally been made as visible radar transceivers [27]. This can include exploiting non-linearities to interface with sensors [27], using harmonics to measure dopplar [27]. As well as detecting the presence of electronics themselves, such as surveillance equipment [27] or remotely triggered explosive devices.

For the applications which are concerned with localization and detection of objects, such as, organisms with an attached diode, as well as the detection of electronic equipment, the process consists of a transmitter, often consisting of a sweeping antenna [132]. In the receiver, the low noise amplifier, local oscillator, and intermediate frequency band filter, are all designed for $2f_0$, where f_0 is the transmitted frequency. The use of $2f_0$ significantly reduces the effect of clutter, reducing the overall noise figure.

The use of harmonic radar suffers from some issues. Some implementations have used a limited range on the order of only 5 ft [24]. Additionally, range resolution is an issue [132]. In order to increase resolution, additional techniques have been employed, such as pulse pseudonym codes [25].

We propose using time-domain radar as an alternative technique to using harmonic radar. Instead of emitting a frequency f_0 and receiving $2f_0$, the time-domain equivalent consists of transmitting two pulses, $V(t)$ and $-V(t)$ and measuring the differences of the received signal.

Using a time-domain approach can be a huge improvement in certain aspects. Firstly much of the modeling of the non-linear scatterers occurs in the time-domain [133]. Secondly, there are certain aspects of the time-domain analysis that can give much higher SNR given the parameters of a given architecture. Lastly, the time-domain gives a location directly, as

opposed to a harmonic approach in which additional processing steps are required all the while adding noise.

6.2 Concept

Using non-linear radar in the time-domain is conceptually simple. First, a pulse $V(t)$ is transmitted towards the object under test, the response is then measured. The inverse of the pulse $-V(t)$ is then transmitted, and the response is measured. The two pulses from the two situations are then calibrated, and the ambient components are subtracted. The pulses can then aligned to account for any time drift. The non-linear components are then measured using the following formula:

$$C(t) = (V(t))^2 - (-V(t))^2 \tag{6.1}$$

If the object under test does not contain any non-linearities then the response would ideally be zero, in reality it is not zero and is made up of the noise from the system and non-linearities present in the receiver.

A simulation is performed to illustrate the process. The simulation is performed in CST. A plane wave is incident upon a metal rod. In one situation, the metal rod is solid. The simulation is performed again, this time a slice is removed from the centre of the rod, and a diode is placed to bridge the gap. The setup is shown in Fig. 6.1(a). The reflected pulses from the $V(t)$ situation are shown in Fig. 6.1(b). There is some additional ringing in the pulse from the non-linear object but the dramatic contrast is shown after the application of eq(7.1). The output results are shown in Fig. 6.1(c). As this is a simulation, the inversion of the metal response adds to exactly zero, this is not the case in a real world situation. Using this technique, the presence of non-linear components can be detected. Due to the effect of the ringing, depending on the processing, the range resolution may be lower than for traditional targets, based on the bandwidth of the pulse.

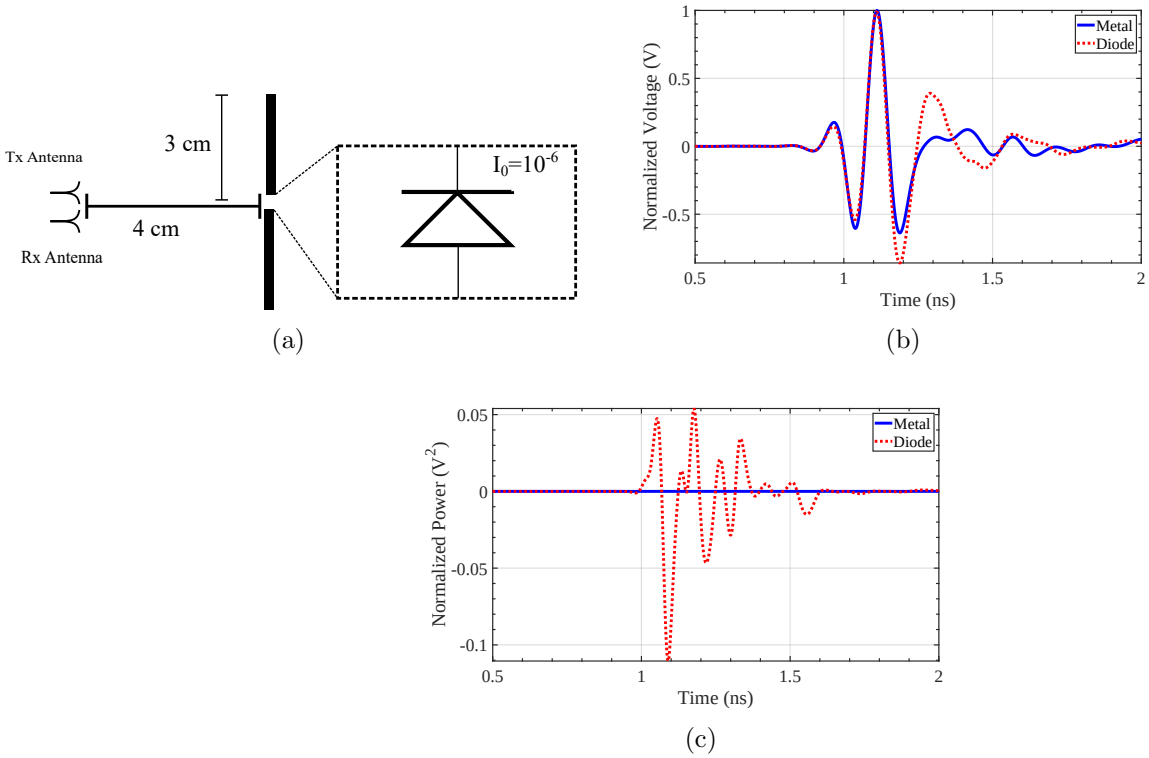

Figure 6.1: (a) Simulation setup. (b) Calibrated pulses comparing the reflection off a metal rod to a metal rod with a diode inserted in the middle. (c) Difference of squares comparing the metal rod to metal with diode.

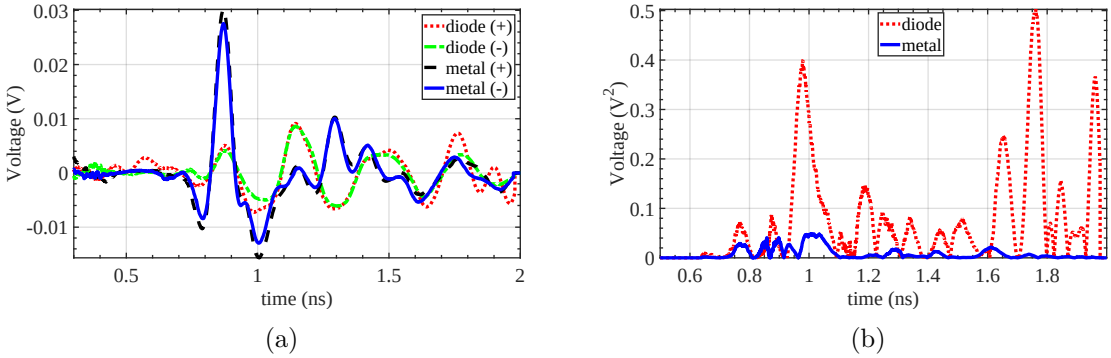

Figure 6.2: (a) Calibrated pulse after ambient subtraction, inversion, and lining up for a single aperture location. (b) Difference of squares.

6.3 Experimental Proof of Concept

The experimental setup consists of placing the device under test on a Styrofoam block and making a CSAR measurement of it. The two devices considered are a metal rod of length

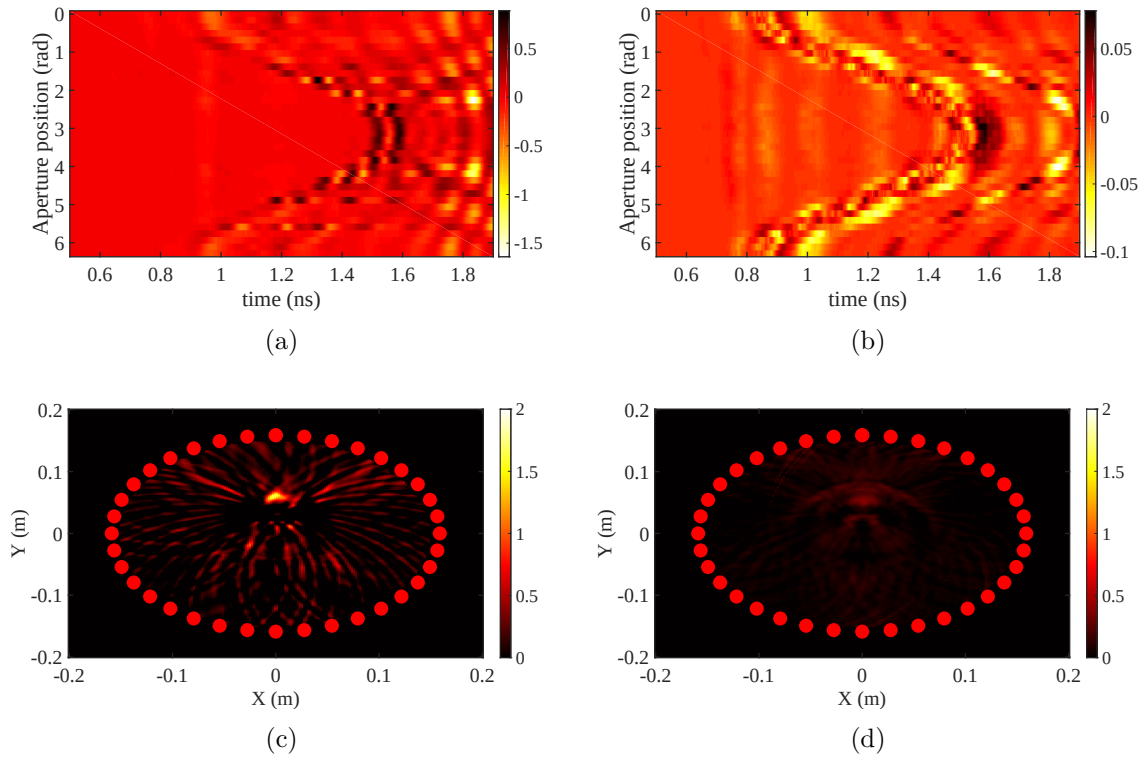

Figure 6.3: Difference of squares data with all apertures shown together from the (a) non-linear sensor, (b) Metal rod. Reconstructed positive images (c) From the diode, (d) From the metal rod. Both plots are normalized to the same real power level.

3 cm, and a diameter of 2 mm, the non-linear device consists of a metal rod of length of 3 cm and, diameter 1 mm which is cut and a diode NP42342 is placed between the two halves. The ambient calibration is done as explained previously [71]. After subtraction, the results from a single aperture position can be viewed. As this experimental procedure involved flipping the antenna orientation by hand, some drift and noise have been introduced. To deal with this, after the negative pulse is inverted, and the first peaks are aligned. After inverting the negative pulse and inversion, the results at a single aperture location, the results are shown in Fig. 6.2(a). As can be seen, due to the thicker metal rod used and subsequent increased RCS, the reflections from the metal are larger overall than from the non-linear sensor.

This data is now ready for the non-linear processing. Taking the difference of squares of the two pulses, the non-linear features are elevated. These results are shown in Fig. 6.2(b). Despite the metal having an overall larger RCS and reflection, the difference of squares

elevates the reflection well above the noise floor of a metallic reflector.

The data from the whole aperture is shown in Fig. 6.3(a) for the non-linear target and Fig. 6.3(b) for the metal target. The non-linear behaviour is around 10 dB above the data from the metal. Additionally, the ringing effect of the sensor shows prominently as compared to the metal. We can see more of angular dependence manifesting in the sensor data, whereas the metal appears to be more isotropic in that plane.

We can see that a significant amount of the non-linear behaviour for the sensor, manifests as ringing of the pulse. However, when the data is projected into an image, the non-linear object is properly localized as shown in Fig. 6.3(c). The image for the metal rod is shown in Fig. 6.3(d). The power levels are kept constant between the two images which leads to the diode target showing much stronger in the final reconstructed image.

6.3.1 Conclusions and Future Work

The strengths of conventional frequency domain harmonic radar are the ability to use highly discriminative analog or digital filters in order to remove the baseband and focus solely on the second harmonic. However, reflections in the second harmonic have an inherent power loss of 13.5 dB, which mitigates the advantage of the technique, and requires higher operating power levels. The strengths of employing non-linear radar in the time domain is a power advantage as the scattered pulse contains the energy of all harmonics, including the fundamental frequency. The asymmetric pulse scattering behaviour of the PN junction, in forward and reverse bias, allows additional suppression of linear clutter and may allow localization of even targets of smaller RCS. The secondary advantage of non-linear radar in the time domain is inherent in technique and that additional techniques like coding are not required for localization to be achieved.

The major barrier to the continuation of this work, is the pulse inversion. This technique requires two pulses $V(t)$ and $-V(t)$ to be created and to have quite good fidelity. In this experiment, it was done by physically rotating the antenna 180° in order to create the positive and negative waveforms in the dominant polarization plane of the antenna. There

are certain techniques for pulse creation that lend themselves towards producing positive and negative waveforms without the need for mechanical actuation [134]. If these techniques can be further developed to produce high fidelity pulses, the potential applications of this technique will increase.

Time-domain non-linear radar has not previously been proposed in the literature. Here is it proposed and the technique is validated using simple simulations and some small scale experiments.

Chapter 7

Microwave Based Stroke Classification and Imaging

7.1 Introduction

Each year in the United States alone around seven hundred and ninety five thousand people experience a new or recurrent stroke [135]. Over an individuals lifetime, one in 5 women and 1 in six men will have a stroke. Among the survivors, stroke is a leading cause of serious long-term disability. The total cost of the disease has been estimated to be 45 billion euros per year in Europe alone [136]. To mitigate deaths and the long term effects of strokes, rapid response is crucial. Every 30 minute delay in the application of treatment leads to significantly worse outcomes [137], [138]. Thus, getting appropriate treatment as soon as possible is paramount.

There are two main types of stroke, ischaemic (ISH), which consists of a blockage to the flow of blood to the brain, and haemorrhagic (ICH) which consists of bleeding of the brain. The distribution of strokes is that 87% are ISH and 10% are ICH. The remaining are Subarachnoid Haemorrhage (SAH) which are related to head trauma and are more similar to ICH strokes.

Treatment differs for the different stroke types. If the stroke is determined to be of type ISH, the primary course is to attempt to remove the blockage. This is normally done by an emergency intravenous (IV) medication. The injected drugs work to dissolve the blood clot.

In the case of ICH stroke the fastest acting course of action is to be given drugs or a blood transfusion to remove any blood-thinning medications in the advent the patient is taking them. At a slightly slower time scale both stroke types can be treated with different types of surgeries.

From this material we can conclude that the differentiation of stroke type is paramount in being able to apply rapid treatment as the treatments of one type will lead to even worse reactions in the case of the other stroke type. To determine the type of stroke, doctors have several tools available. The main tool used is a brain scan using magnetic resonance imaging (MRI) or Computerized tomography (CT) scan. Using the information from the scans in conjunction with blood tests and a physical exam doctors can prescribe treatment.

For large, rural, sparsely populated areas such as that of northern Alberta, there can be significant delays in getting to a facility with adequate medical resources such as an MRI or a CT scanner. Recently, a solution to this has come in the form of a stroke ambulance. This consists of a custom made ambulance equipped with a CT scanner, video-conference capabilities, and laboratory analyser. The cost of the single vehicle to serve the Edmonton area is billed at 3.3 million dollars Canadian. Much of the cost is due to the CT scanner whose requirements led to the need of a custom built truck which can be seen in Fig. 7.1. Due to the cost there is currently only one vehicle operating in the region. Due to this, when an individual has a stroke in a remote region, a conventional ambulance is dispatched from their local healthcare center (which does not contain a CT scanner), meanwhile, the stroke ambulance is dispatched from Edmonton. When the two ambulances meet, the patient is transferred to the stroke ambulance, which then takes the patient to one of the large metropolitan hospitals in the Edmonton region during which a CT scan can be performed and in the advent an ISH stroke is found to be likely, treatment can be deployed before even reaching the hospital.

To improve the response rate and decrease costs microwave imaging has been proposed as a solution [139]–[142]. Because microwave imaging systems are significantly smaller, cheaper, and more portable. Microwave systems could be implemented at more locations, such as

smaller health care centres that do not posses an MRI or CT scanner. They could also be implemented in ambulances, however, due to smaller size and cost, microwave systems could be implemented much more widely than the implementation involving the stroke ambulance.

There are several issues related to microwave being a feasible solution to imaging for stroke. Microwave image resolution cannot provide similar resolutions to MRI or CT. Additionally, some sources have shown that the dielectric changes due to stroke are of relatively low contrast [143], with ICH stroke causing decreases of around 20% and increases of 10% for ICH stroke when compared to normal values.

Previously different aspects of the problem have been investigated. Modelling for simulations have been investigated [144], as have phantom creation [136]. Different techniques and systems have been designed [139]–[141], [143], [145]–[147]. Of these previous projects [139], [140] use very simplistic models which do not contain the complexity of the problem, [141], [143], [147] make use of a matching liquid which may also not be representative of a realistic scenario. Overall, they do not demonstrate high quality imaging which demonstrates that this is a suitable method to conduct brain imaging. Only [139] attempts to present stroke classification instead of imaging, however, the use of such a simplistic model does not indicate whether this technique is promising.

Instead of a purely imaging based diagnosis we present a technique on attempting to classify the type of stroke based on a modified correlation technique inspired from the field of ultrasound imaging. Correlation based radar has been shown to increase the effect of movement above that of stationary objects by up to 100 dB [148]. Because of this the stroke classification can be obtained by imaging over time and measuring the movement over time. The downside of this technique is that it is only useful at early stages of the stroke while large-scale fluid displacements are still ongoing. However, as microwave imaging of stroke is proposed purely as a early classification this is a limited restriction of this technique. Additionally, the measurement over time can be used as a continuous measurement technique where microwave sensing has also been suggested as an option [136] to monitor the state of the stroke over the period of hours to days, where MRI and CT and too expensive an CT is

Figure 7.1: Stroke ambulance. Image courtesy of Alberta Health Services.

too damaging for such a long term exposure.

This chapter is organized as follows In Section 7.2 the simulation model is described. Section 7.3 shows the results of the simulation. Finally the chapter is concluded in Section 4.4.

7.2 Simulation Model

The head contains many complicated layers of highly varying contrast. Because of the complicated electrical profile of the brain, a realistic model is desired. Models of 16 human heads produced by MRI and segmented into surfaces for each distinct material have been developed [149]. The materials consist of skin, skull, Cerebral spinal fluid (CSF), Cerebellum, ventricles, grey matter, white matter. The permittivities for the materials is obtained from a library of human tissues [150]. Firstly the surface models are converted to a voxelized model based on a voxel size of 0.5 mm. To simulate a ICH stroke a sphere of blood with a linearly increasing radius is introduced at a random location. The materials of the region are replaced by blood when the stroke reaches that point. The visualization of this is shown in Fig. 7.2 where Fig. 7.2(a) shows the model at a point in time and Fig. 7.2(b) shows the model at a point farther along in time. The simulation setup consists of a circular aperture with 36 transceivers in a plane placed approximately at the midpoint of the brain matter in the z-axis. A full wave time domain simulation is conducted 30 times as the haemorrhagic

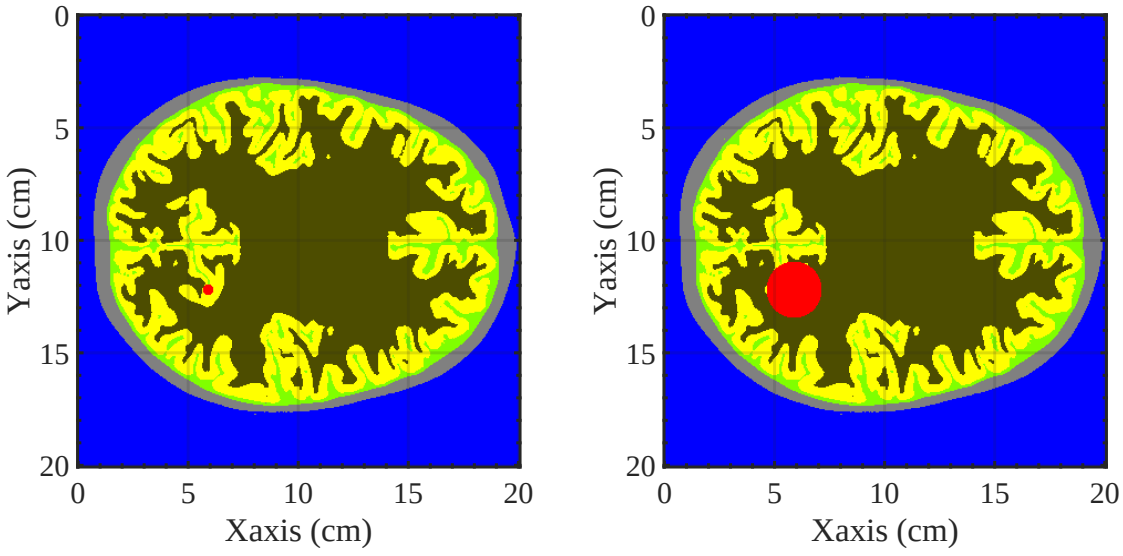

Figure 7.2: Brief image showing the different regions of the model. (a) Early model, (b) later model where the stroke has grown in size.

stroke progresses in volume.

7.3 Simulation Results

The reconstructed image can be obtained using the received data, and the global back projection algorithm [151]. However, due to the highly contrasting dielectric values, in order to image with minimal distortion, the variable group velocity technique should be used [4]. Using the variable group velocity method we obtain the image presented in Fig. 7.3(a). As the aperture was setup as a circular aperture, and the shape of the skull is elliptical, the front and back portions of the skull show up very strongly. This can be mitigated in this situation by choosing an aperture that aligns with the shape of the skull. However, for a general purpose solution, the technique will need to be used on skulls with a variety of shapes.

The stroke region is not initially apparent in the reconstructed image shown in Fig. 7.3(a). Additionally, high quality details of the brain such as those that are visible in an MRI or CT scan are not clear. This is due to the lower resolution of the microwave scanning. To perform stroke classification, despite the shortcomings of microwave imaging different techniques are

required.

The first step is to perform a differential analysis over time. This consists simply of a subtraction at each aperture location with the results of the previous data. This could be altered to be a subtraction with respect to a point in time farther ago in time. It could also be with respect to a floating average of several points in time. These changes will depend on the sampling frequency of the final setup with respect the speeds of the stroke progression.

Once the differential analysis is performed, in the case of simulation, the effect of the stroke is clearly visible, this is shown in Fig. 7.3(b), this figure is a plot of a single aperture location over time. The plot corresponds to a probe situated in the bottom left hand quadrant with reference to Fig. 7.2(b). In the plot in the region of 2-3ns we can see the effect of the near side of the stroke region. In the region where time is greater than 3 ns we can see the reflection of the far side of the stroke region. The far side is stronger due to a focusing effect present in full wave simulations when perfect circles are used as scatterers. In order to increase the effect of the transient effects on the final image a cross correlation function is employed. The function consists of first deciding on an array of speeds to examine the data for. At a specific point in slow time N and for each aperture location, the function takes in the data $N-5:N+5$ for that aperture location and applies a shifted cross correlation for each speed under analysis. In this way a 3D dataset is created. With the axis being the aperture, the fast time axis, and the speeds under analysis.

$$C(m,n,v_{op}) = \Sigma_{i=m_c-5}^{m_c+5} D(m, n-(m-i)\frac{2t_{prf}v_{op}}{v_g d_t}) \tag{7.1}$$

where D is the measured data, m is the aperture location, n is fast time, v is the speed, t_{prf} is the period of the pulse repetition frequency at that aperture location, v_{op} speed of interest, v_g is the group velocity in the target scene, d_t is the time step of the fast time axis. The output C is a matrix which tells us for each aperture location, for each speed of interest, what is chance that any scatterers are traveling at that speed.

From this data, each speed can be checked to see how strongly the correlation is at that

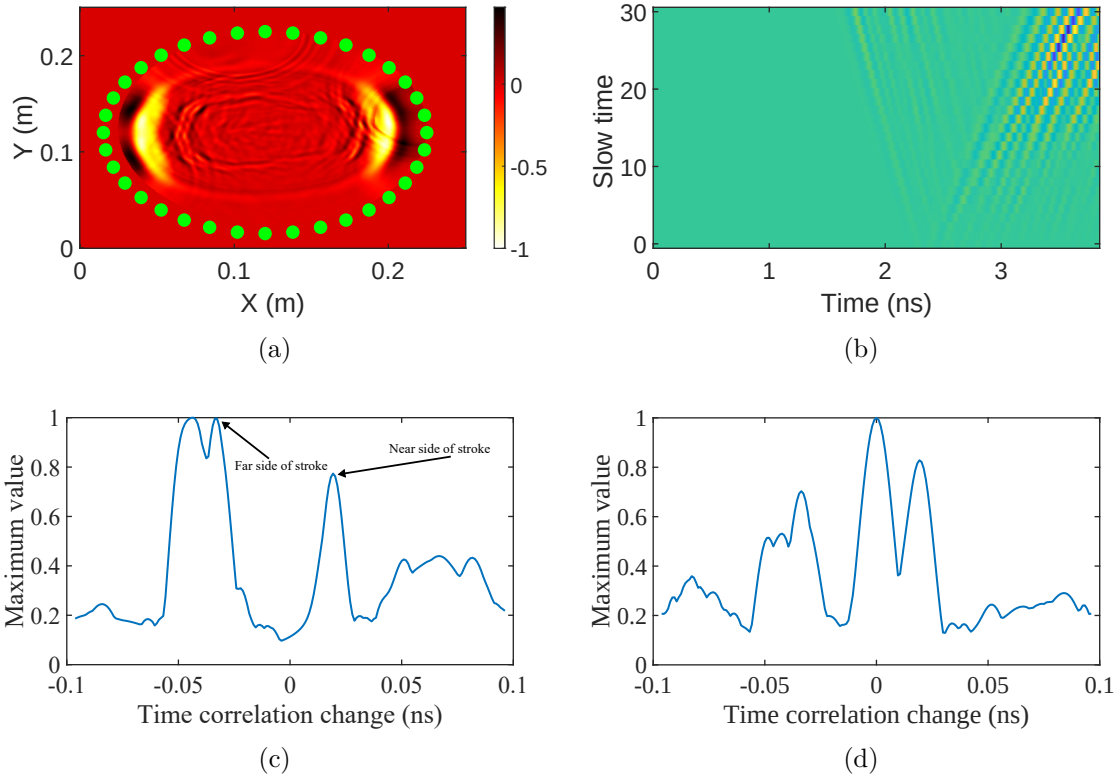

Figure 7.3: (a) Reconstructed image using variable group velocity method. (b) Slow time. (c) Plot of maximum value at different speeds for differential. (d) Plot of maximal value at speeds shifts for non differential.

speed, which indicates the amount of transient behaviour at that speed. To quickly validate this technique, we can plot an example of the the 3D dataset. For each speed of interest we take the maxima for that speed. This result is shown in Fig. 7.3(c). This figure shows two large peaks which correspond to the expanding front of the stroke and the receding far side of the stroke with respect to the probe location. Naturally, high quality data is expected as a differential treatment in a simulation will perfectly remove non-transient effects. However, if we apply the same function to the non-differential data we can see a similar graph as shown in Fig.7.3(d) which is created in the exact same way for the original data to Fig. 7.3(c). The Fig.7.3(d) shows that both transient effects are clearly visible with the addition of significant correlation at 0 transient change as expected from a non-differential dataset. Although modified for this situation, the processing closely follows the same basic algorithm which is used in ultrasound imaging [152]. This example clearly demonstrates that this

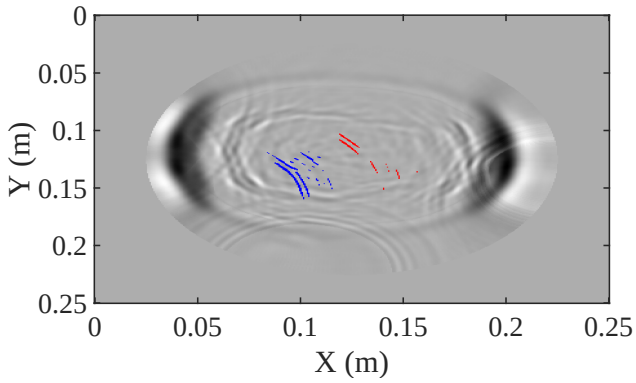

Figure 7.4: Grayscale reconstructed image with a superimposed doppler image.

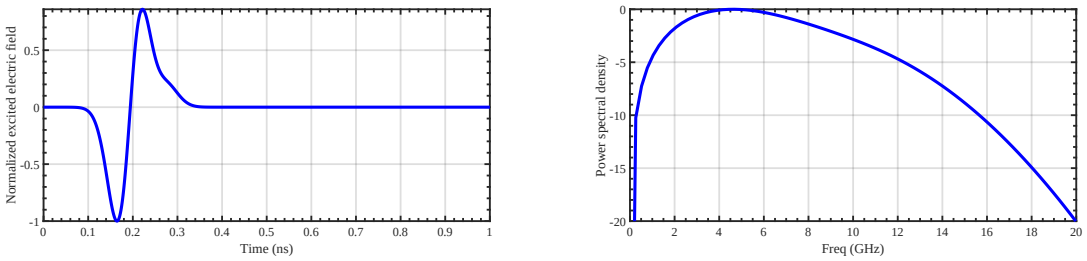

(a) (b)

Figure 7.5: Plots of the details of the excitation pulse. (a) Time domain pulse. (b) Plot of power spectral density.

technique can be used to find differential effects that are not otherwise visible due to much larger reflections from stationary scatterers.

In order to add localization to this technique, the data can be thresholded and the data can be projected into the spatial domain using the global back projection algorithm. Using a judicious threshold, the data generated by moving scatteres can be produced and overlayed on the original reconstructed data and is shown in Fig. 7.3. As the reflections from the stroke are very weak and very delayed due to the high permittivity of the head, only transceivers on the bottom left quadrant are even able to receive these signals. For this reason, there is limited ability to properly focus the energy as the array has a small angle of integration. However, the data is projected to the correct location and can give a viewer of the image an idea of where the stroke is occurring.

7.4 Conclusion

This chapter motivates using microwave imaging in stroke scanning and classification. An algorithm, which is inspired from ultrasound imaging is created and tailored for microwave imaging. This algorithm demonstrates in simulation that stationary clutter suppression can be achieved and stroke classification and localization can be achieved despite challenges in the microwave space for stroke imaging.

Chapter 8

Conclusion and Future Work

8.1 Conclusion

This thesis aims to improve the ability of time domain UWB radar imaging to detect objects that are either low contrast or low RCS relative to the rest of the target scene. To this end, the conventional SAR-based UWB imaging techniques are analyzed and scrutinized. Several issues with the current techniques are identified. Firstly, image reconstruction algorithms require knowledge of the group velocity in the target scene, and the group velocity is expected to be uniform. Next, the placement of the aperture can significantly affect the reconstructed image. Thirdly, multiple reflections and more significant scatterers can drown out smaller scatterers making them hard to identify in certain imaging applications.

Based on these three issues, this thesis proposes several techniques which can be used to mitigate or overcome these issues. Two techniques are proposed to mitigate the uniform group velocity issue in the target scene. One technique provides a method to theoretically characterize simple antennas as well as a manner to characterize transceivers experimentally. It is also demonstrated how the characterization can be easily integrated into image reconstruction algorithms, resulting in higher image quality and successful mitigation of the disturbance in the uniform group velocity caused by imaging in the near field of the antenna.

This technique was shown in Chapter 2. The second technique provides a method to mitigate issues when imaging in regions with regions of variable group velocity. This technique exploits circular symmetry to segment the target scene and apply varying group velocities to different regions, thus mitigating the restriction on uniform group velocity in this situation. This technique facilitates the use of microwave imaging in regions with highly varying group velocities, which, without this technique, will result in highly distorted regions which previously would have limited microwave imaging in those applications. The second technique related to uniform velocity in imaging is detailed in Chapter 5.

The second main issue that this thesis highlights in microwave imaging is the issue with the aperture, and the issues restrictions of the aperture can cause. The technique proposed in Chapter 4 can mitigate the impact of the restrictions on the aperture on microwave imaging. It does this by creating a model of the major scatterers in the spatial domain and creating new data based on that model, which can be used to mitigate missing aperture locations.

The final group of techniques demonstrated in this thesis are the techniques that directly work to improve the imaging of low-contrast targets in specific applications. The thesis proposes two techniques that can image in situations where due to low contrast and low RCS, objects would normally be invisible to radar. However, in specific situations, the targets can still be found. The first situation is where the targets exhibit non-linear behaviour; the second is where the target is moving. These two techniques were shown in Chapter 6 and Chapter 7, respectively. Finally, a framework for designing time domain antennas for microwave imaging was shown in Chapter 3. This chapter demonstrated the importance of designing antennas with the time domain behaviour in mind and the resulting impact this will have on the images created. This impact comes in several ways. First, we can design antennas that will have a limited near field, which will improve and simplify imaging in the near field. Additionally, reduced ringing will result in a better SNR and higher-quality reconstructed images.

These proposed techniques all serve to improve the reconstructed images. The improved images, either with reduced background noise, reduced clutter, or with reduced distortion,

can all serve to improve the likelihood that low RCS and low contrast targets can be found.

8.2 Future Directions

Of the proposed techniques, several are ready to implement in current microwave imaging applications. Near field mitigation techniques proposed in Chapter 2 have been demonstrated to be effective and can easily be implemented in situations that require near field imaging. Currently, this technique is only demonstrated in two dimensions. In the future, the demonstration of this technique could be extended to three dimensions.

In terms of the topics presented in Chapter 3, this chapter presented important evidence that designing with the time domain in mind is important for antennas that intend to be used in the time domain. There are many future directions for this topic. One concept is at the nexus of time domain antenna design and near field imaging. The idea is to design practical transmitters which can reduce the near field or else produce a near field that is designed to be easily quantifiable in some manner. Theoretical work has already been done by others in this direction [153]. Antennas with improved near field characteristics could further improve the quality of near field imaging. Additionally, designing a pulse shape such that reduced ringing would occur at the output of the antenna is also a future direction with significant applications.

The Virtual Aperture project, presented in Chapter 4, first presented a method to detect the major scatterers in the target scene and use the model of the major scatterers to augment the aperture virtually. It demonstrated that this technique reduced artifacts and increased the readability of the image as well as decreasing the distortion of the major scatterers in the reconstructed image. However, this technique added more data from the large detected objects in order to correct their shape in the reconstructed image. This meant that for small targets that were not detected by the object detection algorithm, adding data might actually decrease the likelihood that they would be visible in the final image. As a potential future research in this direction, a new algorithm could be created to attempt to intelligently remove the received data from large detected objects instead of augmenting it. Potentially

this would increase the ability to view objects with lower RCS as the image would not be dominated by the large reflectors.

Chapter 5 presented a new technique to mitigate image distortion caused by regions in the target scene having highly varying group velocities. This technique demonstrated increased image quality and can be currently applied to any imaging situation where there there is some circular symmetry in the target scene. This technique could also be applied to LSAR applications, and the demonstration of such an application could be a future direction of this work. There are also several techniques that allow prediction of the group velocity of a specific region [129]. Another future direction of this work could be to integrate the prediction of the group velocities in the different regions directly in the image reconstruction.

The novel technique presented in Chapter 6, that being the time domain technique to detect non-linear targets. This technique showed some promise and theoretically has lots of potential; however, to pursue this topic, further limitations in the hardware need to be solved. To perform the experiments shown in Chapter 6, the transmitting Vivaldi antenna was rotated by hand to produce the inverted pulses. This added significant noise to the experiment as it was difficult to ensure exactly a 180° rotation, and slight disturbances in the orientation of the antenna were unavoidable when moving by hand. As the clutter suppression relied on the alignment of the pulses in order to subtract the linear components, slight misalignment resulted in significant contributions to the noise of the experiment. A hardware solution is required to overcome this. If a pulse generator system can be designed this would allow this non-linear work to be extended closer to real world applications.

Finally, in Chapter 7, a new technique for stationary clutter suppression was proposed. Future work in this direction would consist of additional full-wave simulations and creating rigorous techniques to classify ischemic and hemorrhagic strokes need to be created. Should these additional testing prove successful, the next step is to create systems capable of clinical monitoring in order to move closer to clinical testing.

References

[1] S. Gogineni, J.-B. Yan, D. Gomez-Garcia, *et al.*, "Ultra-wideband radars for measurements over ice and snow," in *2015 IEEE International Geoscience and Remote Sensing Symposium (IGARSS)*, 2015, pp. 4204–4207. DOI: 10.1109/IGARSS.2015.7326753.

[2] D. O. Batrakov, M. S. Antyufeyeva, A. V. Antyufeyev, and A. G. Batrakova, "Remote sensing of plane-layered media with losses using uwb signals," in *2017 XI International Conference on Antenna Theory and Techniques (ICATT)*, 2017, pp. 370–373. DOI: 10.1109/ICATT.2017.7972666.

[3] X. Wang, A. Dinh, and D. Teng, "Low-power low-complexity carrier-based uwb transmitter in 90nm cmos for wireless biomedical radar sensing applications," in *Proceedings of 2010 IEEE International Symposium on Circuits and Systems*, 2010, pp. 3477–3480. DOI: 10.1109/ISCAS.2010.5537845.

[4] D. Oloumi, R. S. C. Winter, A. Kordzadeh, P. Boulanger, and K. Rambabu, "Microwave imaging of breast tumor using time-domain uwb circular-sar technique," *IEEE Transactions on Medical Imaging*, vol. 39, no. 4, pp. 934–943, 2020. DOI: 10.1109/TMI.2019.2937762.

[5] B. Zhou, W. Shao, and G. Wang, "On the resolution of uwb microwave imaging of tumors in random breast tissue," in *2005 IEEE Antennas and Propagation Society International Symposium*, vol. 3A, 2005, 831–834 vol. 3A. DOI: 10.1109/APS.2005.1552386.

[6] J. D. Garrett and E. C. Fear, "Average property estimation validation with realistic breast models," in *The 8th European Conference on Antennas and Propagation (EuCAP 2014)*, 2014, pp. 1279–1280. DOI: 10.1109/EuCAP.2014.6902009.

[7] M. Jalilvand, X. Li, and T. Zwick, "A model approach to the analytical analysis of stroke detection using uwb radar," in *2013 7th European Conference on Antennas and Propagation (EuCAP)*, 2013, pp. 1555–1559.

[8] M. Baboli, A. Sharafi, A. Ahmadian, and M. Nambakhsh, "An accurate and robust algorithm for detection of heart and respiration rates using an impulse based uwb signal," in *2009 International Conference on Biomedical and Pharmaceutical Engineering*, 2009, pp. 1–4. DOI: 10.1109/ICBPE.2009.5384092.

[9] K. K.-M. Chan, A. E.-C. Tan, and K. Rambabu, "Circularly polarized ultra-wideband radar system for vital signs monitoring," *IEEE Transactions on Microwave Theory and Techniques*, vol. 61, no. 5, pp. 2069–2075, 2013. DOI: 10.1109/TMTT.2013.2253328.

[10] M. Naveena, D. K. Singh, and H. Singh, "Design of uhf band uwb antenna for foliage penetration application," in *2017 IEEE International Conference on Antenna Innovations Modern Technologies for Ground, Aircraft and Satellite Applications (iAIM)*, 2017, pp. 1–3. DOI: 10.1109/IAIM.2017.8402555.

[11] D. Oloumi, K. K.-M. Chan, P. Boulanger, and K. Rambabu, "Sagd process monitoring in heavy oil reservoir using uwb radar techniques," *IEEE Transactions on Microwave Theory and Techniques*, vol. 64, no. 6, pp. 1884–1895, 2016. DOI: 10.1109/TMTT.2016.2561926.

[12] F. Zhenhe, Z. Jun, and W. Yi, "The hal-3 airborne navigation radar," *IEEE Transactions on Aerospace and Electronic Systems*, vol. 32, no. 3, pp. 1208–1211, 1996. DOI: 10.1109/7.532286.

[13] M. Yeary, B. L. Cheong, J. M. Kurdzo, T.-y. Yu, and R. Palmer, "A brief overview of weather radar technologies and instrumentation," *IEEE Instrumentation Measurement Magazine*, vol. 17, no. 5, pp. 10–15, 2014. DOI: 10.1109/MIM.2014.6912194.

[14] R. Feghhi, R. S. C. Winter, and K. Rambabu, "Design of a low-cost uwb time-domain radar system for sub-centimeter image resolution," *IEEE Transactions on Microwave Theory and Techniques*, vol. 39, no. 4, pp. 934–943, 2022. DOI: 10.1109/TMI.2019.2937762.

[15] K. K. Chan, A. E. Tan, and K. Rambabu, "Decade bandwidth circularly polarized antenna array," *IEEE Trans. Antennas Propag.*, vol. 61, no. 11, pp. 5435–5443, Nov. 2013. DOI: 10.1109/TAP.2013.2276923.

[16] D. Oloumi and K. Rambabu, "Studying the superluminal behavior of uwb antennas and its effect on near-field imaging," *IEEE Trans. Antennas Propag.*, vol. 64, no. 12, pp. 5084–5093, Dec. 2016, ISSN: 0018-926X. DOI: 10.1109/TAP.2016.2620524.

[17] M. Kanda, "Time domain sensors for radiated impulsive measurements," *IEEE Transactions on Antennas and Propagation*, vol. 31, no. 3, pp. 438–444, May 1983, ISSN: 0018-926X. DOI: 10.1109/TAP.1983.1143057.

[18] K. Rambabu, A. E. .-. Tan, K. K. .-. Chan, and M. Y. .-. Chia, "Estimation of antenna effect on ultra-wideband pulse shape in transmission and reception," *IEEE Transactions on Electromagnetic Compatibility*, vol. 51, no. 3, pp. 604–610, Aug. 2009.

[19] X. Qing, Z. N. Chen, and M. Y. W. Chia, "Characterization of ultrawideband antennas using transfer functions," *Radio science*, vol. 41, no. 01, pp. 1–10, 2006.

[20] A. E. C. Tan, M. Y. W. Chia, K. K. M. Chan, and K. Rambabu, "Modeling the transient radiated and received pulses of ultra-wideband antennas," *IEEE Trans. Antennas Propag.*, vol. 61, no. 1, pp. 338–345, Jan. 2013, ISSN: 0018-926X. DOI: 10.1109/TAP.2012.2215293.

[21] N. Ghavami, G. Tiberi, D. J. Edwards, and A. Monorchio, "Uwb microwave imaging of objects with canonical shape," *IEEE Trans. Antennas Propag.*, vol. 60, no. 1, pp. 231–239, 2011.

[22] Y. Zou, X. Gao, X. Li, and Y. Liu, "A high precision gtd parameter estimation method," in *2015 8th Int. Congr. on Image and Signal Processing (CISP)*, Oct. 2015, pp. 1220–1224. DOI: 10.1109/CISP.2015.7408067.

[23] A. Pimpatang, T. Lertwiriyaprapa, and C. Pongcharoenpanich, "Heuristic utd corner and slope diffractions for antenna problem," in *2017 Int. Symp. on Antennas and Propagation (ISAP)*, Oct. 2017, pp. 1–2. DOI: 10.1109/ISANP.2017.8228981.

[24] J. Kiriazi, J. Nakakura, K. Hall, N. Hafner, and V. Lubecke, "Low profile harmonic radar transponder for tracking small endangered species," in *2007 29th Annual International Conference of the IEEE Engineering in Medicine and Biology Society*, IEEE, 2007, pp. 2338–2341.

[25] Z.-M. Tsai, P.-H. Jau, N.-C. Kuo, *et al.*, "A high-range-accuracy and high-sensitivity harmonic radar using pulse pseudorandom code for bee searching," *IEEE Transactions on Microwave Theory and Techniques*, vol. 61, no. 1, pp. 666–675, 2012.

[26] J. Riley, A. Smith, D. Reynolds, *et al.*, "Tracking bees with harmonic radar," *Nature*, vol. 379, no. 6560, pp. 29–30, 1996.

[27] G. J. Mazzaro, A. F. Martone, K. I. Ranney, and R. M. Narayanan, "Nonlinear radar for finding rf electronics: System design and recent advancements," *IEEE Transactions on Microwave Theory and Techniques*, vol. 65, no. 5, pp. 1716–1726, 2017.

[28] D. W. P. Thomas, M. H. Baharuddin, C. Smartt, G. Gradoni, G. Tanner, and S. Creagh, "Reducing the complexity of near-field scanning of stochastic fields," in *2017 13th Int. Conf. on Advanced Technologies, Systems and Services in Telecommunications (TELSIKS)*, Oct. 2017, pp. 11–14. DOI: 10.1109/TELSKS.2017.8246218.

[29] J. Fortuny-Guasch, "A novel 3-d subsurface radar imaging technique," *IEEE Trans. Geosci. Remote Sens.*, vol. 40, no. 2, pp. 443–452, Feb. 2002. DOI: 10.1109/36.992808.

[30] S. M. Mikki and Y. M. M. Antar, "A theory of antenna electromagnetic near field—part I," *IEEE Trans. Antennas Propag.*, vol. 59, no. 12, pp. 4691–4705, 2011.

[31] S. M. Mikki and Y. M. M. Antar, "A theory of antenna electromagnetic near field—part II," *IEEE Trans. Antennas Propag.*, vol. 59, no. 12, pp. 4706–4724, 2011.

[32] C. F. Curtis and E. C. Fear, "Near field radar imaging in the frequency domain with application to patient data," in *2015 USNC-URSI Radio Science Meeting (Joint with AP-S Symp.)*, Jul. 2015, pp. 306–306. DOI: 10.1109/USNC-URSI.2015.7303590.

[33] D. Oloumi, P. Boulanger, A. Kordzadeh, and K. Rambabu, "Breast tumor detection using uwb circular-sar tomographic microwave imaging," in *2015 37th Annu. Int. Conf. of the IEEE Engineering in Medicine and Biology Society (EMBC)*, Aug. 2015, pp. 7063–7066. DOI: 10.1109/EMBC.2015.7320019.

[34] M. Jalilvand, X. Li, L. Zwirello, and T. Zwick, "Ultra wideband compact near-field imaging system for breast cancer detection," *IET Microwaves, Antennas Propagation*, vol. 9, no. 10, pp. 1009–1014, 2015, ISSN: 1751-8725. DOI: 10.1049/iet-map.2014.0735.

[35] X. Li, M. Jalilvand, L. Zwirello, and T. Zwick, "Array configurations of a uwb near field imaging system for the detection of water accumulation in human body," in *2011 8th European Radar Conf.*, Oct. 2011, pp. 170–173.

[36] M. S. Ali, N. J. Shoumy, S. Khatun, L. M. Kamarudin, and V. Vijayasarveswari, "Non-invasive blood glucose measurement performance analysis through uwb imaging," in *2016 3rd Int. Conf. on Electronic Design (ICED)*, Aug. 2016, pp. 513–516. DOI: 10.1109/ICED.2016.7804698.

[37] S. Adnan, A. F. Mirza, R. A. Abd-Alhameed, *et al.*, "Microwave antennas for near field imaging," in *2014 IEEE MTT-S Int. Microwave Workshop Series on RF and Wireless Technologies for Biomedical and Healthcare Applications (IMWS-Bio2014)*, Dec. 2014, pp. 1–3. DOI: 10.1109/IMWS-BIO.2014.7032405.

[38] S. Di Meo, P. F. Espín-López, A. Martellosio, *et al.*, "On the feasibility of breast cancer imaging systems at millimeter-waves frequencies," *IEEE Trans. Microw. Theory Techn.*, vol. 65, no. 5, pp. 1795–1806, 2017.

[39] M. V. Prati, J. Moll, C. Kexel, *et al.*, "Breast cancer imaging using a 24 ghz ultra-wideband mimo fmcw radar: System considerations and first imaging results," in *2020 14th European Conf. on Antennas and Propagation (EuCAP)*, 2020, pp. 1–5.

[40] H. Yang, T. Li, N. Li, Z. He, and Q. H. Liu, "Efficient near-field imaging for single-borehole radar with widely separated transceivers," *IEEE Trans. Geosci. Remote Sens.*, vol. 53, no. 10, pp. 5327–5337, Oct. 2015, ISSN: 0196-2892. DOI: 10.1109/TGRS.2015.2421478.

[41] S. S. Fayazi, J. Yang, and H. S. Lui, "Uwb sar imaging of near-field object for industrial process applications," in *2013 7th European Conf. on Antennas and Propagation (EuCAP)*, Apr. 2013, pp. 2245–2248.

[42] S. S. Fayazi, H. S. Lui, and J. Yang, "Microwave imaging of near-field object using ultra-wideband synthetic aperture radar algorithm," in *Proc. of the 2012 IEEE Int. Symp. on Antennas and Propagation*, Jul. 2012, pp. 1–2. DOI: 10.1109/APS.2012.6348657.

[43] K. Rambabu, A. E. C. Tan, K. K. M. Chan, and M. Y. W. Chia, "Estimation of antenna effect on ultra-wideband pulse shape in transmission and reception," *IEEE Transactions on Electromagnetic Compatibility*, vol. 51, no. 3, pp. 604–610, Aug. 2009, ISSN: 0018-9375. DOI: 10.1109/TEMC.2009.2023364.

[44] A. T. Mobashsher and A. M. Abbosh, "Near-field time-domain characterisation of wideband antennas," *Electronics Letters*, vol. 51, no. 25, pp. 2076–2078, 2015, ISSN: 0013-5194. DOI: 10.1049/el.2015.2763.

[45] A. Shlivinski, E. Heyman, and R. Kastner, "Antenna characterization in the time domain," *IEEE Trans. Antennas Propag.*, vol. 45, no. 7, pp. 1140–1149, Jul. 1997, ISSN: 0018-926X. DOI: 10.1109/8.596907.

[46] D. Ghosh, A. De, M. C. Taylor, T. K. Sarkar, M. C. Wicks, and E. L. Mokole, "Transmission and reception by ultra-wideband (uwb) antennas," *IEEE Antennas and Propagation Magazine*, vol. 48, no. 5, pp. 67–99, Oct. 2006, ISSN: 1045-9243. DOI: 10.1109/MAP.2006.277157.

[47] M. A. Almoteriy, M. I. Sobhy, and J. C. Batchelor, "Antenna characterisation and channel effects on digital systems," in *Loughborough Antennas Propagation Conf. (LAPC 2017)*, Nov. 2017, pp. 1–5. DOI: 10.1049/cp.2017.0258.

[48] W. Wiesbeck, G. Adamiuk, and C. Sturm, "Basic properties and design principles of uwb antennas," *Proc. of the IEEE*, vol. 97, no. 2, pp. 372–385, Feb. 2009, ISSN: 0018-9219. DOI: 10.1109/JPROC.2008.2008838.

[49] K. K. M. Chan, D. Oloumi, P. Boulanger, and K. Rambabu, "Uwb antenna design for dispersion free time synchronized pulse radiation," *IEEE Trans. Antennas Propag.*, vol. 65, no. 12, pp. 6819–6826, Dec. 2017, ISSN: 0018-926X. DOI: 10.1109/TAP.2017.2757965.

[50] R. L. Smith, "The velocities of light," *American Journal of Physics*, vol. 38, no. 8, pp. 978–984, 1970.

[51] J. C.-E. Sten and A. Hujanen, "Aspects on the phase delay and phase velocity in the electromagnetic near-field," *Progress In Electromagnetics Research*, vol. 56, pp. 67–80, 2006.

[52] D. Oloumi, "Ultra-wideband synthetic aperture radar imaging: Theory and applications," Ph.D. dissertation, University of Alberta, Jul. 2016.

[53] L. J. Wang, A. Kuzmich, and A. Dogariu, "Gain-assisted superluminal light propagation," *Nature*, vol. 406, pp. 277–279, Jul. 2000. [Online]. Available: http://dx.doi.org/10.1038/35018520.

[54] D. Mugnai, A. Ranfagni, and L. Ronchi, "The question of tunneling time duration: A new experimental test at microwave scale," *Physics Letters A*, vol. 247, no. 4, pp. 281–286, 1998, ISSN: 0375-9601. DOI: https://doi.org/10.1016/S0375-9601(98)00628-8. [Online]. Available: http://www.sciencedirect.com/science/article/pii/S0375960198006288.

[55] J. Lloyd, K. Wang, A. Barkan, and D. M. Mittleman, "Characterization of apparent superluminal effects in the focus of an axicon lens using terahertz time-domain spectroscopy," *Optics Communications*, vol. 219, no. 1, pp. 289–294, 2003, ISSN: 0030-4018. DOI: https://doi.org/10.1016/S0030-4018(03)01311-7. [Online]. Available: http://www.sciencedirect.com/science/article/pii/S0030401803013117.

[56] I. Ahmed, *Study of the local backprojection algorithm for image formation in ultra wideband synthetic aperture radar*, 2008.

[57] D. Oloumi, J. W. Ting, and K. Rambabu, "Design of pulse characteristics for near-field uwb-sar imaging," *IEEE Trans. Microw. Theory Techn.*, vol. 64, no. 8, pp. 2684–2693, Aug. 2016, ISSN: 0018-9480. DOI: 10.1109/TMTT.2016.2585484.

[58] D. Oloumi and K. Rambabu, "Metal-cased oil well inspection using near-field uwb radar imaging," *IEEE Trans. Geosci. Remote Sens.*, vol. 56, pp. 5884–5892, Oct. 2018, ISSN: 0196-2892. DOI: 10.1109/TGRS.2018.2827395.

[59] D. Oloumi, M. I. Pettersson, P. Mousavi, and K. Rambabu, "Imaging of oil-well perforations using uwb synthetic aperture radar," *IEEE Trans. Geosci. Remote Sens.*, vol. 53, no. 8, pp. 4510–4520, Aug. 2015, ISSN: 0196-2892. DOI: 10.1109/TGRS.2015.2400918.

[60] R. S. C. Winter, D. Oloumi, and K. Rambabu, "Uwb sensor characterization for radar sensing and imaging in superluminal propagation regions," *IEEE Transactions on Microwave Theory and Techniques*, vol. 69, no. 1, pp. 297–307, 2021. DOI: 10.1109/TMTT.2020.3023095.

[61] H. A. Kiani, C. B. Ali, S. J. A. Shah, M. Z. Khan, A. Noorwali, and S. A. Shah, "Performance enhancement and size reduction of vivaldi antenna using defected ground structure for active phased array radar applications," in *2021 International Congress of Advanced Technology and Engineering (ICOTEN)*, IEEE, 2021, pp. 1–5.

[62] A. Kuriakose, T. A. George, and S. Anand, "Improved high gain vivaldi antenna design for through-wall radar applications," in *2020 International Symposium on Antennas & Propagation (APSYM)*, IEEE, 2020, pp. 58–61.

[63] A. O. Asok and S. Dey, "Novel uwb antipodal antenna with paddle shaped stubs and frustum shaped dielectric loading for microwave imaging applications," in *2020 IEEE Asia-Pacific Microwave Conference (APMC)*, IEEE, 2020, pp. 1060–1062.

[64] K. Kikuta and A. Hirose, "Compact folded-fin tapered slot antenna for uwb applications," *IEEE Antennas and Wireless Propagation Letters*, vol. 14, pp. 1192–1195, 2015.

[65] E. C. Fear, X. Li, S. C. Hagness, and M. A. Stuchly, "Confocal microwave imaging for breast cancer detection: Localization of tumors in three dimensions," *IEEE Transactions on Biomedical Engineering*, vol. 49, no. 8, pp. 812–822, 2002.

[66] R. Wang, Y. Sun, and J.-C. Scheytt, "An on-board differential bunny-ear antenna design for 60 ghz applications," in *German Microwave Conference Digest of Papers*, IEEE, 2010, pp. 9–12.

[67] D. Schaubert, E. Kollberg, T. Korzeniowski, T. Thungren, J. Johansson, and K. Yngvesson, "Endfire tapered slot antennas on dielectric substrates," *IEEE Transactions on antennas and propagation*, vol. 33, no. 12, pp. 1392–1400, 1985.

[68] H. Kähkönen, J. Ala-Laurinaho, and V. Viikari, "Dual-polarized ka-band vivaldi antenna array," *IEEE Transactions on Antennas and Propagation*, vol. 68, no. 4, pp. 2675–2683, 2019.

[69] A. S. Dixit and S. Kumar, "A miniaturized antipodal vivaldi antenna for 5g communication applications," in *2020 7th International Conference on Signal Processing and Integrated Networks (SPIN)*, IEEE, 2020, pp. 800–803.

[70] R. Natarajan, J. V. George, M. Kanagasabai, *et al.*, "Modified antipodal vivaldi antenna for ultra-wideband communications," *IET Microwaves, Antennas & Propagation*, vol. 10, no. 4, pp. 401–405, 2016.

[71] D. Oloumi, "Oil Well Monitoring by Ultra-wideband Ground Penetrating Synthetic Aperture Radar," M.S. thesis, Blekinge Institute of Technology, Karlskrona, Sweden, 2012.

[72] L. Zhang, S. Gao, Q. Luo, *et al.*, "Single-feed ultra-wideband circularly polarized antenna with enhanced front-to-back ratio," *IEEE Transactions on Antennas and Propagation*, vol. 64, no. 1, pp. 355–360, 2015.

[73] G. Teni, N. Zhang, J. Qiu, and P. Zhang, "Research on a novel miniaturized antipodal vivaldi antenna with improved radiation," *IEEE Antennas and wireless propagation letters*, vol. 12, pp. 417–420, 2013.

[74] R. Feghhi, D. Oloumi, and K. Rambabu, "Tunable subnanosecond gaussian pulse radar transmitter: Theory and analysis," *IEEE Transactions on Microwave Theory and Techniques*, vol. 68, no. 9, pp. 3823–3833, 2020. DOI: 10.1109/TMTT.2020.2983161.

[75] J. Ao, J. Huang, W. Wu, and N. Yuan, "A miniaturized vivaldi antenna by loading with parasitic patch and lumped resistor," *AEU-International Journal of Electronics and Communications*, vol. 81, pp. 158–162, 2017.

[76] G. Kumar Pandey and M. Kumar Meshram, "A printed high gain uwb vivaldi antenna design using tapered corrugation and grating elements," *International Journal of RF and Microwave Computer-Aided Engineering*, vol. 25, no. 7, pp. 610–618, 2015.

[77] S. Zhu, H. Liu, and P. Wen, "A new method for achieving miniaturization and gain enhancement of vivaldi antenna array based on anisotropic metasurface," *IEEE Transactions on Antennas and Propagation*, vol. 67, no. 3, pp. 1952–1956, 2019.

[78] F. Jolani, G. R. Dadashzadeh, M. Naser-Moghadasi, and A. Dadgarpour, "Design and optimization of compact balanced antipodal vivaldi antenna," *Progress In Electromagnetics Research C*, vol. 9, pp. 183–192, 2009.

[79] C. Zhang, M. Kuhn, M. Mahfouz, and A. E. Fathy, "Planar antipodal vivaldi antenna array configuration for low cross-polarization and reduced mutual coupling performance," in *2007 IEEE Antennas and Propagation Society International Symposium*, IEEE, 2007, pp. 725–728.

[80] X. Qing, Z. N. Chen, and M. Y. W. Chia, "Dual elliptically tapered antipodal slot antenna loaded by curved terminations for ultrawideband applications," *Radio Science*, vol. 41, no. 06, pp. 1–14, Dec. 2006. DOI: 10.1029/2006RS003497.

[81] P. Fei, Y.-C. Jiao, W. Hu, and F.-S. Zhang, "A miniaturized antipodal vivaldi antenna with improved radiation characteristics," *IEEE Antennas and Wireless Propagation Letters*, vol. 10, pp. 127–130, 2011, ISSN: 1536-1225. DOI: 10.1109/LAWP.2011.2112329.

[82] A. Kumar, A. Sarma, E. Ansari, and K. Yedukondalu, "Improved phase center estimation for gnss patch antenna," *IEEE transactions on Antennas and Propagation*, vol. 61, no. 4, pp. 1909–1915, 2013.

[83] Y. Hu, "A method of determining phase centers and its application to electromagnetic horns," *Journal of the Franklin Institute*, vol. 271, no. 1, pp. 31–39, 1961.

[84] G. Sun, F. Zhang, S. Pan, and X. Ye, "Frequency-domain versus time-domain imaging for photonics-based broadband radar," *Electronics Letters*, vol. 56, no. 24, pp. 1330–1332, 2020.

[85] X. Zhuge, T. Savelyev, A. Yarovoy, L. Ligthart, and B. Levitas, "Comparison of different migration techniques for uwb short-range imaging," in *2009 European Radar Conference (EuRAD)*, 2009, pp. 184–187.

[86] J. T. Case, M. T. Ghasr, and R. Zoughi, "Optimum 2-d nonuniform spatial sampling for microwave sar-based nde imaging systems," *IEEE Transactions on Instrumentation and Measurement*, vol. 61, no. 11, pp. 3072–3083, 2012.

[87] J. Salzman, D. Akamine, R. Lefevre, and J. C. Kirk, "Interrupted synthetic aperture radar (sar)," *IEEE aerospace and electronic systems magazine*, vol. 17, no. 5, pp. 33–39, 2002.

[88] G. Coskuner and H. Huang, "Enhanced oil recovery in post-chops cold heavy oil production with sand heavy oil reservoirs of alberta and saskatchewan part 2: Field piloting of cycling solvent injection," in *SPE Canada Heavy Oil Conference*, OnePetro, 2020.

[89] D. Oloumi, *Oil well monitoring by ultra-wideband ground penetrating synthetic aperture radar*, 2012.

[90] P. Stoica, J. Li, J. Ling, and Y. Cheng, "Missing data recovery via a nonparametric iterative adaptive approach," in *2009 IEEE International Conference on Acoustics, Speech and Signal Processing*, IEEE, 2009, pp. 3369–3372.

[91] C. H. Musgrove and J. C. West, "Replacing missing data between airborne sar coherent image pairs," *IEEE Transactions on Aerospace and Electronic Systems*, vol. 53, no. 6, pp. 3150–3158, 2017.

[92] M. Çetin, I. Stojanović, N. Ö. Önhon, *et al.*, "Sparsity-driven synthetic aperture radar imaging: Reconstruction, autofocusing, moving targets, and compressed sensing," *IEEE Signal Processing Magazine*, vol. 31, no. 4, pp. 27–40, 2014.

[93] K. Cuomo, J. Pion, and J. Mayhan, "Ultrawide-band coherent processing," *IEEE Transactions on Antennas and Propagation*, vol. 47, no. 6, pp. 1094–1107, 1999.

[94] J. Karlsson, W. Rowe, L. Xu, G.-O. Glentis, and J. Li, "Fast missing-data iaa with application to notched spectrum sar," *IEEE Transactions on Aerospace and Electronic Systems*, vol. 50, no. 2, pp. 959–971, 2014.

[95] E. G. Larsson, P. Stoica, and J. Li, "Amplitude spectrum estimation for two-dimensional gapped data," *IEEE Transactions on Signal Processing*, vol. 50, no. 6, pp. 1343–1354, 2002.

[96] P. Foster, J. D. Halsey, and M. G. Hussain, "Ultra-wideband antenna technology," in *Introduction to Ultra-Wideband Radar Systems*, CRC Press, 2020, pp. 145–286.

[97] D. Oloumi, J.-W. Ting, and K. Rambabu, "Design of pulse characteristics for near-field uwb-sar imaging," *IEEE Transactions on Microwave Theory and Techniques*, vol. 64, no. 8, pp. 2684–2693, 2016.

[98] P. Valluraiah and B. Biswal, "Ecg signal analysis using hilbert transform," in *2015 IEEE Power, Communication and Information Technology Conference (PCITC)*, IEEE, 2015, pp. 465–469.

[99] A. V. Oppenheim, *Discrete-time signal processing*. Pearson Education India, 1999.

[100] G. Turin, "An introduction to matched filters," *IRE transactions on Information theory*, vol. 6, no. 3, pp. 311–329, 1960.

[101] D. Oloumi, P. Boulanger, A. Kordzadeh, and K. Rambabu, "Breast tumor detection using uwb circular-sar tomographic microwave imaging," in *2015 37th Annual International Conference of the IEEE Engineering in Medicine and Biology Society (EMBC)*, IEEE, 2015, pp. 7063–7066.

[102] L. Li, A. E.-C. Tan, K. Jhamb, and K. Rambabu, "Buried object characterization using ultra-wideband ground penetrating radar," *IEEE Transactions on Microwave Theory and Techniques*, vol. 60, no. 8, pp. 2654–2664, 2012.

[103] J. Elmore, K. Armstrong, C. Lehman, and S. Fletcher, "Screening for breast cancer," *JAMA*, vol. 293, no. 10, pp. 1245–1256, 2005.

[104] C. H. Lee, D. D. Dershaw, D. Kopans, *et al.*, "Breast cancer screening with imaging: Recommendations from the society of breast imaging and the acr on the use of mammography, breast mri, breast ultrasound, and other technologies for the detection of clinically occult breast cancer," *Journal of the American college of radiology*, vol. 7, no. 1, pp. 18–27, 2010.

[105] A. Nnewihe, E. Staroswiecki, N. Bangerter, and B. Hargreaves, "Dual tuned Helmholtz coil for breast cancer imaging," in *Proc. Intl. Soc. Mag. Reson*, 2008.

[106] E. J. Hall and D. J. Brenner, "Cancer risks from diagnostic radiology," *The British Journal of Radiology*, vol. 81, pp. 362–378, 2008.

[107] D. Grady, "American cancer society, in a shift, recommends fewer mammograms," *The New York Times*, Oct, 20th, 2015.

[108] G. I. Andreea, R. Pegza, L. Lascu, S. Bondari, Z. Stoica, and A. Bondari, "The role of imaging techniques in diagnosis of breast cancer," *Current health sciences Journal*, vol. 37, no. 2, pp. 241–248, 2011.

[109] S. P. Na and D. Houserkovaa, "The role of various modalities in breast imaging," *Biomed Pap Med Fac Univ Palacky Olomouc Czech Repub*, vol. 151, no. 2, pp. 209–218, 2007.

[110] S. C. Hagness, A. Taflove, and J. E. Bridges, "Two-dimensional fdtd analysis of a pulsed microwave confocal system for breast cancer detection: Fixed-focus and antenna-array sensors," *IEEE Transactions on Biomedical Engineering*, vol. 45, no. 12, pp. 1470–1479, 1998.

[111] S. C. Hagness, A. Taflove, and J. E. Bridges, "Three-dimensional FDTD analysis of a pulsed microwave confocal system for breast cancer detection: Design of an antenna-array element," *IEEE Transactions on Antennas and Propagation*, vol. 47, no. 5, pp. 783–791, 1999.

[112] E. C. Fear and M. A. Stuchly, "Microwave detection of breast cancer," *IEEE Transactions on Microwave Theory and Techniques*, vol. 48, no. 11, pp. 1854–1863, Nov. 2000, ISSN: 0018-9480. DOI: 10.1109/22.883862.

[113] J. D. Shea, P. Kosmas, S. C. Hagness, and B. D. Van Veen, "Three-dimensional microwave imaging of realistic numerical breast phantoms via a multiple-frequency inverse scattering technique," *Medical physics*, vol. 37, no. 8, pp. 4210–4226, 2010.

[114] M. Ostadrahimi, P. Mojabi, A. Zakaria, J. LoVetri, and L. Shafai, "Enhancement of Gauss Newton inversion method for biological tissue imaging," *IEEE Transactions on Microwave Theory and Techniques*, vol. 61, no. 9, pp. 3424–3434, Sep. 2013, ISSN: 0018-9480. DOI: 10.1109/TMTT.2013.2273758.

[115] M. Ostadrahimi, A. Zakaria, J. LoVetri, and L. Shafai, "A near-field dual polarized (TE-TM) microwave imaging system," *IEEE Transactions on Microwave Theory and Techniques*, vol. 61, no. 3, pp. 1376–1384, Mar. 2013, ISSN: 0018-9480. DOI: 10.1109/TMTT.2012.2237181.

[116] P. Kosmas and C. M. Rappaport, "Time reversal with the FDTD method for microwave breast cancer detection," *IEEE Transactions on Microwave Theory and Techniques*, vol. 53, no. 7, pp. 2317–2323, Jul. 2005, ISSN: 0018-9480. DOI: 10.1109/TMTT.2005.850444.

[117] T.Rubaek, P. M. Meaney, P. Meincke, and K. D. Paulsen, "Nonlinear microwave imaging for breast-cancer screening using gauss-newtons method and the cgls inversion algorithm," *IEEE Transactions on Antennas and Propagation*, vol. 55, no. 8, pp. 2320–2331, Aug. 2007, ISSN: 0018-926X. DOI: 10.1109/TAP.2007.901993.

[118] P. M. Meaney, M. W. Fanning, D. Li, S. P. Poplack, and K. D. Paulsen, "A clinical prototype for active microwave imaging of the breast," *IEEE Transactions on Microwave Theory and Techniques*, vol. 48, no. 11, pp. 1841–1853, Nov. 2000, ISSN: 0018-9480. DOI: 10.1109/22.883861.

[119] S. Y. Semenov, A. E. Bulyshev, A. E. Souvorov, *et al.*, "Three-dimensional microwave tomography: Experimental imaging of phantoms and biological objects," *IEEE Transactions on Microwave Theory and Techniques*, vol. 48, no. 6, pp. 1071–1074, Jun. 2000, ISSN: 0018-9480.

[120] A. E. Bulyshev, S. Y. Semenov, A. E. Souvorov, *et al.*, "Computational modeling of three-dimensional microwave tomography of breast cancer," *IEEE Transactions on Biomedical Engineering*, vol. 48, no. 9, pp. 1053–1056, Sep. 2001, ISSN: 0018-9294.

[121] S. Y. Semenov, A. E. Bulyshev, A. Abubakar, *et al.*, "Microwave-tomographic imaging of the high dielectric-contrast objects using different image-reconstruction approaches," *IEEE Transactions on Microwave Theory and Techniques*, vol. 53, no. 7, pp. 2284–2294, Jul. 2005, ISSN: 0018-9480.

[122] E. J. Bond, X. Li, S. C. Hagness, and B. D. V. Veen, "Microwave imaging via space-time beamforming for early detection of breast cancer," *IEEE Transactions on Antennas and Propagation*, vol. 51, no. 8, pp. 1690–1705, Aug. 2003, ISSN: 0018-926X.

[123] A. H. Golnabi, P. M. Meaney, and K. D. Paulsen, "Tomographic microwave imaging with incorporated prior spatial information," *IEEE Transactions on Microwave Theory and Techniques*, vol. 61, no. 5, pp. 2129–2136, May 2013, ISSN: 0018-9480.

[124] L. Li, A.-C. Tan, K. Jhamb, and K. Rambabu, "Characteristics of ultra-wideband pulse scattered from metal planar objects," *IEEE Transactions on Antennas and Propagation*, vol. 61, no. 6, pp. 3197–3206, Jun. 2013, ISSN: 0018-926X. DOI: 10.1109/TAP.2013.2247371.

[125] G. Turin, "An introduction to matched filters," *IRE Transactions on Information Theory*, vol. 6, no. 3, pp. 311–329, Jun. 1960, ISSN: 0096-1000. DOI: 10.1109/TIT.1960.1057571.

[126] D. Oloumi, P. Boulanger, A. Kordzadeh, and K. Rambabu, "Breast tumor detection using UWB circular-SAR tomographic microwave imaging," in *IEEE Engineering in Medicine and Biology Society (EMBC), 2015 37th Annual International Conference*, Aug. 2015, pp. 7063–7066. DOI: 10.1109/EMBC.2015.7320019.

[127] D. Oloumi, M. Pettersson, P. Mousavi, and K. Rambabu, "Imaging of oil-well perforations using UWB synthetic aperture radar," *IEEE Transactions on Geoscience and Remote Sensing*, vol. 53, no. 8, pp. 4510–4520, Aug. 2015, ISSN: 0196-2892. DOI: 10.1109/TGRS.2015.2400918.

[128] M. Lazebnik, L. McCartney, D. Popovic, *et al.*, "A large-scale study of the ultrawideband microwave dielectric properties of normal breast tissue obtained from reduction surgeries," *Physics in medicine and biology*, vol. 52, no. 10, p. 2637, 2007.

[129] L. Guo and A. M. Abbosh, "Optimization-based confocal microwave imaging in medical applications," *IEEE Transactions on Antennas and Propagation*, vol. 63, no. 8, pp. 3531–3539, Aug. 2015, ISSN: 0018-926X. DOI: 10.1109/TAP.2015.2434394.

[130] *Cst microwave studio suite, electromagnectic field simlation software*, version 2018, 2018. [Online]. Available: https://www.3ds.com/products-services/simulia/products/cst-studio-suite/.

[131] M. J. Burfeindt, T. J. Colgan, R. O. Mays, *et al.*, "MRI-derived 3D printed breast phantom for microwave breast imaging validation," *IEEE antennas and wireless propagation letters*, vol. 11, pp. 1610–1613, 2012.

[132] D. Milanesio, M. Saccani, R. Maggiora, D. Laurino, and M. Porporato, "Design of an harmonic radar for the tracking of the a sian yellow-legged hornet," *Ecology and evolution*, vol. 6, no. 7, pp. 2170–2178, 2016.

[133] G. J. Mazzaro, A. F. Martone, K. I. Ranney, and R. M. Narayanan, "Nonlinear radar for finding rf electronics: System design and recent advancements," *IEEE Transactions on Microwave Theory and Techniques*, vol. 65, no. 5, pp. 1716–1726, May 2017, ISSN: 0018-9480. DOI: 10.1109/TMTT.2016.2640953.

[134] M. Rahman and K. Wu, "A nonlinear transmission approach to compressing rise and fall time in picosecond pulse generation," *IEEE Transactions on Instrumentation and Measurement*, vol. 70, pp. 1–13, 2021. DOI: 10.1109/TIM.2021.3075526.

[135] A. S. Go, D. Mozaffarian, V. L. Roger, *et al.*, "Heart disease and stroke statistics—2014 update: A report from the american heart association," *Circulation*, vol. 129, no. 3, e28–e292, 2014.

[136] S. Joof, G. Cansiz, S. Ozgur, T. Yilmaz, M. Cayoren, and I. Akduman, "Tissue mimicking phantoms for microwave brain stroke imaging," in *2018 18th Mediterranean Microwave Symposium (MMS)*, 2018, pp. 332–333. DOI: 10.1109/MMS.2018.8612103.

[137] M. P. LaMonte, Y. Xiao, P. F. Hu, *et al.*, "Shortening time to stroke treatment using ambulance telemedicine: Telebat," *Journal of Stroke and Cerebrovascular Diseases*, vol. 13, no. 4, pp. 148–154, 2004.

[138] M. Mazighi, S. A. Chaudhry, M. Ribo, *et al.*, "Impact of onset-to-reperfusion time on stroke mortality: A collaborative pooled analysis," *Circulation*, vol. 127, no. 19, pp. 1980–1985, 2013.

[139] X. Lin, Y. Chen, Z. Gong, and H. Zhang, "Brain stroke classification using a microwave transmission line approach," in *2020 IEEE Asia-Pacific Microwave Conference (APMC)*, 2020, pp. 1092–1094. DOI: 10.1109/APMC47863.2020.9331463.

[140] V. Mariano, J. A. T. Vasquez, R. Scapaticci, L. Crocco, P. Kosmas, and F. Vipiana, "Comparison of reconstruction algorithms for brain stroke microwave imaging," in *2020 IEEE MTT-S International Microwave Biomedical Conference (IMBioC)*, 2020, pp. 1–3. DOI: 10.1109/IMBIoC47321.2020.9385032.

[141] A. Zamani, A. T. Mobashsher, B. J. Mohammed, and A. M. Abbosh, "Microwave imaging using frequency domain method for brain stroke detection," in *2014 IEEE MTT-S International Microwave Workshop Series on RF and Wireless Technologies for Biomedical and Healthcare Applications (IMWS-Bio2014)*, 2014, pp. 1–3. DOI: 10.1109/IMWS-BIO.2014.7032452.

[142] D. Ireland, K. Bialkowski, and A. Abbosh, "Microwave imaging for brain stroke detection using born iterative method," *IET Microwaves, Antennas & Propagation*, vol. 7, no. 11, pp. 909–915, 2013.

[143] I. Merunka, D. Vrba, O. Fiser, J. Cumana, and J. Vrba, "2d microwave system for testing of brain stroke imaging algorithms," in *2019 European Microwave Conference in Central Europe (EuMCE)*, 2019, pp. 508–511.

[144] D. Ireland and A. Abbosh, "Modeling human head at microwave frequencies using optimized debye models and fdtd method," *IEEE Transactions on Antennas and Propagation*, vol. 61, no. 4, pp. 2352–2355, 2013. DOI: 10.1109/TAP.2013.2242037.

[145] V. L. Coli, P.-H. Tournier, V. Dolean, *et al.*, "Detection of simulated brain strokes using microwave tomography," *IEEE Journal of Electromagnetics, RF and Microwaves in Medicine and Biology*, vol. 3, no. 4, pp. 254–260, 2019. DOI: 10.1109/JERM.2019.2921076.

[146] U. Ahmed, A. Mobashsher, K. Bialkowski, and A. Abbosh, "Convex optimization approach for stroke detection in microwave head imaging," in *2014 Makassar International Conference on Electrical Engineering and Informatics (MICEEI)*, 2014, pp. 46–49. DOI: 10.1109/MICEEI.2014.7067308.

[147] P.-H. Tournier, F. Hecht, F. Nataf, *et al.*, "Microwave tomography for brain stroke imaging," in *2017 IEEE International Symposium on Antennas and Propagation USNC/URSI National Radio Science Meeting*, 2017, pp. 29–30. DOI: 10.1109/APUSNCURSINRSM.2017.8072057.

[148] J. Xu, L. Ren, H. Fan, E. Mao, and Q. Liu, "Clutter and range ambiguity suppression using diverse pulse train in pulse doppler system," *Sensors*, vol. 18, no. 7, p. 2326, 2018.

[149] A. T. Htet, E. H. Burnham, G. M. Noetscher, D. N. Pham, A. Nummenmaa, and S. N. Makarov, "Collection of cad human head models for electromagnetic simulations and their applications," *Biomedical Physics & Engineering Express*, vol. 5, no. 6, p. 067 005, 2019.

[150] P. Hasgall and G. Di. "It'is database for thermal and eletromagnetic parameters of biological tissues." (2022), [Online]. Available: itis.swiss/database.

[151] L.-E. Andersson, "On the determination of a function from spherical averages," *SIAM Journal on Mathematical Analysis*, vol. 19, no. 1, pp. 214–232, 1988. DOI: 10.1137/0519016. eprint: http://dx.doi.org/10.1137/0519016.

[152] M. Parker, "Radar basics-part 2: Pulse doppler radar," *Electronics Engineering Times. Available online at: http://www. eetimes. com/document. asp*, 2011.

[153] S. Mikki, "Theory of nonsinusoidal small antennas for near-field communication system analysis," *Progress In Electromagnetics Research B*, vol. 86, pp. 177–193, 2020.